JPhys Photonics

PURPOSE-LED PUBLISHING™

TOPICAL REVIEW • OPEN ACCESS

# Liquid crystal-integrated tunable metamaterials and metasurfaces: from microwave to optical frequencies

To cite this article: Gülcan Aydın *et al* 2026 *J. Phys. Photonics* **8** 032004

View the article online for updates and enhancements.

You may also like

- Combined spatially and temporally multiplexed photonic reservoir computer with a diffractively coupled VCSEL-array
J Robertson, M Pflüger, I Fischer et al.
- Gauge-programmable mode selection in non-Hermitian directed-graph networks
Wenwen Liu and Shuang Zhang
- Correlative photoacoustic and nonlinear microscopy measurements reveal ageing signatures in multilayered paint systems
Eleanna Pirgianaki, Meropi Mari, Kristalia Melessanaki et al.

This content was downloaded from IP address 193.140.54.157 on 07/10/2026 at 19:17

Journal of Physics: Photonics

Check for updates

OPEN ACCESS

RECEIVED
13 June 2026

REVISED
29 August 2026

ACCEPTED FOR PUBLICATION
10 September 2026

PUBLISHED
23 September 2026

Original content from this work may be used under the terms of the Creative Commons Attribution 4.0 licence.

Any further distribution of this work must maintain attribution to the author(s) and the title of the work, journal citation and DOI.

TOPICAL REVIEW

# Liquid crystal-integrated tunable metamaterials and metasurfaces: from microwave to optical frequencies

**Gülcan Aydın**[1,*], **İdris Candan**[1], **Mahpeyker Kocakoç Toprakoğlu**[2] and **Sait Eren San**[1]

[1] Department of Physics, Faculty of Arts and Sciences, Kocaeli University, 41001 Kocaeli, Türkiye
[2] Department of Computer Technologies, Cukurova University, Adana, Türkiye
[*] Author to whom any correspondence should be addressed.

**E-mail:** gulcan.aydin@kocaeli.edu.tr

**Keywords:** liquid crystals, tunable metamaterials, metasurfaces, dynamic electromagnetic control, frequency selective surfaces, reconfigurable intelligent surfaces, AI-assisted design

## Abstract

Conventional metamaterials (MMs) are fundamentally constrained by their static architectures, which lock electromagnetic properties at the time of fabrication and prevent real-time tunability. To overcome these limitations, this review systematically explores the integration of liquid crystals (LCs) with electromagnetic MMs and metasurfaces, focusing on dynamic and tunable devices spanning microwave, terahertz, and optical frequency regimes. The review outlines the theoretical foundations of MMs and provides a taxonomy of LC phases—nematic, smectic, cholesteric, blue phase, discotic, and lyotropic—distinguishing the present work from prior reviews addressing only nematic LCs. Four principal integration strategies (layered, embedded, microfluidic-based, and hybrid) are examined, followed by a systematic review of all major architecture families: split-ring resonator-based bulk MMs, fishnet structures, frequency selective surfaces, plasmonic metasurfaces, and chiral structures. Fabrication techniques including photolithography, EBL, FIB milling, nanoimprint lithography, and 3D printing are benchmarked against cost, throughput, and scalability metrics, with analysis of commercialization prospects. Dedicated sections address long-term stability and degradation mechanisms, electromagnetic loss sources and mitigation strategies, and a systematic comparison of LCs with competing tunable platforms including graphene, $VO_2$, GST, MEMS, ferroelectrics, and transparent conducting oxides. Engineering trade-offs among tuning range, LC thickness, operating voltage, and switching speed are analysed quantitatively. Standardized figures of merit are proposed for microwave, THz, and optical platforms to enable cross-platform benchmarking. The convergence of artificial intelligence -assisted inverse design with LC-MM systems is discussed, including integration with Reconfigurable Intelligent Surfaces for 6 G communications. Applications in telecommunications, biomedical imaging, sensing, and display technologies are highlighted, and five key research bottlenecks are identified.

## 1. Introduction

The development of adaptive electromagnetic devices capable of real-time environmental response has emerged as a critical frontier in photonics and materials science. Metamaterials (MMs) [1] are artificial structures engineered at subwavelength scales. They have revolutionized this field by enabling extraordinary properties such as negative refraction [2], electromagnetic invisibility [3, 4], and superlensing [5–7]. Unlike conventional materials, these properties arise not from chemical composition but from meticulously designed geometries, as first theorized by Veselago [8]. Practical realization began with Pendry's split-ring resonators (SRRs) [9, 10] and Smith's experimental demonstration of negative-index media [11], which laid the foundation for advancements in acoustic MMs [12], as well as mechanical, and programmable MMs.

Throughout this review, a clear distinction is maintained between two related but fundamentally different classes of artificial electromagnetic structures. MMs refer to three-dimensional, volumetrically

© 2026 The Author(s). Published by IOP Publishing Ltd

periodic structures, such as multilayer fishnet architectures or bulk SRR arrays, whose electromagnetic properties (including negative permittivity, negative permeability, or negative refractive index) emerge from the collective response of subwavelength unit cells distributed throughout the material volume. Metasurfaces, by contrast, are the two-dimensional counterparts of MMs: ultrathin, planar arrays of subwavelength resonators or antennas confined to a single layer or a few layers on a substrate. Rather than modifying bulk electromagnetic properties, metasurfaces impart abrupt, spatially engineered changes in the phase, amplitude, or polarization of electromagnetic waves at the interface itself. While both classes share the principle of subwavelength structuring, their dimensionality, operating mechanisms, and practical form factors differ substantially. In the context of LC integration, MMs exploit the LC-tunable dielectric environment to shift bulk resonance conditions (e.g. negative-index passband in fishnets, magnetic resonance in volumetric SRR arrays), whereas LC-integrated metasurfaces harness the same molecular reorientation to reconfigure surface-level wavefront control functions such as beam steering, holography, and polarization conversion. This distinction is reflected in the structure of the present review, where separate subsections address LC-enhanced plasmonic metasurfaces, LC-integrated SRR-based MMs, and LC-enhanced fishnet MMs, among others.

Despite their transformative potential, conventional MMs suffer from a key limitation: their static architectures fix electromagnetic properties post-fabrication, hindering adaptability. For instance, frequency-specific absorbers cannot adapt to changing interference environments, while rigid metasurfaces lack the flexibility required for reconfigurable communication protocols or multifunctional imaging systems [13]. This inherent rigidity has spurred demand for materials whose electromagnetic behaviour can be dynamically tuned during operation, not just fabrication.

Liquid crystals (LCs) [14, 15] offer a promising solution. Their anisotropic molecular structure responds to external stimuli (electric fields, temperature, stress) [16], enabling voltage-tunable birefringence and permittivity [17–23]. Early breakthroughs include terahertz LC-MM absorbers by Shrekenhamer *et al* [24] with 30% modulation depth and Yang *et al*'s [25] designs demonstrating tunable electromagnetically induced transparency (EIT) with 18.3 dB modulation. These systems exemplify the potential of LC integration for adaptive polarization and resonance control.

LCs constitute a broad family of mesophases with distinct molecular architectures. Thermotropic LCs, the most relevant class for MM applications, are further divided into several categories. The nematic (N) phase, composed of rod-shaped (calamitic) molecules with long-range orientational order but no positional order, exhibits the highest birefringence ($\Delta n = n_e - n_o \approx 0.1$–$0.4$) among common phases and is the dominant choice for tunable metasurfaces due to its voltage-driven director reorientation. The smectic phases add positional order: Smectic-A (SmA) molecules are arranged in layers perpendicular to the director, while in Smectic-C (SmC) the director is tilted relative to the layer normal; when chirality is introduced, the latter becomes the ferroelectric SmC phase with spontaneous polarization and sub-microsecond switching times. The cholesteric (or chiral nematic, $N^*$) phase arises when a chiral dopant is added to a nematic host, forming a helical superstructure whose pitch—and thus selective reflection wavelength—is tunable by temperature, electric field, or UV exposure. At higher chirality concentrations, cubic Blue Phases (BP I, II, III) emerge, consisting of double-twist cylinder lattices with intrinsically fast electro-optic response ($\sim$1 ms) and an isotropic appearance. Discotic LCs, formed by disc-shaped molecules, self-assemble into columnar phases and are exploited in charge-transport and organic photonics applications. In contrast to thermotropic systems, lyotropic LCs are concentration-driven: amphiphilic molecules in solution form micellar, hexagonal columnar, or lamellar phases depending on concentration, and are relevant for bio-inspired and soft-matter photonic devices. The selection of an appropriate LC phase for a given MM platform, therefore, depends on the required switching speed, operating frequency range, fabrication compatibility, and birefringence magnitude. To effectively harness these properties, various structural approaches are employed; the four principal LC-MM integration strategies and their dynamic operating principles are illustrated in figure 1.

The applications of LC-enhanced MMs span diverse industries. In telecommunications, reconfigurable antennas optimize spectrum sharing in 5 G/6 G networks, providing maximum aperture efficiency of 22.5% and beam coverage of over 120° [26]. Healthcare benefits from terahertz MMs that enhance cancer imaging resolution to sub-millimetre precision. In the energy sector, LC-based MM absorbers have achieved absorption rates exceeding 92% in the range of 116.5 GHz–121.8 GHz [27]. Representative device-level demonstrations include electrically tunable spatial light and phase modulators, switchable meta-pixels, and voltage-controlled beam-steering metasurfaces operating from the terahertz to the optical range [28–32]. Quantum photonics has emerged as a prospective application domain, in which static dielectric metasurfaces have already been used to prepare and reconstruct entangled photon states. The extension of this capability to electrically reconfigurable LC-integrated platforms is discussed in section 3.9.

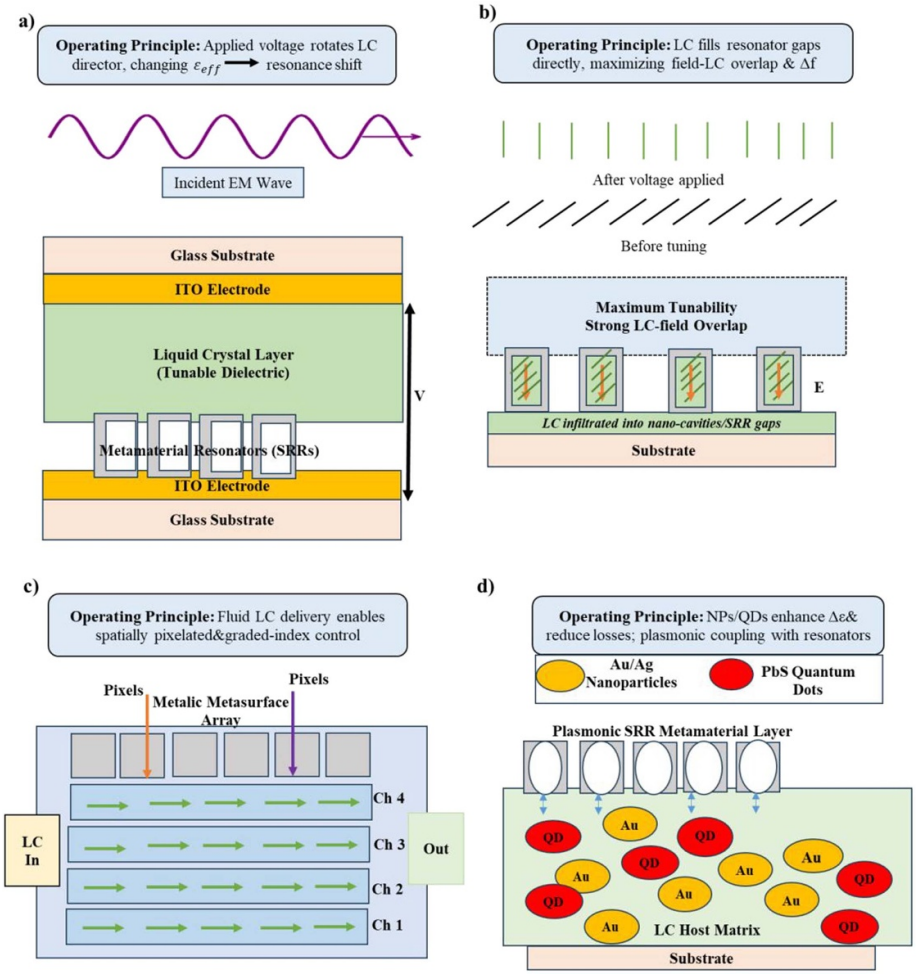



**Figure 1.** Schematic illustration of the four principal LC-metamaterial integration strategies and their dynamic operating principles. (a) Layered integration: The LC layer acts as a tunable dielectric sandwiched between ITO electrodes and the metamaterial resonators; applied voltage rotates the LC director, modifying the effective permittivity ($\varepsilon_{\text{eff}}$) and shifting the resonance frequency. (b) Embedded (infiltrated) integration: LC molecules are infiltrated directly into the nano-gaps of resonator structures, maximizing the field-LC overlap and achievable frequency tunability. (c) Microfluidic integration: Controlled delivery of LC material through microchannels enables spatially pixelated and gradient-index electromagnetic control. (d) Hybrid integration: Dispersion of metal nanoparticles or quantum dots in the LC host enhances dielectric anisotropy and introduces strong plasmonic coupling.

However, technical challenges persist. At optical frequencies, precise alignment of LC molecules within nanostructured cavities remains a manufacturing hurdle, while optical losses from metal-LC interactions limit efficiency. Innovations such as roll-to-roll nanoimprinting and two-photon polymerization (TPP) are addressing scalability, though interdisciplinary collaboration across materials science, photonics, and nanotechnology is essential for full industrial adoption.

This review advances the understanding of LC-enhanced MMs by systematically consolidating interdisciplinary research and addressing critical gaps in tunable electromagnetic systems. As summarized in table 1, no previous review simultaneously covers all six LC phase classes (nematic, smectic, cholesteric, blue phase, discotic, and lyotropic), all four principal architecture families (SRR-based bulk MMs, fishnet structures, frequency selective surfaces (FSSs), and chiral/asymmetric metasurfaces), and the full microwave-to-optical frequency spectrum. While prior works such as Li *et al* [33] focus exclusively on THz MMs with nematic LCs, and Kang *et al* [34] address only visible-range 2D metasurfaces, the present review uniquely bridges these domains and additionally incorporates fabrication benchmarking, a systematic comparison with competing tunable material platforms (graphene, $VO_2$, GST, MEMS), long-term stability analysis, and an outlook on artificial intelligence (AI)-assisted design methodologies. The work is structured to guide readers through foundational principles, innovative integration strategies, and experimental breakthroughs in microwave, terahertz, and optical regimes. Technical challenges such as nanoscale LC alignment and optical losses are rigorously analysed, with scalable solutions like roll-to-roll nanoimprinting highlighted as pathways to industrial adoption. By bridging theoretical models,

**Table 1.** Comparison of present review with key prior works.

| Review paper | Year | Frequency range | LC phases covered | Architecture types | Key distinction from present work |
|---|---|---|---|---|---|
| Li *et al* [33] | 2024 | THz only | Nematic only | Absorbers, modulators | THz-only scope; no FSS, no chiral, no LC-phase taxonomy |
| Kang *et al* [34] | 2024 | Visible–NIR | Nematic only | 2D metasurfaces only | No 3D metamaterials, no THz/microwave, no fabrication review |
| Gorkunov *et al* [35] | 2015 | Microwave–Optical | Nematic only | SRR, plasmonic | No FSS, no fishnet, no chiral; no fabrication comparison |
| Wang *et al* [36] | 2025 | THz | Nematic, smectic | Modulators, absorbers | No FSS; no AI design discussion; no comparative FoM table |
| Present Work (Aydin *et al*) | 2026 | Microwave–THz–Optical | Nematic, smectic, cholesteric, blue phase, discotic, lyotropic | SRR, fishnet, FSS, plasmonic, chiral, 2D/3D | Full LC-phase taxonomy; all architecture classes; fabrication benchmarking; LC vs competing materials; AI design outlook |

fabrication advancements, and real-world applications, this review establishes a comprehensive roadmap for transitioning LC-MM innovations from laboratory research to transformative technologies.

## 2. Material principles of LC-MM integration

The integration of LCs with MMs brings a vital capability to electromagnetic devices: adaptability. While MMs are celebrated for their ability to manipulate waves through engineered geometry, their fixed physical structure inherently limits them to static operation. By incorporating LCs into these structures, we introduce a tunable dielectric environment, effectively transforming passive resonators into dynamic, reconfigurable systems. This section outlines the material mechanisms that make this integration possible and the engineering challenges involved in creating a stable interface.

### 2.1. Fundamental theories of LCs

Before discussing specific tuning mechanisms and integration strategies, it is useful to summarize the fundamental theoretical framework that governs the behaviour of LCs, since every figure of merit of an LC-integrated MM, tuning range, driving voltage, switching speed, and alignment quality, can be traced back to a small set of underlying physical quantities.

The defining feature of a liquid crystalline mesophase is long-range orientational order without (in the nematic case) positional order. The degree of order is quantified by the scalar order parameter $S = \langle(3\cos^2\theta - 1)/2\rangle$, where $\theta$ is the angle between the long axis of an individual molecule and the average orientation direction, the director $n$. $S$ vanishes in the isotropic phase and typically takes values of 0.4–0.7 deep in the nematic phase. At the molecular level, the stability of the nematic phase is captured by the Maier–Saupe mean-field theory, in which anisotropic dispersion interactions favour parallel molecular alignment [37]; at the macroscopic level, the Landau–de Gennes (LdG) expansion of the free energy in powers of S describes the weakly first-order nematic–isotropic transition at the clearing temperature $T_{NI}$ [38]. The practical consequence for MM design is direct: both the optical birefringence $\Delta n$ and the dielectric anisotropy $\Delta\varepsilon$ scale with $S$, so the maximum achievable resonance shift of any LC-integrated device is bounded by the order parameter of the chosen mixture and collapses as the operating temperature approaches $T_{NI}$.

Spatial distortions of the director field cost elastic energy, described by the Oseen–Frank continuum theory through three fundamental deformation modes, splay, twist, and bend, with elastic constants $K_{11}$, $K_{22}$, and $K_{33}$, typically of the order of a few piconewtons [39, 40]. In LC-integrated MMs this elasticity is not a formality: when the LC is confined in sub-micrometre resonator gaps or nanoholes, the elastic energy of reorientation competes with the surface anchoring energy, and complete director switching may become energetically inaccessible. This is one of the principal reasons why the effective tunability measured in nanostructured devices is systematically smaller than the value predicted from bulk $\Delta\varepsilon$.

The balance between the aligning torque of an applied field and the elastic restoring torque defines a threshold below which no reorientation occurs. For a planar-aligned cell with positive $\Delta\varepsilon$, the threshold voltage is $V_{th} = \pi(K_{11}/\varepsilon_0\Delta\varepsilon)^{1/2}$, remarkably independent of the cell thickness [38, 41]. The Fréedericksz

threshold fixes the lower bound of the driving voltage of every electrically tuned LC-MM and is responsible for the characteristically nonlinear voltage–phase (or voltage–frequency-shift) response curves reported throughout section 3.

The temporal response is governed by the Ericksen–Leslie hydrodynamic theory [42]; in the simplest approximation the field-on and field-off relaxation times scale as $\tau \propto \gamma_1 d^2/(\mathrm{K}\pi^2)$, where $\gamma_1$ is the rotational viscosity and d the LC layer thickness. The quadratic thickness dependence explains the central speed advantage of metasurface integration: by concentrating the resonant field in ultrathin LC layers, meta-structures reduce the required d by up to two orders of magnitude relative to conventional cells, with a corresponding dramatic acceleration of the response. It equally underlies the tuning-range/speed trade-off analysed quantitatively in the engineering trade-offs section of this review.

Taken together, these quantities set the practical envelope of LC-MM performance: with $\Delta n \approx 0.1$–0.4 in the terahertz band and typical $\Delta\varepsilon$ of a few units, the achievable resonance shift is of the order of 5%–20% of the centre frequency, at driving voltages of a few volts and switching times ranging from milliseconds in bulk cells to sub-millisecond in ultrathin metasurface geometries.

The orientation imposed by bounding surfaces is described by the Rapini–Papoular anchoring energy [43], with strong anchoring enforcing a fixed easy axis and weak anchoring permitting field-assisted surface reorientation. On the chemically heterogeneous, nanostructured metal surfaces of MM resonators the easy axis is often ill-defined, which is the microscopic origin of the alignment challenges discussed later in this section.

The tuning mechanisms discussed in the following subsection, electric, magnetic, all-optical, and thermal, are best understood as different external handles acting on this single theoretical framework: each stimulus reorients the director (or suppresses $S$), and the resulting change of the dielectric tensor is subsequently transduced by the MM architecture into a measurable electromagnetic response.

### 2.2. Anisotropy and tuning mechanisms

The core mechanism driving LC-integrated MM devices is the controlled reorientation of the LC director ($\hat{n}$), in response to an external stimulus, which modifies the effective permittivity seen by the MM resonators and thereby shifts the resonance frequency, phase, or amplitude of the electromagnetic response [44].

It should be emphasized that the reorientation-induced modification of the LC dielectric tensor is a general mechanism that is not restricted to resonator-based architectures. In non-resonant waveguiding platforms, such as LC-core fibre waveguides [45] and LC-infiltrated photonic crystal fibres, the reorientation does not act through the localized resonance of a subwavelength meta-atom; instead, it manifests itself primarily as a change in the effective refractive index, accumulated propagation phase, polarization state, or modal confinement and loss of the guided wave. The two regimes therefore differ mainly in how the light–matter interaction is enhanced: resonant MMs concentrate the field within a subwavelength volume, whereas non-resonant waveguides accumulate the same anisotropy-induced index change over a long propagation length. Externally tunable devices exploiting this non-resonant response, including thermal, electrical, and all-optical control, have been demonstrated in LC-filled photonic bandgap fibres [46–48], and photonic LC fibres, particularly for polarization control, have developed into a field of their own [49]. The present review deliberately focuses on resonant MM and metasurface architectures, in which the LC-induced permittivity change is transduced into a shift of an engineered resonance; non-resonant LC waveguide photonics is addressed only where it directly informs MM integration.

Within this resonant framework, figure 2 illustrates schematically how rod-shaped (calamitic) nematic LC molecules respond to four distinct classes of external stimuli.

*Electric Field Tuning:* When the applied voltage exceeds the Fréedericksz threshold ($V_{\mathrm{th}}$), molecules with positive dielectric anisotropy ($\Delta\varepsilon > 0$) rotate to align their long axes parallel to the electric field (figure 2(a)). This reorientation changes the effective permittivity from $\varepsilon_\perp$ to $\varepsilon_\parallel$, producing a tunable shift in resonance frequency. This approach is the most widely used in active devices owing to its low driving voltages, CMOS compatibility, and fast modulation speeds. For example, this rapid modulation directly enables the development of active 5 G/6 G beam-steering antennas and real-time reconfigurable intelligent surfaces (RISs).

*Magnetic Tuning:* LC molecules also exhibit diamagnetic anisotropy ($\Delta\chi$), enabling contactless reorientation under an applied magnetic field exceeding the critical field $B_{\mathrm{c}}$ (figure 2(b)). Because no metallic electrodes are required, magnetic tuning eliminates electrode-induced interference with the resonator

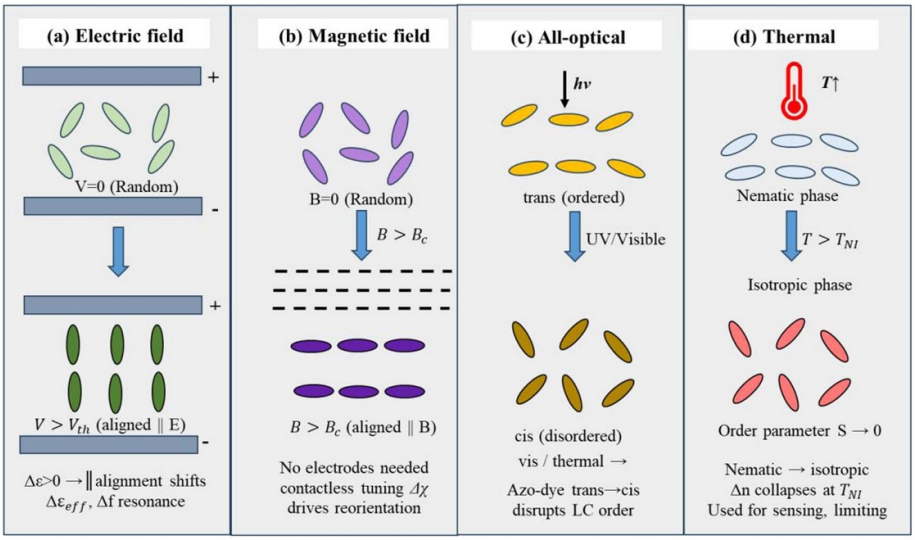



**Figure 2.** Illustration of liquid crystal (LC) molecule response mechanisms under various external stimuli. (a) Electric field: Reorientation of LC molecules with positive dielectric anisotropy ($\Delta\varepsilon > 0$) from the initial planar (homogeneous) alignment to an aligned state parallel to the field ($E$) when $V > V_{\text{th}}$, shifting the effective permittivity ($\varepsilon_{\text{eff}}$) and resonance frequency ($\Delta f$). (b) Magnetic field: Contactless tuning of LC orientation through magnetic anisotropy ($\Delta\chi$) above a critical field ($B_C$). (c) All-optical: Photochemical transformation of azo-dye molecules from trans (ordered) to cis (disordered) states under UV/Visible light, disrupting the LC order without external wiring. (d) Thermal: Phase transition from a highly anisotropic nematic phase to an isotropic phase above the clearing temperature ($T_{\text{NI}}$), where the order parameter ($S$) and birefringence ($\Delta n$) collapse.

geometry. Such contactless manipulation is highly advantageous for deploying terahertz isolators and tunable microwave absorbers in complex aerospace environments where physical wiring is impractical.

*All-Optical Switching:* When LCs are doped with photo-responsive agents such as azo-dye molecules, optical irradiation triggers a reversible trans-to-cis isomerization (figure 2(c)). Upon UV or visible-light exposure, the cis isomer adopts a bent geometry that disrupts the LC ordering and collapses the birefringence, enabling fully wireless, wiring-free electromagnetic control. In practical implementations, this all-optical control paves the way for ultrafast photonic switching and optical routing in advanced telecommunication networks.

*Thermal Tuning:* The nematic-to-isotropic phase transition at the clearing temperature $T_{\text{NI}}$ produces the most dramatic change in optical anisotropy: the order parameter $S$ falls continuously from its nematic value to zero as $T \rightarrow T_{\text{NI}}$, causing $\Delta n$ to collapse (figure 2(d)). Although thermal tuning is less suitable for rapid switching, the large and reproducible index change is heavily exploited in high-sensitivity temperature sensors. Additionally, this mechanism forms the basis for smart windows capable of dynamic thermal management in energy-efficient architectures [50, 51].

Furthermore, the effectiveness of these tuning mechanisms is highly dependent on initial molecular orientations and material compositions. For instance, previous studies by the co-authors of this review (Okutan *et al*) [52] have demonstrated that the dielectric anisotropy ($\Delta\varepsilon$) of dye-doped nematic LCs exhibits a strong frequency-dependent relaxation, transitioning from a positive to a negative anisotropy state under varying AC electric fields. This dielectrically controlled crossover behaviour provides an additional degree of freedom for advanced dual-frequency tuning in LC-integrated MM systems. To provide a clearer picture of the material requirements for these tuning mechanisms, especially in high-frequency applications, table 2 summarizes the key refractive and birefringent properties of prominent LC mixtures across the terahertz band. Additionally, table 3 presents a quantitative comparison of the four principal tuning mechanisms across key performance metrics, including tuning range, response time, modulation depth, and operating voltage, enabling direct assessment of their respective advantages and trade-offs for practical LC-MM applications.

Electrical tuning via AC field offers the best combination of low voltage (2.5–15 $V_{\text{rms}}$), CMOS compatibility, and response time (1.89–150 ms), making it dominant in practical devices. All-optical switching is attractive for wiring-free systems, while thermal tuning delivers the largest index contrast (suitable for sensing). Magnetic tuning eliminates electrode-induced field distortion but requires bulky magnet setups.

**Table 2.** Terahertz birefringence and refractive index properties of common LC Mixtures " Reproduced with permission from [36]. CC-BY-NC-ND 4.0.

| LC Material | Freq. Range (THz) | Ordinary index ($n_o$) | Extraordinary index ($n_e$) | Birefringence ($\Delta n$) at 1 THz | Characteristics |
|---|---|---|---|---|---|
| 5CB [53] | 0.3–1.4 | 1.59–1.83 | 1.74–2.04 | 0.130–0.210 | Standard nematic |
| E7 [54] | 0.2–2.0 | 1.557–1.581 | 1.690–1.704 | 0.130–0.148 | Widely used mixture |
| BL037 [55] | 0.3–2.5 | 1.56–1.62 | 1.76–1.78 | 0.200 | Temperature dependent |
| NJU-LDn-4 [56] | 0.4–1.6 | 1.50–1.51 | 1.80–1.82 | 0.310 | High birefringence |
| 2020 + nps3 [57] | 0.3–3.0 | 1.55–1.60 | 1.90–1.92 | 0.360 | Ferroelectric NP doped |
| LC1825 [58] | 0.2–2.5 | 1.54–1.57 | 1.91–1.95 | 0.380 | Low loss, high $\Delta n$ |

**Table 3.** Comparison of LC tuning mechanisms.

| Tuning Mechanism | Freq. range | Tuning range | Response time | Modulation depth | Operating voltage | Key advantage |
|---|---|---|---|---|---|---|
| Electrical (AC) | Microwave–THz–Optical | 3–21 GHz/5%–10% | 1.89 ms—150 ms | Up to 96% | 2.5–15 $V_{rms}$ | CMOS-compatible; low power |
| Magnetic | Microwave–THz | ∼3%–8% | Seconds | Moderate | N/A (contactless) | No electrode interference |
| Thermal | Microwave–THz | Large (phase transition) | Seconds–minutes | High near TNI | N/A | Large index change; sensing |
| All-optical (azo-dye) | NIR–Optical | ∼5%–15% | ms–s | Moderate | N/A (light-driven) | Wiring-free; remote control |

### 2.3. Dynamic features of LC–metasurface hybrid devices: a systematic comparison

A fundamental motivation for combining LCs with metasurfaces is that each component independently possesses certain electromagnetic functionalities, yet neither alone can achieve the full range of dynamically reconfigurable behaviour that their integration enables. To clarify the added value of the hybrid system, it is essential to systematically compare the optical properties of the standalone components with the emergent features of the integrated device. Circular dichroism (CD) provides an excellent illustrative example of how similar optical properties are modulated when combined:

*Standalone Metasurface* (*Passive*): A chiral metasurface exhibits CD, differential absorption of left-handed (LCP) and right-handed (RCP) circularly polarized light, due to its geometrically asymmetric resonators. It provides subwavelength spatial resolution and sharp spectral precision. However, this response is completely static; its CD magnitude and absorption preference are permanently locked at the time of fabrication.

*Standalone LC Medium* (*Bulk*): A LC medium, particularly in its cholesteric phase, natively exhibits CD due to its helical molecular superstructure. While its optical properties are voltage-tunable, this is a bulk optical effect that uniformly affects transmitted light across the entire aperture, lacking the subwavelength spatial resolution of a resonant metasurface.

*LC-Metasurface Hybrid Device* (*Dynamic*): Integrating birefringent nematic LCs into a chiral metal–insulator-metal (MIM) metasurface creates a fundamentally new dynamic capability. As demonstrated by Yin *et al* [59], the modulation occurs through a dynamic modification of the local dielectric environment. At an initial state (e.g. LC molecules aligned at 0°), the metasurface strongly absorbs one spin state (e.g. RCP) and reflects the opposite spin, yielding a strong positive CD. When an external voltage is applied, the LC molecules realign toward 90°, which alters the plasmonic coupling conditions between the chiral resonators. Crucially, this does not merely tune the absorption magnitude; it enables the complete reversal of the CD sign. The system switches its absorption preference while maintaining an absorption efficiency above 80% and a CD near 70%. This dynamic sign reversal—a functionality achievable neither by the static metasurface nor by the bulk LC alone—highlights how the hybrid architecture transcends the limitations of its individual constituents.

### 2.4. Interface engineering and alignment challenges

Successfully integrating organic LCs with inorganic metallic structures is not merely a matter of infiltration; it is a complex surface engineering challenge. The performance of the final device depends heavily on how well the LC molecules align within the subwavelength features of the MM. If the alignment

is random or disturbed, the device suffers from high scattering losses and a low Quality Factor (Q-factor). Historically, mechanical rubbing of polyimide layers has been the industry standard for displays. However, in the context of MMs, this method is often destructive; the physical friction can damage delicate nanostructures and fails to provide uniform alignment near sharp metallic edges [60]. To overcome this, photoalignment techniques have emerged as the superior solution. By exposing photosensitive polymers to polarized UV light, researchers can dictate the alignment direction without physically touching the surface. This non-contact method allows for precise molecular ordering even inside deep nanocavities, which is critical for minimizing optical losses [61–63]. Additionally, treating the metallic surfaces with self-assembled monolayers (SAMs) allows engineers to fine-tune the anchoring energy, directly improving the switching speed and reducing the voltage required to drive the device [64].

A significant challenge in electrically tuned LC-MMs is the fringe field effect. When a patterned metasurface is used directly as an electrode, it often generates a non-uniform static electric field, leaving LC molecules near the edges partially unaligned or requiring excessively high driving voltages. To overcome this, Wang *et al* [65] integrated few-layer porous graphene (FLPG) directly onto a cross-shaped metasurface. The highly transparent (>98% in THz) graphene layer acts as a continuous electrode, providing a uniform static electric field that successfully drives a homogeneous planar-to-homeotropic LC transition at a low operating voltage of 10 V, while the underlying metallic metasurface reduces the overall sheet resistance to ∼400 Ω $sq^{-1}$.

## 3. Integration of LCs with MMs

LCs are integrated with MMs by embedding an LC layer within or around the MM structure, enabling dynamic control of electromagnetic properties through molecular reorientation. When an external electric field (AC or DC) is applied, LC molecules reorient depending on the sign of their dielectric anisotropy, which is the difference between permittivity values along different molecular axes, thereby changing the effective refractive index of the LC layer. Initially, the molecules are uniformly aligned using alignment layers which are specially treated surfaces that impose a preferred orientation on LC molecules, to prevent light scattering. This change in refractive index modifies the electromagnetic environment of the MM, shifting its resonance frequency, phase, or amplitude. For example, in SRRs, LC reorientation adjusts the capacitance and inductance, which directly determine the resonant frequency at which the MM interacts with electromagnetic waves, while in plasmonic MMs, it modifies surface plasmon resonance (SPR) conditions. By varying the strength of the applied field, the LC alignment can be continuously adjusted, allowing for real-time tuning of the MM's properties. This integration mechanism leverages the anisotropic permittivity of LCs, meaning their electrical properties vary depending on the direction of measurement, making them ideal for creating tunable and reconfigurable MM devices.

### 3.1. Integration approaches of LCs with MMs

The integration of LCs with MMs has opened new avenues for real-time tunability and reconfigurability in electromagnetic devices. Owing to their strong sensitivity to external stimuli such as electric fields, temperature variations, and mechanical stress, LCs can dynamically modify the electromagnetic response of MM structures. Several integration strategies have been developed to effectively couple LC behaviour with MM resonances. These strategies are commonly classified into four main approaches: layered structure integration, embedded (or infiltrated) integration, microfluidic-based dynamic integration, and hybrid material system integration.

#### *3.1.1. Layered structure integration*

In layered configurations, an LC layer is deposited adjacent to or between the MM resonator structure and a transparent electrode, typically an indium tin oxide (ITO)-coated substrate. When an external voltage is applied, the orientation of the LC molecules changes, leading to a tunable effective refractive index and dielectric permittivity in proximity to the resonator. This results in a measurable shift in the resonance frequency.

This is the most manufacturable of the four strategies, since it reuses the electrode geometry and cell-gap architecture of conventional LC displays, and it is consequently the configuration adopted in the majority of microwave and terahertz demonstrations reviewed in section 3.4. Its intrinsic limitation is that only the evanescent tail of the resonant field overlaps the LC volume, so the tuning obtained per unit LC thickness is the lowest of the four approaches. Increasing the layer thickness to compensate directly degrades the switching speed, which is the trade-off quantified for SRR devices by Chiang *et al* [66] and Wang *et al* [67]. Layered integration should therefore be regarded as the default, low-risk

option, adopted unless a specific application demands the larger tuning or spatial addressability offered by the remaining strategies.

*3.1.2. Embedded or infiltrated structures*

A stronger interaction is achieved when LCs are directly infiltrated into micro- or nano-scale cavities within the MM. In this embedded approach, LC molecules fill the gaps (for example, within the split gaps of SRRs or through holes in fishnet structures), maximizing their influence on the localized electromagnetic fields.

Because the LC occupies precisely the region where the resonant field is most concentrated, this approach delivers the largest tuning per unit LC volume, and it underlies the infiltrated SRR and fishnet devices discussed in sections 3.4.3 and 3.4.4 [68, 69]. The penalty is imposed by the physics described in section 2.1: in sub-micrometre gaps the elastic energy of reorientation competes with the surface anchoring energy, so only a fraction of the confined LC actually switches and the measured tunability falls systematically below the bulk-$\Delta n$ limit. Uniform infiltration of closed cavities is also difficult to verify experimentally. The approach is well established at microwave and terahertz frequencies but becomes progressively harder to implement as feature sizes approach the optical regime. It is the strategy of choice when tuning range is the dominant design requirement.

*3.1.3. Microfluidic-based dynamic integration*

Microfluidic channels enable the controlled delivery and spatial patterning of LC materials within MM architectures. This method is particularly beneficial for pixelated or gradient-index metasurface designs, where local tuning of electromagnetic properties is required.

The distinguishing advantage of this route is spatial control rather than tuning magnitude: soft lithography combined with microfluidics achieves feature resolutions of about 1 $\mu$m at low cost and provides excellent channel-level control, as summarized in the fabrication comparison of section 3.2. It is therefore the only one of the four strategies that natively supports pixelated and gradient-index architectures, which are prerequisites for spatial light modulators and large-area RISs. The principal difficulties are practical rather than physical, namely complex sealing and the verification of LC filling uniformity across many channels. Reported device-level demonstrations remain considerably fewer than for layered or embedded integration, so the approach is best described as an enabling fabrication route at an earlier stage of validation rather than an established device platform.

*3.1.4. Hybrid material systems: nanoparticles and conductive polymers*

The integration of LCs can be further enhanced by the addition of nanoparticles or conductive polymers. The incorporation of metal nanoparticles (e.g. Au, Ag, PbS quantum dots) or conductive polymers (e.g. P3HT, PEDOT: PSS) within the LC host can modify the dielectric anisotropy and optical response, leading to improved tunability and reduced losses.

Hybrid integration differs from the preceding three approaches in that it modifies the LC medium itself rather than its geometrical arrangement, and the two can therefore be combined freely. Ferroelectric nanoparticle doping has been shown to raise the terahertz birefringence to 0.360, exceeding that of most undoped mixtures (table 2) [57], and nanoparticle-doped nematics additionally exhibit hysteresis and optical memory effects that are unavailable in the pure host [70]. The limitations are those of any colloidal system: particle aggregation compromises alignment homogeneity, added conductive species increase ionic conductivity and scattering loss, and long-term colloidal stability remains largely uncharacterized, all of which bear directly on the degradation mechanisms discussed in section 3.4.9. Reported work is accordingly concentrated at the materials level, with comparatively few complete device demonstrations. Hybrid integration is best positioned as a materials-side lever that complements, rather than replaces, the geometrical strategies.

### 3.2. Fabrication of LC-enhanced MMs

The fabrication of LC-enhanced MMs has evolved significantly, employing various lithographic techniques to achieve precise and scalable structures. The initial demonstrations of functional LC integration utilized conventional lithography and assembly methods. Key pioneering work, such as that by Zhao *et al* [71], first established the fundamental feasibility of using LCs to achieve active tuning in microwave SRRs. This was followed by influential studies, including Decker *et al* [72], who demonstrated electro-optical switching in gold SRR-based metasurfaces at optical frequencies, marking a transition toward high-frequency applications. These early methods laid the groundwork for the adoption of more advanced, high-resolution techniques. Among these, photolithography, EBL, and FIB milling have

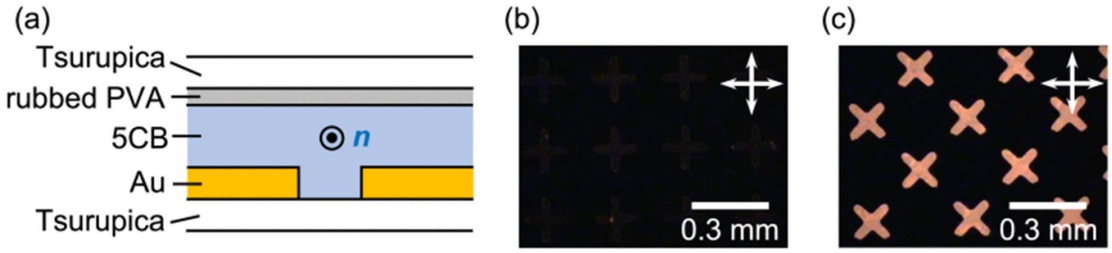



**Figure 3.** (a) Cross-sectional schematic (*xz*-plane) of the LC-embedded gold mesh metamaterial. (b) Polarization optical microscope (POM) image showing the dark state. (c) POM image showing the bright state. These images demonstrate the successful infiltration of the nematic liquid crystal (5CB) into the resonator gaps (embedded integration). The dynamic transition between dark and bright states under external stimuli serves as direct visual evidence of subwavelength polarization modulation and strong light–matter interaction within the embedded architecture. Reproduced from [73]. CC BY 4.0.

been the most prominent methods, each offering distinct advantages in terms of resolution, cost, and scalability.

Photolithography remains a widely used technique, particularly in industrial settings. In a typical process, a metal film (e.g. gold or copper) is deposited on a silicon or glass substrate. A patterned photoresist is then applied, then exposed to UV light through a mask to define the desired pattern. Chemical etching removes unexposed metal, and spacers are added to form an LC cell. Finally, the cell is filled with LCs. This method is favoured for its cost-effectiveness and compatibility with large-area processing.

A notable example of the embedded (infiltrated) integration approach fabricated via photolithography is the work of Sasaki *et al* [73], who used photolithography to create a gold mesh on a transparent Tsurupica resin substrate, as shown in figure 3. In this configuration, the 5CB LC (4-Cyano-4'-pentylbiphenyl) was injected directly into the apertures of the mesh, and a polyvinyl alcohol alignment layer was applied to control the molecular orientation. This direct infiltration of LC into the structural gaps of the resonator maximizes the overlap between the LC and the localized electromagnetic field—a defining characteristic of the embedded integration strategy.

Meanwhile, Kowerdziej *et al* [74] designed a plasmonic MM composed of metallic nano-islands hybridized with a 1.8 $\mu$m-thick dual-frequency LC (DFLC) layer, operated via in-plane switching.

For applications demanding higher precision, EBL is employed. For example, Decker *et al* [72] fabricated an LC-MM cell with gold SRRs arranged in a 300 nm-separated periodic array on a glass substrate. A 5 nm ITO coating was applied, and the structures were defined using EBL. Such cells demonstrate rapid transitions between electric and magnetic resonances when the LC molecules realign under an external field. Sharma *et al* [75] utilized EBL to fabricate plasmonic metasurfaces on ITO-coated glass substrates, creating rod-shaped and cross-shaped nanoantennas with 180 nm periodicity. Wu *et al* [76] introduced a mechanics-guided fabrication method for LCE MMs, achieving uniform molecular alignment through biaxial stretching and integrating the structures into biocompatible wound healing applications.

FIB milling has also been extensively used for nanoscale MM fabrication. Buchnev *et al* [77] developed an electro-optical cell by positioning an ITO-coated cover glass 15 $\mu$m above a MM structure. This MM consisted of a zigzag pattern of V-shaped plasmonic resonators, fabricated via FIB milling on an 80 nm gold film deposited on a glass substrate. A similar approach was taken by Buchnev *et al* [78], where a double-periodic array of V-shaped resonators was fabricated on a silicon nitride (SiN) membrane, as shown in figure 4. This MM was integrated into an LC cell with ITO electrodes, allowing dynamic tuning of plasmonic resonance via an applied electric field.

In contrast to the embedded configurations described above, Lee *et al* [79] employed a layered integration approach, in which the LC material acts as a tunable dielectric layer sandwiched between the metasurface and a substrate, rather than being infiltrated into the resonator gaps. Specifically, FIB milling was used to create a metasurface: first forming a 12 $\mu$m gap LC cell using polyimide-coated ITO glass and a rubbed polyvinyl alcohol-coated fused quartz substrate, as shown in figure 5. The cell was filled with ZLI-2293 nematic LC, and a negative metasurface was fabricated by e-beam evaporating a 30 nm-thick Au film onto a fused quartz substrate. Nano-sized double-split ring resonator (DSRR) arrays were then patterned using FIB milling. In this layered geometry, the LC layer modifies the effective electromagnetic environment of the underlying resonator through changes in refractive index upon molecular reorientation, without the molecules being directly confined within the structural features of the MM.

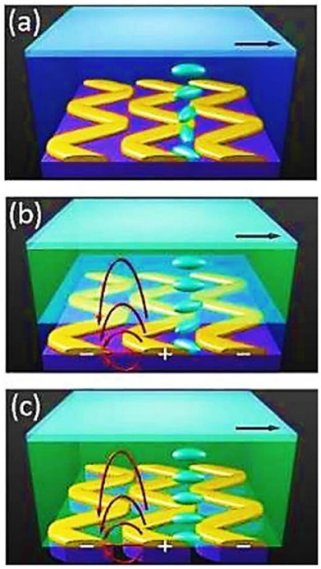



**Figure 4.** Schematic representation of a hybrid liquid crystal cell with a nanostructured metasurface. The cell is controlled by applying in-plane voltages. (a) In the off state, the liquid crystal in the bulk is twisted. (b) In the on state, the liquid crystal changes to a flat, planar arrangement (shown in green). However, a very thin layer at the bottom (shown in blue) remains slightly twisted due to strong surface anchoring. (c) When the metasurface is suspended, the liquid crystal is fully planar both in the bulk and over the metasurface. A black arrow indicates the rubbing direction that sets the LC alignment on the top cover. Reproduced from [78]. CC BY 4.0.

Advancements in MM fabrication have also incorporated hybrid techniques, such as a combination of atomic layer deposition (ALD) and photolithography. As a demonstrative hybrid approach, researchers have introduced graphene-integrated LC MM modulators by layering a gold substrate with an amorphous silicon sheet, a dielectric layer, and a highly transparent graphene electrode. The metasurface modulator is patterned using EBL, optimizing the light–matter interaction in terahertz and infrared regimes while the graphene provides a uniform static electric field for homogeneous LC alignment.

Mirbagheri's team [80] used plasma-enhanced chemical vapour deposition (PECVD) to deposit the initial silicon oxide and amorphous silicon layers, followed by reactive ion etching with HBr and oxygen gases to create the nanodisk structures.

Innovations in 3D printing have further expanded LC-MM fabrication possibilities. Techniques such as stereolithography (SLA), TPP, and direct ink writing (DIW) offer high-resolution manufacturing capabilities [81]. Lv *et al* [82] utilized DIW to design a tunable LC-enhanced MM filter, achieving frequency tuning via applied voltage.

Hybrid manufacturing approaches, such as the integration of soft lithography and microfluidics, enable the capillary filling of LC materials into pre-formed MM structures. This combination enables the creation of microchannels with patterned polymer structures via soft lithography and the precise filling of these channels with LC via microfluidic systems, so that complex three-dimensional MM architectures can be achieved. This method enables precise alignment and controlled operation thanks to integrated electrodes. In order to improve device performance, Wang *et al* [83] patterned aluminum electrodes on fused silica wafers by photolithography and etching methods, and integrated LCs into the system by placing them by capillary effect and sealing with vacuum.

Recent advances also include Park *et al* [84], who developed an LC-based antenna for wave beam-steering, achieving a 120° steering range with a 10.754 dB gain. Their voltage-controlled 32-unit cell design eliminates the need for phase shifters, reducing power consumption while enhancing scalability.

In summary, the fabrication of LC-enhanced MMs encompasses a diverse range of techniques, from traditional photolithography to advanced nanoscale methods such as EBL and FIB milling. Emerging approaches, including 3D printing and hybrid integration strategies, provide greater flexibility and precision, driving innovations in telecommunications, sensing, and optics. However, it must be noted that yield and reproducibility data are rarely reported in the LC-MM fabrication literature. EBL-fabricated

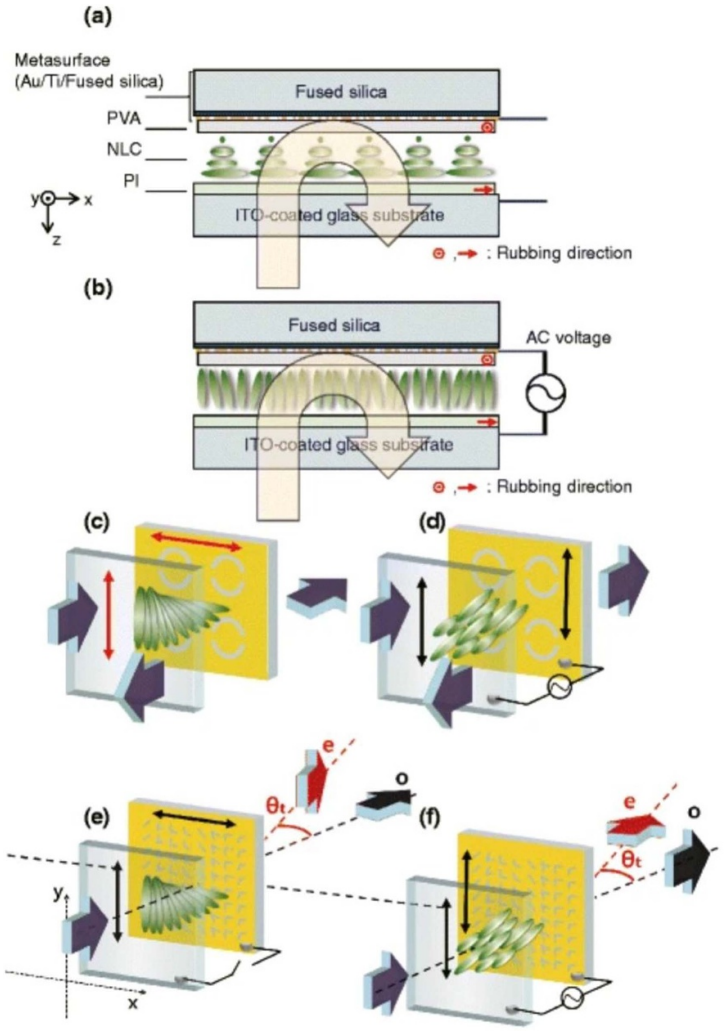



**Figure 5.** Electromagnetic wave manipulation through layered LC-metasurface integration. (a) Cross-sectional view of the initial structure comprising an ITO-coated glass substrate, PI layer, PVA-coated fused silica, and a nematic LC layer. (b) Application of an AC voltage across the LC cell. (c) Reorientation of LC molecules in response to the applied electric field. (d) Dynamic manipulation of the electromagnetic wave propagation direction as a direct result of the LC reorientation. (e) The metasurface directing the wave to a specific angle ($\theta_t$) based on the aligned state. (f) Fine-tuning the metasurface's reflection or transmission response by continuously adjusting the LC alignment Reproduced from [79]. CC BY 4.0.

structures from independent groups operating at nominally identical geometries frequently exhibit resonance frequency discrepancies of 5%–15%, suggesting that cell gap variation, LC infiltration completeness, and alignment layer quality, none of which are standardized across the field, are significant uncontrolled variables. This absence of standardized fabrication reporting protocols represents a systemic barrier to cross-laboratory comparison and field-wide progress toward industrialization.

### 3.3. Fabrication scalability and commercialization prospects

The fabrication techniques reviewed in the preceding subsections, photolithography, EBL, FIB milling, nanoimprint lithography, and 3D printing, each demonstrate clear proof-of-concept capability for LC-integrated MM devices. However, transitioning these laboratory demonstrations to manufacturable, commercially viable products requires confronting a set of scale-specific challenges that are distinct from the resolution and precision concerns addressed in the research literature. This subsection critically examines five principal barriers to large-scale production and outlines realistic pathways toward industrial adoption.

The most persistent fabrication challenge is achieving uniform LC molecular alignment within the sub-micron gaps and cavities of resonator arrays. Conventional mechanical rubbing of polyimide alignment layers, the industry standard in liquid crystal display (LCD) manufacturing, is destructive to delicate metallic nanostructures and fails to provide uniform anchoring near sharp metallic edges. Photoalignment via polarized UV exposure offers a non-contact alternative that preserves nanostructure integrity and achieves alignment uniformity within deep nanocavities, reducing optical losses by up to

60% compared to mechanical rubbing. SAMs applied to metallic surfaces provide an additional means to fine-tune anchoring energy and reduce threshold voltage by 20%–40% [64]. However, both approaches introduce additional process steps, specialized equipment, and material costs that must be factored into production economics.

In patterned metasurface architectures used directly as electrodes, spatially non-uniform electric fields arise at resonator edges, leaving LC molecules near boundaries partially unreoriented or requiring excessively high drive voltages. Insertion of a continuous transparent electrode interlayer, such as few-layer graphene (>98% THz transparency, ∼400 Ω $sq^{-1}$ sheet resistance with the underlying metasurface) or thin-film ITO (<5 nm), resolves this issue but requires additional deposition and patterning steps [65]. At the wafer scale, ensuring electrode uniformity across areas of tens to hundreds of $cm^2$ remains an open engineering challenge.

EBL and FIB milling—the highest-resolution techniques capable of defining sub-10 nm features—are inherently serial, single-point processes with throughputs of order 1–10 $mm^2$ per hour. These are wholly impractical for production volumes. Roll-to-roll nanoimprint lithography (R2R-NIL) offers a fundamentally different scaling pathway: continuous substrate processing at web speeds of 1–10 m $min^{-1}$, with demonstrated feature sizes below 50 nm. The critical technical requirement is a defect-free master mould, since any mould imperfection is replicated across every imprinted substrate. For the near-term commercialization targets, FSS-based tunable radomes and Ka-band reflect arrays, where feature sizes are in the 100 $\mu$m range, conventional photolithographic processes adapted from the display industry are already sufficient, enabling large-area (>1 $m^2$) patterning at low cost with established yield metrics [85].

Current LC-MM device fabrication costs are estimated at 10–100× higher per unit area compared to conventional LCD panels of equivalent dimensions, primarily owing to the lithographic patterning of resonator arrays and the multistep alignment and cell assembly process. This cost gap narrows substantially for microwave and millimetre-wave applications, where the resonator feature sizes (100 $\mu$m–1 mm) are compatible with screen-printing or inkjet-printed metallic inks, process technologies already deployed at scale in RFID and flexible electronics manufacturing. For THz and optical applications, where submicron features are mandatory, cost reduction requires investment in NIL master mould infrastructure and high-throughput UV-NIL tools currently being developed for the semiconductor packaging and display industries.

Performance drift under temperature cycling (−40 °C to +85 °C), UV exposure (>500 h per JEDEC JESD22-A101), and humidity (85 °C/85% RH) remains a critical barrier to outdoor deployment in telecommunications and radar applications. Hermetic encapsulation using glass frit bonding or ALD-deposited barrier layers ($Al_2O_3$, ∼10 nm) effectively limits moisture ingress and extends operational lifetime. Qualification against military (MIL-STD-810) or automotive (AEC-Q100) standards has not yet been demonstrated for LC-MM devices and represents a necessary step prior to commercialization in demanding environments.

Based on the above analysis, the most realistic near-term path to commercial viability proceeds in three stages: (i) proof-of-production at the Ka-band and mmWave using photolithographic patterning on display-grade glass substrates with standard LC cell assembly, targeting reconfigurable radome and 5 G/6 G beam-steering reflect array applications; (ii) cost reduction through adoption of R2R-NIL for THz-band FSS arrays, leveraging the existing nanoimprint infrastructure being developed for advanced packaging; and (iii) full optical integration via wafer-scale EBL replacement by deep-UV (DUV) stepper lithography for optical metasurface arrays, following the roadmap established by the metalens commercialization community. Each stage builds on the manufacturing infrastructure of an established adjacent industry, displays, RF electronics, and semiconductor optics respectively, minimizing the greenfield capital investment required. A comparative assessment of these fabrication techniques is provided in table 4.

### 3.4. Recent advances in LC-enhanced MMs

The integration of LCs with artificial electromagnetic structures has produced substantial device-level advances. To maintain rigorous terminology throughout this section, a strict distinction is observed: metasurfaces refer to 2D planar arrays providing abrupt interfacial phase/amplitude modulation, whereas MMs refer to three-dimensional volumetric structures exhibiting bulk effective medium properties.

While LC integration manifests differently across various geometries—from volumetric SRRs and fishnets to planar FSS and chiral metasurfaces—a unifying application thread throughout these designs is their collective push toward next-generation wireless communications. Specifically, dynamic terahertz (THz) modulation, advanced telecommunications routing, and adaptive signal filtering serve as the primary operational targets connecting these diverse structural approaches.

Furthermore, to address the vast scope of these technologies, the recent advancements discussed below are explicitly categorized into three technologically significant application domains: (i) spatial

**Table 4.** Comparative assessment of fabrication techniques for LC-integrated metamaterials.

| Technique | Resolution | Scalability | LC alignment compatibility | Estimated cost | Throughput | Key limitation |
|---|---|---|---|---|---|---|
| Photolithography | >1 $\mu$m | High (Mass Production) | Good (Planar) | Low–Medium | High | Diffraction limit restricts optical applications [86, 87]. |
| Electron Beam Lithography (EBL) | <10 nm [88] | Low (Slow Serial Writing) | Excellent | Very High | Very Low | Not scalable to large area; slow; high cost [89]. |
| Focused Ion Beam (FIB) | <10 nm | Low | Moderate | Very high | Very low | Ion contamination; substrate damage; slow [90, 91]. |
| Nanoimprint Lithography (NIL) | <50 nm | High (roll-to-roll) | Good | Medium | High | Requires high-quality master mould; defect replication [92]. |
| 3D Printing (TPP/DLW) | <100 nm | Moderate | Excellent (volumetric) | Medium–High | Low–Moderate | Limited material choice; slow for large areas [60]. |
| Soft Lithography + Microfluidics | ~1 $\mu$m | Moderate | Excellent (channel control) | Low | Moderate | Complex sealing; LC filling uniformity |

light modulation (SLM) (e.g. beam steering, holography), (ii) optical and spectral filtering (e.g. dichroic filters, tunable absorbers) [93], and (iii) display and colour technologies (e.g. structural colour, micro-displays) [94–104].

*3.4.1. LC-enhanced high-Q resonators and plasmonics*

The integration of LCs with plasmonic nanostructures primarily targets display technologies, SLM, and high-sensitivity spectral filtering. While passive plasmonic arrays exhibit strong surface lattice resonances (SLRs) and localized SPRs, their fixed geometries limit them to a single operational band. Integrating LCs introduces a dynamic dielectric matrix. When an external electric field is applied, LC molecules realign, modifying the medium's anisotropic properties. This voltage-controlled molecular rearrangement dynamically tunes the plasmonic resonance wavelengths and light scattering properties, transforming static arrays into active photonic components.

The underlying physics is that of localized and lattice SPRs: the resonance condition of a metallic nanostructure depends sensitively on the refractive index of the surrounding dielectric, with the spectral sensitivity commonly expressed in nm per refractive-index unit (nm/RIU). Because the reorientation of an LC director can change the index experienced by the near-field by up to $\Delta n \approx 0.2$–$0.4$, embedding the plasmonic array in an LC matrix converts this passive index sensitivity into an actively addressable spectral shift. The magnitude of the achievable shift is set by the overlap between the plasmonic near-field, which decays within tens of nanometres of the metal surface, and the LC volume that actually reorients, which is precisely the region where surface anchoring is strongest; this competition defines both the promise and the difficulty of plasmonic LC devices.

In the domain of display and colour technologies, the integration of noble metal nanoparticles (such as gold and silver) into LC environments forms structures with highly tunable plasmonic properties [105]. For instance, anisotropic particles like gold nanorods provide polarization-dependent responses [106]; Chu *et al* [107] demonstrated that the simultaneous adjustment of transverse and longitudinal plasmonic modes allows for voltage-controlled spectral shifts, providing the high-contrast colour modulation essential for micro-displays and virtual retina displays. Building on this concept of spatial and colour modulation, fully integrated voltage-controlled devices have been developed using imprinted plasmonic surfaces. As illustrated in figure 6, sandwiching an active LC layer between conventional LCD components and a plasmonic substrate allows for the independent, real-time control of localized sub-wavelength regions, enabling actively addressed full-colour pixels [108]. Extending this to multi-state systems, Sharma *et al* [109] designed gold nanoantenna arrays supporting SLRs in the visible and near-infrared regimes. By applying a minimal electrical bias of just 2 V, they achieved a modulation depth exceeding 50% at resonance dips, highlighting the efficiency of hybrid systems over conventional LCDs.

Addressing spatial light amplitude modulation and optical switching, terahertz plasmonic metasurfaces have shown exceptional performance. Yang's team [101] developed a tunable dual-layer plasmonic

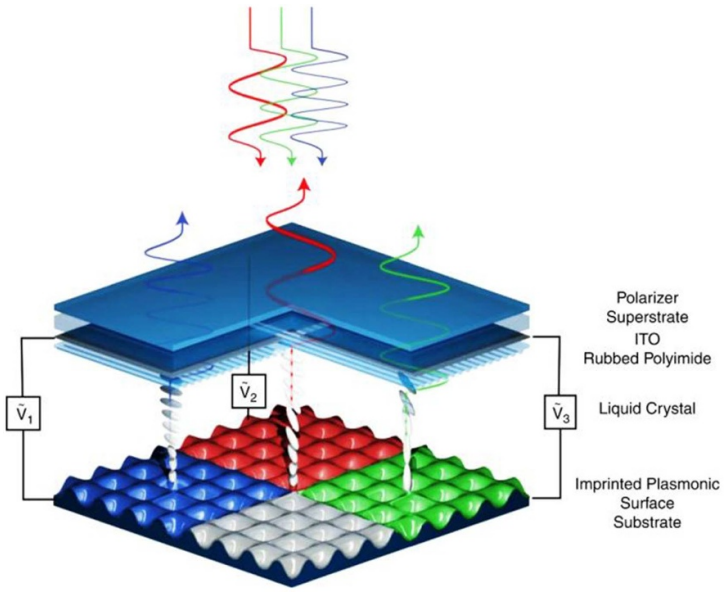



**Figure 6.** Schematic illustration of a voltage-controlled liquid crystal device with an imprinted plasmonic surface. The multi-layer structure shows the integration of conventional LCD components with a plasmonic substrate, demonstrating independent control of different regions through applied voltages. The coloured waves represent light interaction with the device structure Reproduced from [108]. CC BY 4.0.

**Table 5.** Quantitative performance metrics of representative LC-integrated plasmonic and high-Q resonators.

| Device architecture | Operating band | Tuning mechanism | Key technical performance metric | References |
|---|---|---|---|---|
| Terahertz Plasmonic MM | Terahertz | Voltage Control | 96% amplitude modulation depth; 9.35% frequency tunability | [101] |
| Gold Nanorods in LC | Visible | Transverse/Longitudinal | High-contrast colour modulation for micro-displays | [107] |
| Gold Nanoantenna Array (SLR) | Visible/NIR | Electrical Bias (2 V) | >50% modulation depth at resonance dips | [109] |
| LC-SPR Multilayer Sensor | Optical | Molecular Alignment | Significant enhancement in biological detection sensitivity | [111] |

MM operating in the THz spectrum, achieving an extraordinary 96% amplitude modulation depth and over 9.35% frequency tunability. Furthermore, both volume switching and in-plane switching mechanisms (where electric fields are applied parallel to the substrate surface) provide effective control of optical properties. Buchnev's study [77] showed that combining these mechanisms can eliminate the need for basic components of traditional LC devices (such as alignment layers, transparent electrodes, and polarizers). As emphasized by Abdulhalim [110], this enhanced control over interactions between LCs and subwavelength gratings or porous materials enables the miniaturization of classical optical components, allowing for seamless integration into compact nanophotonic circuits.

In sensing applications—a vital subset of spectral filtering—LC-SPR structures offer significant advantages for medical diagnostics and biochemical analysis. Vahedi and Kouhi [111] utilized alternating metal-LC multilayer configurations for SPR biosensors. Their results proved that the dynamic molecular alignment of LCs significantly amplifies the refractive index sensitivity compared to static bare-metal SPR sensors, particularly when utilizing silver layers. Because LC properties are highly sensitive to the presence of analytes, these hybrid structures modulate the optical response efficiently, providing robust platforms for environmental monitoring and high-sensitivity biological detection. Quantitative performance metrics of these representative LC-integrated plasmonic and high-Q resonators are summarized in table 5.

The extreme field confinement of plasmonic resonances converts nanometre-scale LC volumes into large spectral shifts. This is why modulation depths of 96% with 9.35% frequency tunability [101], and >50% modulation at only 2 V [109], are achievable in this family. The platform is also naturally matched to display and colour applications [107] and to refractive-index sensing [111]. Ohmic loss in noble metals fundamentally caps the attainable quality factor. In addition, strong anchoring on chemically heterogeneous nanostructured metal restricts the fraction of LC that actually reorients within the

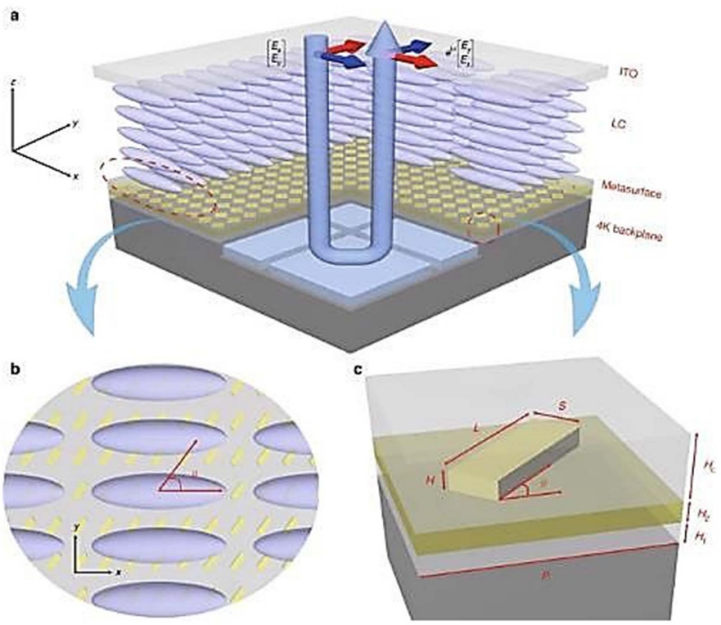



**Figure 7.** Schematic representation of a liquid crystal on silicon (LCoS) spatial light modulator, showing (a) the layered device structure, (b) the molecular LC alignment within the cell, and (c) the unit cell geometry. This configuration demonstrates the dynamic control of light–matter interaction enabled by integrating tunable LC layers with metasurface resonators. Reproduced from [115]. CC BY 4.0.

decay length of the near-field, so measured tunability remains systematically below the bulk-$\Delta n$ limit. The field has produced advanced laboratory demonstrations with well-characterized performance metrics (table 5), but no commercial device has yet emerged. Plasmonics currently offers the most developed route to tunability in the visible range, although for high-efficiency applications it is likely to be progressively displaced by low-loss all-dielectric Mie-resonant metasurfaces.

### *3.4.2. LC-enhanced 2D planar metasurfaces*

Planar metasurfaces excel at manipulating wavefronts (phase, amplitude, and polarization) at a subwavelength interface [112, 113]. While traditional metasurfaces are powerful, they are fundamentally limited by their static nature; once fabricated, their optical response is permanently locked. The integration of LCs addresses this limitation by introducing dynamic tunability without compromising the ultra-thin form factor [114]. While planar metasurface architectures vary widely depending on the target frequency and desired wavefront manipulation, traditional liquid crystal on silicon (LCoS) systems are widely used as spatial light modulators. As shown in the illustrative example in figure 7, when subjected to external stimuli, LCs reorient their molecular alignment. This alters the local anisotropic permittivity tensor, modifying the resonance conditions of the metasurface unit cells and enabling precise, active control over the electromagnetic waves [115].

The operating principle of all LC-tunable planar metasurfaces can be reduced to a single relation: each meta-atom imposes a local, resonance-mediated phase (and amplitude) on the transmitted or reflected wave, and this phase depends on the effective permittivity of the LC superstrate or interlayer. Voltage-driven director reorientation therefore rewrites the spatial phase profile $\varphi(x, y)$ of the entire surface, which is the quantity that determines beam steering angles, hologram content, and focal behaviour. The essential difference from a conventional LCoS modulator is that the resonant meta-atoms provide the required 0–2$\pi$ phase excursion within an LC layer one to two orders of magnitude thinner, with proportionally faster switching.

In the realm of SLM and dynamic wavefront control, LC-integrated metasurfaces offer unprecedented precision. Combining the subwavelength spatial resolution of a metasurface with the continuous phase modulation of an LC layer enables advanced beam manipulation. This is particularly promising in terahertz (THz) technologies. For example, Wu *et al* [29] demonstrated an LC-integrated metasurface capable of programmable beam manipulation with deflection angles up to 32°, while other designs have successfully generated tunable polarization vortex beams [116]. These capabilities directly address critical challenges in next-generation wireless communication, high-resolution sensing, and radar systems.

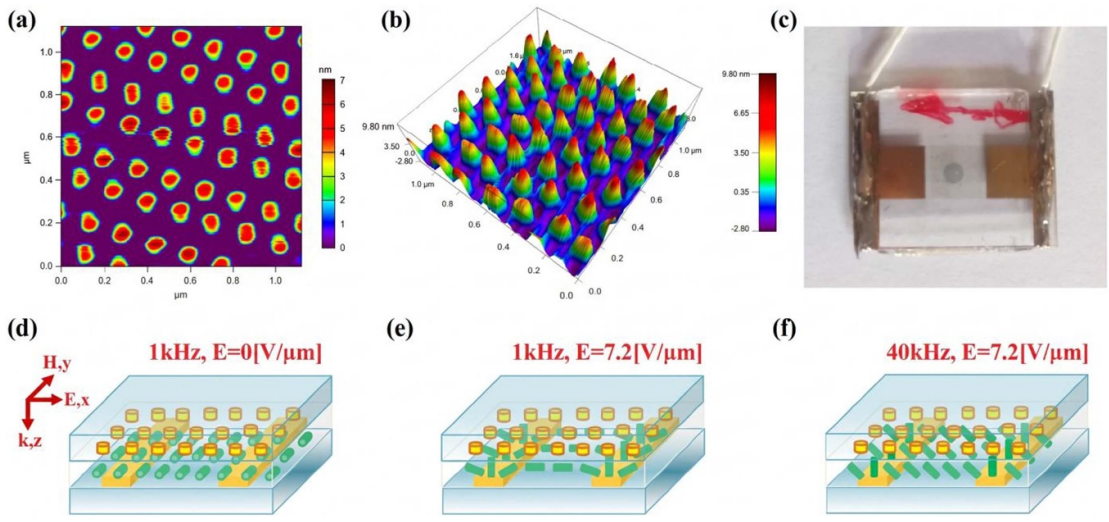



**Figure 8.** Schematic representation of the tuning mechanism in a dual-frequency liquid crystal (DFLC)-integrated metasurface. The LC molecules reorient differently depending on the frequency of the applied electric field (e.g. 1 kHz vs 40 kHz), enabling ultrafast bidirectional switching without relying on slow natural relaxation. Reproduced from [74]. CC BY 4.0.

For display technologies and dynamic holography, 2D metasurfaces operating in the visible and infrared domains have shown remarkable potential. While passive systems are limited to static capabilities—such as fixed structural colours and pre-defined metaholograms [34, 117]—LC hybridization allows these optical responses to be actively and dynamically switched. Beyond mere tunability, a critical parameter for practical display applications is the response time. By integrating DFLC mixtures with metasurfaces, researchers have achieved switching times as fast as 1.89 ms [74], as illustrated by the tuning mechanism in figure 8. This rapid modulation addresses a major limitation of earlier designs, directly paving the way for real-time, video-rate holographic displays and reconfigurable optical components.

In the context of optical and spectral filtering, diverse architectures and control mechanisms have expanded device functionalities beyond traditional electrical fields. For instance, binary-grating structures combined with nematic LCs demonstrate tunable diffraction efficiencies [118], while silicon nanodisk arrays embedded in LC environments provide significant spectral shifting with moderate applied voltages [100]. Moreover, alternative control mechanisms have emerged: three-dimensional magnetic field orientation provides unprecedented freedom in manipulating electric and magnetic resonances independently [119]. Photoalignment techniques enable all-optical control, eliminating the need for metallic electrical connections [120]. Among the diverse array of resonator designs employed for all-optical control, circular SRRs represent a highly effective geometry. For example, using photo-aligned LCs over such specific structures (as depicted in the representative schematic in figure 9), researchers have achieved highly efficient tunable THz filtering with wide frequency ranges [120].

In the terahertz absorber domain, the integration of graphene with asymmetric cross-shaped LC-metasurfaces has yielded exceptional amplitude and frequency modulation capabilities. By applying a moderate bias of 10 V, researchers achieved a broad frequency tunability from 0.75 to 1.0 THz. Furthermore, this hybrid architecture demonstrated an impressive amplitude modulation depth of approximately 80% at 1 THz, highlighting its potential for high-efficiency, fast-switching THz spatial light modulators [65].

To summarize the recent advancements and quantitative capabilities of these planar and dielectric architectures, table 6 outlines the performance metrics of prominent LC-integrated THz metadevices.

This family offers full wavefront programmability in an ultrathin form factor, with demonstrated beam deflection up to 32°, phase excursions exceeding 180° [121], and switching as fast as 1.89 ms [74] using dual-frequency mixtures. The architecture also inherits the manufacturing maturity of LCoS display technology, and control is not restricted to electrical bias, since magnetic and photoaligned all-optical addressing have both been demonstrated. Independent pixel-level addressing of individual meta-atoms nevertheless remains the principal unsolved engineering problem. Resonant phase modulation is also intrinsically accompanied by amplitude variation that degrades hologram fidelity, and diffraction efficiency falls at large steering angles. Overall, planar metasurfaces constitute the most technologically

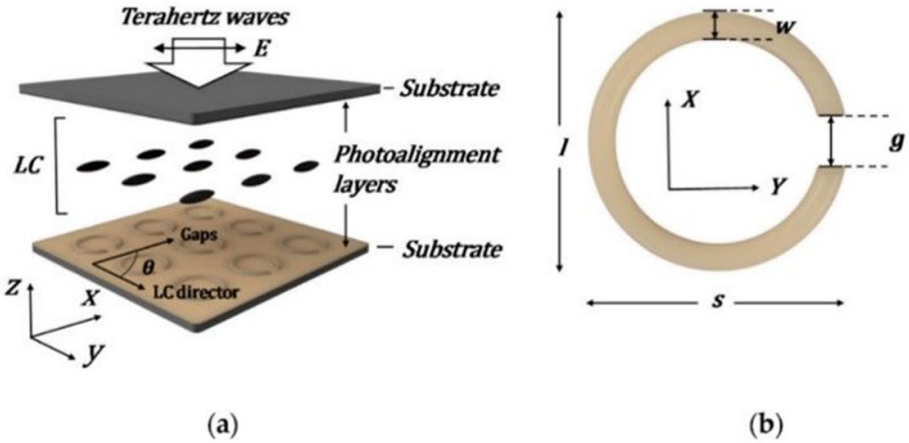



**Figure 9.** Structural schematic of the designed circular-ring terahertz resonator (a) together with the photo-alignment layers of liquid crystal (LC) material (b) for terahertz wave modulation. Reproduced from [120]. CC BY 4.0.

**Table 6.** Technical metrics of LC-integrated dielectric THz Metadevices.

| Architecture | Material base | Stimulus | Functional outcome | Technical value |
|---|---|---|---|---|
| Si Metasurface | High-res. Silicon | Magnetic | Beam steering | 25°–45° deflection [122] |
| Bilayer Metasurface | Cascaded LC-Si | Magnetic | Beam scanning | ±35° to ±75° range [123] |
| Dielectric Metalens | Si/Graphene | 75 V Bias | Focal length tuning | Achromatic focus (0.9–1.4 THz) [124] |
| Microsphere Absorber | Zirconia | Magnetic | Tuning FoM | FoM optimized to 6.67 [125] |
| Anisotropic MS | Dielectric + LC | Electric | Phase control | >180° phase-shift range [121] |
| Achromatic Wave Plate | DFLC + Dielectric | 1–90 kHz AC | Broadband phase diff. | High circular dichroism (30 dB) [126] |

advanced family after FSS, having reached the pre-commercial prototype stage for beam steering and holographic display. They are the leading candidate for consumer-facing applications of LC-MM technology, particularly augmented reality (AR)/virtual reality (VR), LiDAR, and dynamic holography.

*3.4.3. LC-enhanced 3D and bulk MMs*

SRRs are the foundational building blocks of bulk MMs, engineered to produce tailored magnetic responses not found in natural materials [127]. While three-dimensional SRR designs span a vast array of shapes—including square, U-shaped, and multi-ring geometries depending on the required magnetic resonance—a classic and widely referenced representative architecture consists of concentric metallic rings with slits etched on opposing sides (figure 10). The gap between the rings introduces a distributed capacitance that lowers the resonant frequency well below what the physical dimensions alone would suggest, yielding high quality-factor resonators with minimal radiative loss [128, 129]. When arranged in periodic arrays, SRR-based structures can exhibit negative effective permeability in targeted frequency bands, enabling the realization of negative refractive index media—a property absent in any naturally occurring material. In circuit terms, each SRR behaves as a subwavelength resonant circuit formed by the loop inductance $L$ and the gap capacitance $C$, with a resonance frequency $f_0 = 1/(2\pi\sqrt{(LC)})$ that is dominated by $C$ [128]; because the electric field is concentrated precisely in this gap, infiltrating it with a LC places the tunable dielectric where it exerts maximum leverage on $f_0$.

Although isolated SRRs deliver a well-defined resonant response, their operating frequency is fixed by geometry and cannot be adjusted after fabrication. This is the fundamental limitation that LC infiltration addresses. Unlike a bare metasurface, which interacts with electromagnetic waves only at its patterned interface, a 3D SRR-based MM couples to the LC medium throughout its volumetric bulk. The refractive index sensed by the resonator therefore changes with the full dielectric tensor of the LC, providing a larger effective tuning range per unit applied stimulus. Compared to a pure LC medium, which already exhibits appreciable birefringence but lacks structural resonance, the SRR-LC combination translates a modest molecular reorientation into a large, resonance-amplified shift in transmission frequency or phase. This synergy is the core physical motivation for integrating LCs into 3D MM architectures.

Magnetic field tuning: Zhang *et al* [131] demonstrated that nematic LC-filled SRR arrays exposed to external magnetic fields exhibit measurable resonant frequency shifts in the X-band (8–12 GHz). LC molecules reorient along the applied field lines, modifying the local permittivity seen by the fringing

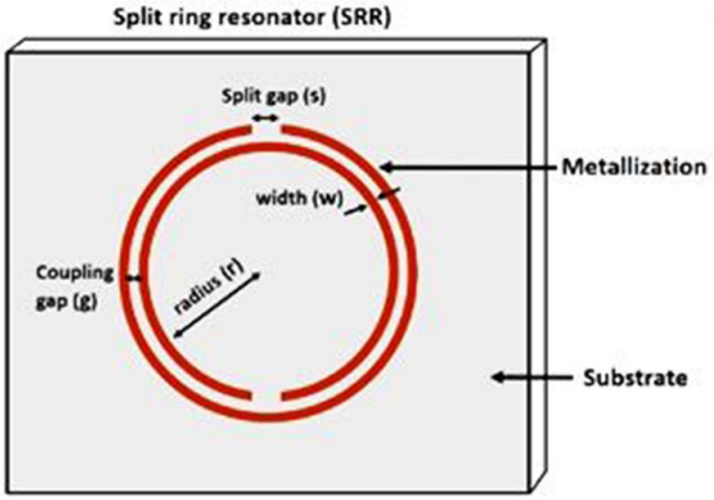



**Figure 10.** Schematic illustration of the key structural components of the SRR. The structure consists of a metallic ring with a split gap ($s$) and a defined width ($w$). The coupling gap ($g$) between the rings critically influences the electromagnetic response of the resonator. The SRRs are typically fabricated on a substrate, with substrate thickness and metallization properties directly affecting device performance. This geometry serves as the fundamental building block of metamaterials, enabling distinctive electromagnetic properties such as negative permeability and frequency selectivity. Reproduced from [130]. CC BY 4.0.

fields of the SRR gap. This contactless control mechanism is attractive for systems in which electrode access is geometrically constrained.

Thermal tuning: Kowerdziej *et al* [132] exploited the temperature-dependent phase transition of nematic LCs to tune the effective permittivity of SRR-based MM structures near 4.9 GHz. As temperature rises toward the nematic-to-isotropic transition, the anisotropy of the LC diminishes continuously, providing a smooth, monotonic tuning handle without the need for applied fields.

Electrical tuning: Electrical bias is the most practically deployable method for SRR-LC systems. Qiu *et al* [69] showed that an SRR covered with an LC droplet achieves a 237 MHz downshift in resonance frequency upon voltage application, accompanied by transmission-phase modulation exceeding 100°. The mechanism is straightforward: the applied electric field aligns LC molecules perpendicular to the substrate, increasing the capacitance of the SRR gap and thereby reducing the resonant frequency. Wang *et al* [67] advanced this approach to the Ka-band (26.5–40 GHz), achieving a continuously tunable resonance shift from 28.5 GHz to 26.1 GHz as the bias increases from 2.5 V to 10 V, with a 150 ms response time enabled by an 11.2 $\mu$m-thin LC layer. Critically, the rapid response is a direct consequence of the reduced LC thickness, illustrating the engineering trade-off between tuning range and switching speed that is particularly pronounced in LC-integrated 3D MMs.

All-optical switching: Atorf *et al* [133] demonstrated optically reconfigurable metasurfaces combining plasmonic SRRs with dye-doped LCs. Visible-light illumination excites the dye molecules, which transfer torque to the surrounding LC mesogens and alter the infrared transmission of the device without any electrical contact. A hybrid alignment configuration, planar on one substrate, homeotropic on the other, creates a pre-tilted LC profile that enhances sensitivity to optical stimuli, reducing the required optical power. This all-optical route to reconfigurability opens pathways toward fully integrated photonic control of MM response.

LC layer thickness optimization: The magnitude of resonance shift is not solely determined by the birefringence of the LC; it also depends on the spatial overlap between the resonant near-field and the LC region. Chiang *et al* [66] showed that, in terahertz SRR MMs, an optimal LC layer thickness of 710 $\mu$m maximizes birefringent interaction while maintaining adequate alignment forces from the polyimide surface layers. Under these conditions, frequency shifts of up to 21 GHz were demonstrated, among the largest reported for thermally and electrically tunable THz MMs.

Colloidal and volumetric 3D structures: Pusovnik *et al* [134] explored soft MM composites in which colloidal SRR particles are suspended directly within an LC host. This approach is inherently three-dimensional, with the LC matrix providing simultaneous mechanical support and optical control. Approximately 5% resonance tunability was achieved via LC birefringence, validating the concept of volumetric MMs in which tuning acts throughout the bulk rather than at a single interface.

Microwave filtering and phase shifting: Beyond resonance-frequency tuning, LC-SRR platforms enable functional signal-processing components. Ding *et al* [135] developed an LC-based microwave phase

shifter that maintains a stable passband from 7.9 to 8.2 GHz while delivering differential phase shifts exceeding 55°. Liu *et al* [136] realized continuously tunable SRR bandpass filters at microwave frequencies using low-bias-voltage LC actuation, a configuration directly compatible with miniaturized communication front-ends.

Sensing: Martinic *et al* [137] employed complementary SRR structures integrated with LCs for label-free dielectric spectroscopy in the 7–10 GHz band. The resonance shift induced by a liquid analyte placed in the SRR gap provides a quantitative measure of permittivity, demonstrating that LC-enhanced MMs can serve as sensitive, non-invasive probes of material properties.

Volumetric overlap between the resonant field and the LC gives this family the largest relative tuning ranges reported in the review, reaching 21 GHz in optimized THz SRR structures [66] and continuous Ka-band tuning from 28.5 to 26.1 GHz at 2.5–10 V [67]. The underlying circuit physics is well understood and transferable across the microwave-to-THz range, with all four stimulus classes experimentally validated [67, 69, 131–133]. Homogeneous LC filling of closed three-dimensional cavities is difficult to achieve and harder to verify, and director alignment inside such cavities is poorly controlled. Furthermore, the thick LC layers required for large tuning impose slow response times, and metallic 3D geometries do not scale to optical frequencies. This family is mature at microwave frequencies, with established proof-of-concept demonstrations at THz. It therefore serves as the reference architecture for fundamental studies and for narrowband microwave and THz components, rather than for large-area reconfigurable apertures.

*3.4.4. LC-fishnet MMs*

Fishnet MMs, metallic multilayer structures perforated by a periodic array of subwavelength holes, constitute another important class of three-dimensional negative-index media. Their multi-layered geometry naturally accommodates LC infiltration within the nanoholes and interlayer cavities, offering an additional degree of design freedom relative to planar SRR arrays.

The negative-index response of a fishnet arises from two spatially overlapping mechanisms. The perforated metal films behave as a diluted plasma, providing negative effective permittivity below the plasma frequency. At the same time, antisymmetric currents excited in the two metal layers form a current loop equivalent to a magnetic dipole, which yields negative effective permeability over a narrowband. Both responses are governed by the dielectric filling the holes and the interlayer gap. Infiltrating this volume with a LC therefore shifts the electric and magnetic resonances simultaneously, tuning the spectral position of the negative-index band itself.

At near-infrared frequencies, Minovich *et al* [138] showed that LC reorientation within a left-handed fishnet shifts its effective refractive index, demonstrating that negative-index behaviour can be dynamically tuned. Zhang *et al* [68] extended this to microwave frequencies: nematic LCs embedded between fishnet layers produced a reversible shift of the left-handed passband under an applied electric field, with the LC molecular reorientation modifying the effective magnetic resonance and thereby the negative-index window. Kruk *et al* [139] further infiltrated fishnet structures with LCs to realize electrically tunable nonlinear optical MMs. Molecular reorientation within the nanoholes altered the local field enhancement and hence the nonlinear susceptibility, producing substantial changes in optical transmission at moderate laser powers, a functionality inaccessible to either the bare fishnet or the bulk LC in isolation.

In the terahertz regime, a multitude of fishnet topologies have been explored to optimize negative-index performance and minimize ohmic losses. As a prominent example highlighting the mechanics of this classification, Zografopoulos and Beccherelli [99] placed a nematic LC cavity between two opposing fishnet slabs, as illustrated in figure 11. Low applied voltages reoriented the LC molecules, shifting the magnetic resonance frequency substantially and yielding faster switching than non-resonant LC-based THz modulators. This resonance-leveraged speed advantage is a recurring theme in LC-MM integration: the sharp spectral feature of the resonator converts small refractive-index changes into large, measurable spectral shifts, relaxing the requirements on LC layer thickness and hence on response time.

Finally, Diepolder *et al* [140] combined p-i-n diodes with LC layers in a reconfigurable transmitarray unit cell operating at 10 GHz. The diodes provide fast, binary 180° phase switching, while the LC layer adds continuous phase trimming within each binary state—a hybrid architecture that overcomes the coarse quantization inherent to diode-only designs. The prototype demonstrated low insertion loss, high efficiency, and good agreement with full-wave simulations, making it suitable for high-gain antenna beamforming applications.

Fishnets remain the only LC-tunable route to a genuinely negative refractive index. Their multilayer geometry provides natural LC reservoirs in the nanoholes and interlayer cavities, allowing the electric and magnetic resonances to be addressed simultaneously [68, 138]. The sharp magnetic resonance also

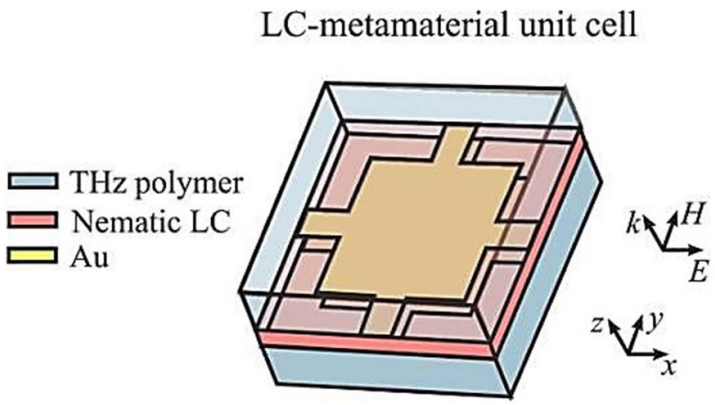



**Figure 11.** The LC-fishnet terahertz metamaterial consists of a metallic fishnet network patterned on a low-loss dielectric substrate. A liquid-crystal cavity is placed between two opposing fishnet slabs, enabling the dynamic tuning of terahertz wave transmission properties. This structure allows for fast switching and precise control, making it suitable for applications in terahertz sensing and communication systems. Reproduced from [99]. CC BY 4.0.

relaxes the LC thickness requirement and hence improves switching speed [99], while infiltration additionally grants access to a tunable nonlinear response [139]. Multilayer nanofabrication is nevertheless slow and costly, uniform infiltration between layers is difficult to verify experimentally, and insertion loss within the negative-index band remains high. The negative-index function itself therefore remains at the laboratory proof-of-concept stage. The hybrid diode–LC transmit-array discussed above [140] is considerably closer to application, but it exploits the fishnet as a phase-shifting host rather than as a negative-index medium. This family is scientifically important for tunable negative-index physics, yet in its present form it is the least likely of the architecture families to reach deployment.

*3.4.5. LC-enhanced FSSs (quasi-2D, metasurface-like)*

FSSs are periodic, planar structures, typically metallic resonators or apertures patterned on a dielectric substrate, that filter electromagnetic waves by selectively transmitting, reflecting, or absorbing energy within defined frequency bands [141–143]. The filtering behaviour arises from the resonant response of the periodic unit cell: at resonance, the structure strongly couples to the incident field and either passes or blocks it depending on whether the element is a patch (band-stop) or an aperture (band-pass) type (figure 12) [144]. Although the specific resonator patterns utilized in literature range from simple dipoles to highly complex fractal or cross-shaped elements, figure 12 provides a general illustrative schematic of an aperture-type FSS to demonstrate the core filtering mechanism. Beyond frequency, FSS performance is sensitive to the angle of incidence and the polarization state of the incoming wave, which must be managed carefully in practical deployments such as radome design, radar cross-section reduction, and antenna sub-reflectors [145, 146].

A conventional FSS has a fixed resonant frequency determined solely by its geometry. Once fabricated, it cannot adapt to changing spectral requirements, a significant limitation in reconfigurable communication systems, cognitive radio, and stealth applications where the operating frequency or threat environment may shift dynamically. Integrating a LC layer into the FSS structure addresses this limitation directly. The LC medium fills the region where the resonant near-field is most concentrated, typically the capacitive gaps between metallic elements, and its bias-dependent permittivity continuously shifts the effective electrical length of the resonator, thereby tuning the resonant frequency without any mechanical or structural change. Compared to a pure LC slab, which provides continuously variable phase delay but no spectral selectivity, the FSS host introduces a sharp, high-Q resonance that translates a modest permittivity change into a precisely controllable shift in the filter passband or stopband centre frequency. This combination is the physical basis for LC-FSS technology as a tunable quasi-2D electromagnetic filter.

The foundational demonstration was reported by Hu *et al* [148], who placed an LC layer between slot-array FSSs operating in the D-band (110–170 GHz). Applying a low bias voltage reoriented the LC molecules, shifting the transmission resonance by approximately 3% and enabling reversible switching between transmission and reflection states. Although the tuning range was modest, this work established that electronic control of FSS resonance through LC permittivity modulation was experimentally viable.

Subsequent efforts extended LC-FSS operation to lower microwave frequencies and more complex polarization environments. Wang and Cai [149] demonstrated a dual-band LC-FSS for Industrial,

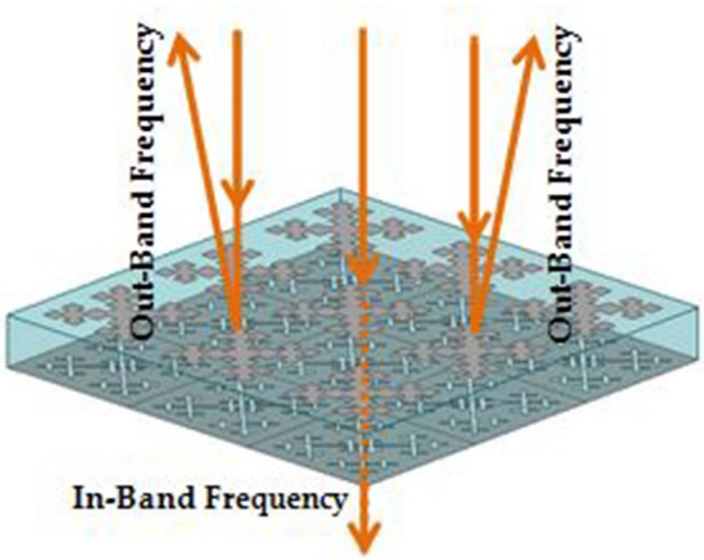



**Figure 12.** Schematic representation of the FSS. The structure transmits in-band frequencies while reflecting out-of-band frequencies. The cross-shaped resonators on the surface govern the transmission and reflection properties based on the incident wave's frequency. Reproduced from [147]. CC BY 4.0.

Scientific, and Medical (ISM) band applications, achieving simultaneous filtering of multiple polarization states across a range of incidence angles—a prerequisite for practical deployment in wideband microwave systems where the illumination geometry is not fixed.

A cluster of significant advances appeared in 2021. Lin *et al* [85] fabricated a Ka-band (26.5–40 GHz) LC-FSS using commercially available LC materials and standard photolithographic processes, achieving 5% frequency tunability, sufficient for channel-switching in millimetre-wave communication front-ends. Li *et al* [150] prioritized spectral selectivity by adopting a three-layer metallization scheme that sharpened the filter roll-off while maintaining low insertion loss across the tuning range; the additional structural degrees of freedom allowed independent control of bandwidth and centre frequency. Lv *et al* [151] pursued miniaturization through vortex-shaped metallic elements, which reduced the unit cell footprint while extending the tuning range to 8.5% and preserving angular stability—an important practical requirement for conformal FSS applications on curved surfaces.

More recently, Yang *et al* [152] addressed the persistent challenge of polarization sensitivity by introducing a double-layer coupled FSS architecture. The coupling between the two layers broadens the effective resonance bandwidth and creates a more isotropic unit cell response, yielding 7.2% continuous frequency tuning across a wide bandwidth with performance that is largely independent of polarization state and incidence angle. This insensitivity to illumination geometry is a critical step toward deploying LC-FSS filters in real-world systems where the direction and polarization of the incident wave are uncontrolled.

Taken together, the trajectory of LC-FSS research reflects a systematic progression in three performance dimensions: tuning range (from 3% to over 8%), spectral selectivity (from simple bandpass to independently controlled centre frequency and bandwidth), and spatial robustness (from normal-incidence-only to wide-angle, polarization-insensitive operation). The primary application drivers are reconfigurable filtering for millimetre-wave and sub-terahertz communications, adaptive radomes for radar systems, and electronically steerable electromagnetic shielding. In each case, the LC-FSS combination delivers a capability, electronically tunable spectral filtering, that neither a fixed-geometry FSS nor an unstructured LC layer can provide independently.

This family is characterized by simple and robust unit cells, low-cost fabrication using commercially available LC mixtures and standard photolithography [85], modest LC volumes, and direct insertion into existing antenna, radome and sub-reflector architectures. The field has also converged on the practically decisive problems, with recent designs delivering angular stability [151] and near-complete polarization and incidence-angle independence [152]. The achievable tuning range nevertheless remains bounded, rising from roughly 3% in the earliest demonstration [148] to 7.2%–8.5% in current designs [151, 152]. This ceiling is set by the trade-off between LC layer thickness, driving voltage and response time, and maintaining the same performance simultaneously across polarization and incidence angle still

requires careful unit-cell engineering. FSS is the most mature family, with LC-based phased-array and reconfigurable-intelligent-surface panels having reached industrial prototyping for satellite and 6 G applications. It therefore represents the most credible near-term commercialization path for LC-MM technology as a whole.

*3.4.6. LC-enhanced chiral and asymmetric structures*

Chirality—the geometric property of a structure that cannot be superimposed on its mirror image—gives rise to a distinctive class of electromagnetic phenomena that neither a conventional metasurface nor a LC medium can fully exploit in isolation. A chiral metasurface interacts differently with left-handed and right-handed circularly polarized (LCP and RCP) light, producing CD and optical activity determined entirely by its fixed geometry. A cholesteric or chiral nematic LC, by contrast, selectively reflects one circular polarization handedness over a photonic bandgap set by its helical pitch, but this response is inherently narrowband and difficult to redirect once the material is assembled. When a chiral or geometrically asymmetric metasurface is integrated with an LC layer, the resonant selectivity of the patterned structure and the bias-tunable birefringence of the LC combine to produce a dynamically reconfigurable chiral optical response—one in which the magnitude, spectral position, and even the sign of the CD can be controlled by an external voltage. This tunability is the defining advantage of LC-integrated chiral architectures over either constituent technology alone.

At the materials level, chirality in LC systems originates from molecular asymmetry and manifests across multiple length scales. Dierking [153] documented how chiral additives or intrinsically asymmetric mesogens drive the self-organization of LCs into helical superstructures, cholesteric phases, Twist Grain Boundary (TGB) phases, and ferroelectric smectic phases, each exhibiting distinct electro-optical responses rooted in their broken mirror symmetry. Notably, biopolymers such as DNA and cellulose nanocrystals adopt lyotropic chiral LC phases due to their inherent molecular handedness, establishing a direct link between biological chirality and photonic functionality. These natural systems provide both design inspiration and fabrication templates for synthetic chiral MMs.

Building on this foundation, Ji *et al* [154] demonstrated a single-layer chiral metasurface capable of selectively absorbing circularly polarized light across multiple spectral bands. The structure exploited different plasmonic resonance conditions for LCP and RCP illumination, yielding absorption efficiency differences of up to 40% between the two spin states. By infiltrating the metasurface with a nematic LC layer, the authors enabled voltage-controlled reconfiguration of both the spin-selective absorption amplitude and the dominant chirality handedness. The absence of a metallic backplate simplified the device architecture and preserved multi-band operation—attributes directly relevant to polarimetric filtering and reconfigurable photonic routing applications.

A complementary approach was demonstrated by Yin *et al* [59], who integrated a birefringent nematic LC into the insulating spacer of a MIM chiral absorber. In its default state, the structure strongly absorbed one circular polarization while reflecting the other, producing a high CD value. When a voltage was applied, LC molecules reoriented from 0° to 90°, reversing the effective optical anisotropy of the spacer layer and flipping the sign of the CD—effectively switching the absorption preference from LCP to RCP without altering the metallic geometry. Simulations confirmed that absorption efficiency remained above 80% and CD values near 70% throughout the switching cycle. This sign-reversal capability, which is inaccessible to a fixed chiral metasurface or a passive LC layer independently, is particularly valuable for biological sensing (where differential CD measurements improve specificity), polarimetric imaging, and chirality-selective optical communication.

At a broader materials level, Wang *et al* [155] reviewed self-organizing chiral LC nanostructures across both thermotropic systems—cholesteric, cubic blue phase, and achiral bent-core LC phases—and lyotropic systems based on DNA, nanocellulose, and graphene oxide. The review identified dynamic photonics, energy harvesting, and optical security as the most mature application areas, while noting that scalable fabrication and long-term stability remain central challenges. Zhang *et al* [156] extended this perspective to LC-templated chiral nanomaterials, systematically addressing the design principles and bottom-up synthesis strategies used to produce chiral plasmonic and chiral luminescent nanostructures. Their framework connects the molecular-scale chirality of the LC template to macroscopic optical activity in the assembled nanomaterial, offering a route to chiral MMs that are self-organized rather than lithographically patterned.

This family provides functionalities that are inaccessible to achiral platforms, including spin-selective absorption with efficiency differences of up to 40% between circular polarizations [154], and voltage-driven reversal of the sign of the CD while maintaining absorption above 80% and CD near 70% [59]. Cholesteric and other chiral LC phases further contribute intrinsic, field-tunable chirality that no lithographic structure alone can supply [153, 155]. Most reported devices are nevertheless isolated single

demonstrations rather than systematically optimized designs, and chiroptical figures of merit (FoM) are not standardized, which makes cross-study comparison unreliable. The coexistence of structural and molecular chirality also substantially complicates modelling and inverse design. This is the youngest of the architecture families, still at an early laboratory stage, with scalable fabrication and long-term stability identified as open problems [155, 156]. It is best regarded as a research frontier with clear long-term relevance to polarization-encoded communication, polarimetric imaging and chiral biosensing, rather than a near-term product route.

As evident from table 7, FSS architectures achieve the best combination of low insertion loss and wide angular stability, while plasmonic and SRR architectures achieve the highest modulation depth at the cost of higher insertion loss. DFLC-based devices offer the fastest response times (1.89 ms) owing to their frequency-driven switching mechanism, whereas electrically tuned SRR systems provide the widest absolute frequency tuning range.

*3.4.7. Critical comparison of architectures*

The preceding sections have examined four principal LC-integrated MM architectures, SRR-based bulk MMs, fishnet structures, FSSs, and chiral/asymmetric metasurfaces. Each offers a distinct combination of electromagnetic functionality, tuning performance, and fabrication complexity that determines its suitability for specific applications.

SRR-based MMs provide the sharpest resonances and hence the highest sensitivity per unit permittivity change, making them well suited to sensing and narrowband filtering. Their primary limitations are polarization sensitivity and the difficulty of scaling periodic three-dimensional arrays to large areas. Fishnet MMs sustain a negative refractive index across a usable bandwidth, but the multilayer metallic geometry introduces significant ohmic loss, particularly at optical frequencies, constraining their use to the microwave and terahertz domains where metal losses are comparatively low. FSSs are inherently planar, scalable, and compatible with conformal substrates, making them the preferred architecture for large-aperture applications such as reconfigurable radomes and adaptive electromagnetic shielding; however, their resonant phase control is limited compared to full metasurface designs. Chiral and asymmetric metasurfaces occupy a distinct functional niche: they are the only architecture capable of circular polarization discrimination and CD sign-reversal under bias, capabilities that are essential for polarimetric sensing and chirality-selective photonics but unnecessary for simple frequency filtering.

In terms of LC integration, the tuning mechanism is the same across all four classes, bias-induced molecular reorientation shifts the effective permittivity in the resonant near-field region, but the sensitivity to LC layer placement, thickness, and alignment varies significantly with architecture. The volumetric coupling in SRR arrays and fishnet structures generally yields larger absolute frequency shifts, while the confined gap fields in FSS and chiral metasurface designs permit thinner LC layers and consequently faster switching. The optimal architecture for any given application must therefore balance resonance sharpness, tuning range, switching speed, insertion loss, and fabrication scalability against the specific electromagnetic functionality required.

Despite these advances, several unresolved technical barriers and conflicting results persist across the literature. Reported tuning ranges for LC-FSS structures vary substantially, from 3% [148] to 7.9% [82], with no consensus on the dominant limiting factor: whether the ceiling is set by LC birefringence, electrode uniformity, or resonator Q-factor degradation under bias remains an open question. Similarly, thermal tuning has been repeatedly proposed for fast switching applications, yet the inherently slow thermal equilibration times (seconds to minutes) make this approach impractical for any communication or signal-processing use case; the few studies pursuing this route have not progressed beyond laboratory demonstration. Reproducibility across laboratories is also a persistent concern: EBL-fabricated LC-MM devices from different groups operating at nominally identical geometries often report resonance frequencies differing by 5%–15%, attributable to variations in LC cell gap, alignment layer quality, and LC infiltration completeness, none of which are consistently reported in the literature. This lack of standardized characterization protocols is a systemic barrier to cross-laboratory comparison and field-wide progress.

*3.4.8. Engineering trade-offs in LC-MM design*

The practical optimization of LC-MM devices requires careful navigation of interdependent performance parameters. Unlike passive MMs where geometry alone determines response, LC-integrated systems involve a coupled set of material, geometric, and electrical variables that cannot be optimized independently. This subsection analyses the three principal trade-off relationships governing device design.

The achievable frequency shift scales approximately linearly with LC layer thickness up to an architecture-dependent optimal value, beyond which field penetration into the LC layer no longer

**Table 7.** Performance benchmark across LC-metamaterial platforms.

| Architecture | Freq. Band | Tuning Range | Mod. Depth | Response Time | Op. Voltage | Insertion Loss | References |
|---|---|---|---|---|---|---|---|
| LC-SRR (electrical) | Ka-band | 26.1–28.5 GHz | >80% | 150 ms | 2.5–10 V | Low | Wang *et al* [83] |
| LC Plasmonic (THz) | THz | 9.35% freq. shift | 96% | <1 s | ∼10 V | Moderate | Yang *et al* [101] |
| LC-FSS (Ka-band) | 26.5–40 GHz | 5% | High | ∼100 ms | <15 V | Low | Lin *et al* [85] |
| LC-FSS (double-layer) | mmWave | 7.2% | High | ∼100 ms | <15 V | Low | Yang *et al* [152] |
| LC-Fishnet (THz) | THz | Resonance shift | >80% | ∼10 ms | ∼10 V | Moderate | Zografopoulos and Beccherelli [99] |
| LC Chiral MIM (optical) | Optical | CD sign reversal | >80%, CD ∼70% | ms | <10 V | Low–moderate | Yin *et al* [59] |
| DFLC Metasurface | Optical | Phase 0–2$\pi$ | >50% | 1.89 ms | 1–40 kHz AC | Low | Kowerdziej *et al* [74] |
| Graphene/LC-Metasurface | THz | 0.75–1.0 THz | ∼80% | ∼50 ms | 10 V | Low | Wang *et al* [65] |

increases the effective permittivity overlap with the resonant near-field. Chiang *et al* [66] demonstrated that for THz SRR MMs, an optimal LC layer thickness of 710 $\mu$m maximizes birefringent interaction, among the largest frequency shifts (up to 21 GHz) reported for electrically tunable THz MMs. Beyond this optimal thickness, additional LC material contributes negligible additional tuning while substantially increasing response time.

LC orientational relaxation time scales as:

$$\tau \propto d^2 \frac{\gamma_1}{K\pi^2} \tag{1}$$

where d is the cell gap, $\gamma_1$ is the rotational viscosity, and $K$ is the relevant Frank elastic constant. This quadratic dependence on cell thickness is the dominant engineering constraint: halving the LC layer thickness reduces response time by a factor of four, but simultaneously reduces the available tuning range proportionally. Wang *et al* [67] demonstrated that an 11.2 $\mu$m-thin LC layer achieves 150 ms response time in a Ka-band SRR system—the optimal trade-off for millimetre-wave communication applications where sub-second reconfiguration is sufficient. For optical applications requiring sub-millisecond response, DFLC mixtures circumvent this constraint by enabling active switching in both directions through frequency modulation rather than relying on elastic relaxation, achieving response times as fast as 1.89 ms [74].

Operating voltage vs cell design and surface treatment. The Fréedericksz threshold voltage is given by:

$$V_{th} = \pi \sqrt{\frac{K}{\varepsilon_0 \Delta\varepsilon}}. \tag{2}$$

Critically, $V_{\text{th}}$ is independent of cell thickness, it depends only on the elastic constant $K$ and the dielectric anisotropy $\Delta\varepsilon$ of the LC mixture. This means that reducing cell thickness to improve response time does not increase the drive voltage requirement, which is a favourable decoupling of these two parameters. However, surface anchoring energy at the LC-electrode interface introduces an effective additional voltage requirement beyond $V_{\text{th}}$.

In summary, no single design point simultaneously optimizes tuning range, response time, and operating voltage. Application-specific prioritization, fast switching for communications, large tuning range for sensing, low voltage for CMOS integration, determines the optimal cell thickness and LC mixture selection for a given LC-MM platform.

*3.4.9. Long-term stability, reliability, and environmental robustness*

Despite the remarkable device-level performance demonstrated across LC-MM platforms, long-term operational stability remains a critical and underexplored aspect of the field. Unlike the LC phase and electromagnetic performance metrics extensively reported in the literature, systematic degradation studies under realistic operating conditions are sparse. The following subsection identifies the principal degradation mechanisms, their physical origins, and practical mitigation strategies.

Mobile ions generated by electrode corrosion, residual impurities in the LC material, or progressive alignment layer decomposition accumulate at the LC-electrode interface under DC or sustained low-frequency AC bias. This ionic accumulation produces image sticking, a progressive increase in threshold voltage ($V_{\text{th}}$), and reduced electro-optic contrast over time. Mitigation strategies include: use of high-purity LC mixtures with ionic impurity levels below 10 ppm; integration of ion-absorbing spacer coatings at the electrode-LC interface; and adoption of AC drive waveforms at frequencies above the ion mobility threshold to suppress directional ion drift.

Polyimide alignment layers, the standard in LCD manufacturing and widely adopted in LC-MM cells, undergo photodegradation under UV illumination and thermal stress above approximately 150 °C, resulting in anchoring energy reduction and pretilt angle drift. These effects directly compromise LC director uniformity and, consequently, device tuning performance. Mitigation: replacement with inorganic alignment layers such as obliquely deposited $SiO_2$ or diamond-like carbon (DLC) films, which exhibit superior thermal and UV stability; alternatively, photoalignment polymers incorporating UV-stable chromophores offer a non-contact solution compatible with nanostructured substrates [61–63].

Nematic LC phases exhibit strong temperature dependence of dielectric anisotropy and birefringence, with both parameters collapsing to zero at the nematic-to-isotropic clearing temperature ($T_{\text{NI}}$). For commonly used mixtures, $T_{\text{NI}} = 60.5$ °C for E7 and $T_{\text{NI}} = 35.3$ °C for 5CB—values that may be approached under high-power illumination or elevated ambient temperatures. Operation near $T_{\text{NI}}$ causes dramatic, uncontrolled permittivity fluctuations that destabilize device performance. Mitigation: selection of high-$T_{\text{NI}}$ LC mixtures such as BL037 ($T_{\text{NI}} > 100$ °C) or GT3-23001 [157]; thermal management

**Table 8.** LC-metamaterial degradation mechanisms and mitigation strategies.

| Mechanism | Cause | Observable effect | Mitigation strategy |
|---|---|---|---|
| Ion contamination | Electrode corrosion; LC impurities | Increased $V_{th}$; image sticking | High-purity LC; AC drive; ion-absorbing coatings |
| Alignment layer aging | UV exposure; thermal stress >150 °C | Pretilt drift; anchoring energy reduction | Inorganic alignment ($SiO_2$, DLC); UV-stable photoalignment polymers |
| Temperature sensitivity | Operation near $T_{NI}$ | Permittivity fluctuations; phase transition | High-$T_{NI}$ LC mixtures; thermal packaging |
| Cyclic fatigue | Repeated switching; flexoelectric buildup | Gradual $V_{th}$ drift; contrast reduction | Optimized waveform; $>10^5$ cycles target |
| Humidity/chemical | Moisture absorption; environmental exposure | Alignment disruption; increased ionic conductivity | Hermetic encapsulation; ALD barrier layers ($Al_2O_3$) |

packaging; and temperature-compensating drive electronics that adjust bias voltage in response to monitored device temperature.

Repeated electrical switching cycles can induce progressive mechanical fatigue in alignment layer surfaces through flexoelectric charge buildup and electrohydrodynamic stress. For standard nematic LC display devices, the literature reports stable operation exceeding $10^5$ switching cycles without significant performance degradation. However, systematic lifetime data for nanostructured LC-MM devices, where alignment is achieved in sub-micron geometries under strong surface anchoring conditions, remain limited. Durability studies in LC-based smart windows have reported stable operation over more than 5000 switching cycles without measurable optical contrast degradation, suggesting the LC layer itself is mechanically robust, with degradation primarily localized to the electrode and alignment subsystems [60].

LC materials can absorb trace atmospheric moisture through imperfect cell sealing, disrupting alignment homogeneity and increasing ionic conductivity, both of which degrade electro-optic performance. Hermetic encapsulation using glass frit bonding or thin-film barrier layers deposited by ALD, notably $Al_2O_3$ at thicknesses of 10–20 nm, provides effective protection against environmental moisture ingress while adding minimal process complexity.

The degradation mechanisms identified above and their corresponding mitigation strategies are consolidated in table 8 below.

### 3.5. Loss mechanisms and mitigation strategies

Despite the remarkable tunability demonstrated across LC-MM platforms, device performance is fundamentally constrained by electromagnetic losses arising from multiple sources. This subsection systematically identifies the primary loss mechanisms and presents targeted mitigation strategies for each.

Metallic resonator structures, most commonly gold (Au) and silver (Ag), contribute significant ohmic losses through resistive dissipation of induced currents, particularly at optical frequencies where the imaginary part of the metal permittivity is large. At THz and microwave frequencies, ohmic losses are comparatively low, making metallic resonators practical. For near-IR and visible applications, replacement with low-loss all-dielectric resonators (Si, $TiO_2$, gap) eliminates metallic absorption entirely while preserving strong electromagnetic resonances through Mie-type modes. Where metallic structures are unavoidable, resonator geometry optimization, minimizing sharp corners and current concentration points, can reduce resistive losses by 20%–30%.

Standard nematic LC mixtures such as E7 and 5CB exhibit non-negligible absorption in the mid-IR range and at select THz frequencies due to molecular vibrational modes. For high-frequency applications, substitution with purpose-engineered low-loss, high-birefringence mixtures, notably LC1825 ($\Delta n \approx 0.38$, low loss) and NJU-LDn-4 ($\Delta n \approx 0.31$) as summarized in table 2, significantly reduces absorption-induced insertion loss while maintaining large tuning range.

Polydomain LC textures arising from poor alignment quality introduce significant scattering losses, particularly in embedded and infiltrated integration geometries where surface-to-volume ratios are high. Photoalignment via polarized UV exposure achieves uniform single-domain alignment even within deep nanocavities, reducing scattering-induced insertion loss by up to 60% compared to conventional mechanical rubbing techniques [61–63]. SAM treatments on metallic surfaces further improve anchoring uniformity at the LC-metal interface [64].

ITO electrodes, while optically transparent in the visible range, contribute parasitic absorption losses of 5%–15% at optical frequencies and significant attenuation at THz frequencies. Mitigation strategies

include: ultra-thin ITO layers (<5 nm) to minimize bulk absorption; substitution with graphene monolayers, which offer >98% THz transparency at ∼400 Ω $sq^{-1}$ sheet resistance [65]; and alternative transparent conductive oxides (AZO, GZO) with optimized carrier density profiles that shift the plasma edge away from the operating frequency.

In metal-LC hybrid systems, near-field energy localized within plasmonic hotspots is partially dissipated through non-radiative decay channels in the metallic structure. This intrinsic loss mechanism limits the quality factor (Q-factor) of plasmonic resonances. Mitigation approaches include: adoption of Fano resonance configurations, where destructive interference between a broad plasmonic mode and a narrow resonance produces a sharp spectral feature with reduced radiative damping; EIT analogue designs that achieve narrow transmission windows with inherently lower loss; and replacement of plasmonic resonators with dielectric Mie resonators supporting high-Q bound states in the continuum (BIC).

#### *3.5.1. LCs vs competing tunable material platforms*

A critical assessment of LC-based tunable MMs requires systematic comparison with the principal competing material platforms. Table 9 consolidates the key performance metrics of seven tunable material technologies across eight comparative dimensions relevant to electromagnetic MM applications.

LCs offer a uniquely advantageous combination of very low power consumption (capacitive operation requiring no sustaining current), continuous analogue tunability, broad spectral coverage from microwave to visible frequencies, and full CMOS compatibility—advantages that no competing material simultaneously matches. The principal disadvantage relative to phase-change materials is switching speed: LC response times in the millisecond range are several orders of magnitude slower than the subpicosecond switching achievable with $VO_2$ or GST under optical excitation. However, for the majority of targeted LC-MM applications, reconfigurable antennas, adaptive radomes, beam-steering reflect arrays, and tunable filters, millisecond-scale reconfiguration is entirely sufficient, making the speed disadvantage practically irrelevant.

Graphene offers ultrafast switching (ps–ns) and gate-voltage tunability compatible with CMOS processes, but its modulation depth in MM systems is limited by the relatively small change in sheet conductance achievable within the linear response regime, and its fabrication at wafer scale with consistent quality remains challenging. Vanadium dioxide ($VO_2$) provides a dramatic metal-to-insulator transition at 68 °C with large optical contrast, but requires sustained thermal input to maintain the metallic state, making it inherently volatile and energy-inefficient for static configurations. GST phase-change materials offer non-volatile multi-level storage states and large optical contrast, but switching requires high-energy optical or electrical pulses and the transition is not fully continuous. MEMS achieve large tuning through geometric reconfiguration but introduce mechanical complexity, fragility under vibration, and are practically limited to microwave and lower THz frequencies. Ferroelectric materials (BTO, PZT) require high drive voltages and exhibit hysteresis that complicates analogue control. Transparent conducting oxides provide CMOS-compatible gate tunability but with narrow modulation range at optical frequencies.

LCs offer uniquely low power consumption (capacitive operation), broad spectral coverage (microwave to visible), and CMOS compatibility—advantages no competing material fully matches. The principal disadvantage relative to phase-change materials ($VO_2$, GST) is slower switching speed (ms vs ps) and temperature sensitivity. Graphene offers faster switching but with limited modulation depth. MEMS achieve large tuning via geometry change but at the cost of mechanical complexity. For most communication and sensing applications where continuous, low-voltage tuning is prioritized, LCs remain the most practical and mature technology.

#### *3.5.2. Standardized FoM for LC-MM devices*

A persistent barrier to meaningful cross-platform comparison in the LC-MM literature is the absence of standardized FoMs. Individual studies report performance metrics using inconsistent definitions—some normalize tuning range to centre frequency, others report absolute shifts; insertion loss is variously reported in dB or as a percentage; response time is sometimes the rise time, sometimes the full switching cycle. This inconsistency makes it impossible to objectively rank competing designs or identify which architecture best suits a given application. To address this, we propose the following frequency-regime-specific FoMs, adapted from analogous metrics in the photonic sensing and microwave engineering literature:

**Table 9.** Liquid crystals vs competing tunable materials for electromagnetic metamaterials.

| Material | Tuning mechanism | Response time | Tuning range | Power consumption | CMOS compatible | Key limitation | Freq. Range |
|---|---|---|---|---|---|---|---|
| Liquid Crystal (LC) | Electric/thermal/optical/magnetic | 1.89 ms—seconds | 3–21 GHz; 5%–10% (THz) | Very low (capacitive) | Yes | Slow vs PCM; temperature sensitive | Microwave–Optical |
| Graphene | Gate voltage (Fermi level) | ps–ns | Moderate ($<$10%) | Low | Yes | Small modulation depth; fabrication complexity | THz–IR |
| $VO_2$ (PCM) | Thermal/optical/electrical | Sub-ps (optical) | Large (metal–insulator) | High (heating required) | Partial | High transition temp. (68 °C); volatile state | THz–Optical |
| GST (PCM) | Optical/electrical pulse | ns–$\mu$s | Very large (amorphous–crystal) | Moderate | Partial | Non-continuous tuning; high write energy | NIR–Optical |
| MEMS | Electrostatic/thermal actuation | $\mu$s–ms | Large (geometry change) | Low | Partial | Fragile; complex fabrication; limited to microwave/THz | Microwave–THz |
| Ferroelectrics (BTO, PZT) | Electric field (piezo) | ns–$\mu$s | Moderate (1%–5%) | Low | Partial | High voltage required; hysteresis | Microwave–THz |
| TCO (ITO, AZO) | Gate voltage (carrier density) | ns | Small–moderate | Low | Yes | Narrow tuning range; high loss at optical freq. | NIR–Optical |

**Table 10.** Standardized FoM comparison across representative LC-metamaterial platforms.

| Architecture | $FoM_{MW}$ (% per $V_{rms}$) | $FoM_{THz}$ (MD/IL) | $FoM_{speed}$ (% per ms) | Notes |
|---|---|---|---|---|
| LC-SRR Ka-band | 0.28 | — | 0.53 | Wang *et al* [67] |
| LC Plasmonic THz | — | ∼32 | ∼96 | Yang *et al* [101] |
| LC-FSS Ka-band | 0.33 | — | — | Lin *et al* [85] |
| LC-FSS double-layer | 0.48 | — | — | Yang *et al* [152] |
| LC-Fishnet THz | — | >8 | ∼8 | Zografopoulos and Beccherelli [99] |
| LC Chiral MIM | — | — | ∼80 | Yin *et al* [59] |
| DFLC Metasurface | — | — | >26 | Kowerdziej *et al* [74] |
| Graphene/LC THz | — | ∼8 | ∼1.6 | Wang *et al* [65] |

Microwave and mmWave regime:

$$FoM_{MW} = \frac{\left(\frac{\Delta f}{f_0}\right)}{V_{drive}} \left[\% \text{ per } V_{rms}\right]. \tag{3}$$

This metric normalizes the relative frequency tuning range by the required drive voltage, rewarding designs that achieve large spectral reconfiguration at low operating voltages—a critical requirement for CMOS-compatible 5 G/6 G beam-steering applications.

Terahertz regime:

$$FoM_{THz} = \frac{Modulation\ Depth\ (\%)}{Insertion\ Loss\ (dB)}. \tag{4}$$

This ratio balances modulation performance against the penalty imposed by device losses, directly reflecting the signal quality achievable in a THz communication or sensing link. A device with 90% modulation depth but 10 dB insertion loss is less useful than one achieving 80% modulation at 1 dB loss.

Optical regime:

$$FoM_{Opt} = \frac{\left|\Delta n_{eff}\right|}{\alpha_{loss}} \left[RIU\ cm\right]. \tag{5}$$

This metric, effective refractive index change normalized by the absorption coefficient, is analogous to the sensitivity-to-loss ratio widely used in optical biosensor benchmarking, and directly captures the trade-off between tuning magnitude and optical transparency.

Switching-speed-critical applications (all regimes):

$$FoM_{speed} = \frac{Modulation\ Depth\ (\%)}{Response\ Time\ (ms)}. \tag{6}$$

This figure of merit rewards designs that achieve high modulation at fast switching speeds, directly relevant for adaptive optics, high-speed communications, and real-time beam steering.

Application of these FoMs to the eight representative LC-MM platforms provided in table 10 below.

### 3.6. Simulation studies used in LC-enhanced MMs research

Simulation studies of LC-enhanced MMs inherently involve a multiscale and multiphysics problem, where electromagnetic wave propagation is strongly coupled with the field-induced reorientation of anisotropic LC molecules. Unlike conventional passive MMs, the tunability of these systems arises from the dynamic redistribution of the LC director field, which directly modifies the local permittivity tensor. Consequently, numerical modelling is not merely supportive but constitutes the backbone of design, optimization, and physical interpretation in this field.

Early simulation approaches often relied on simplified isotropic approximations, where the LC medium was treated as a homogeneous dielectric with an effective scalar permittivity [158]. Although computationally efficient, this approximation has been shown to produce fundamentally incorrect predictions in resonant MM systems. In particular, isotropic models fail to capture localized near-field

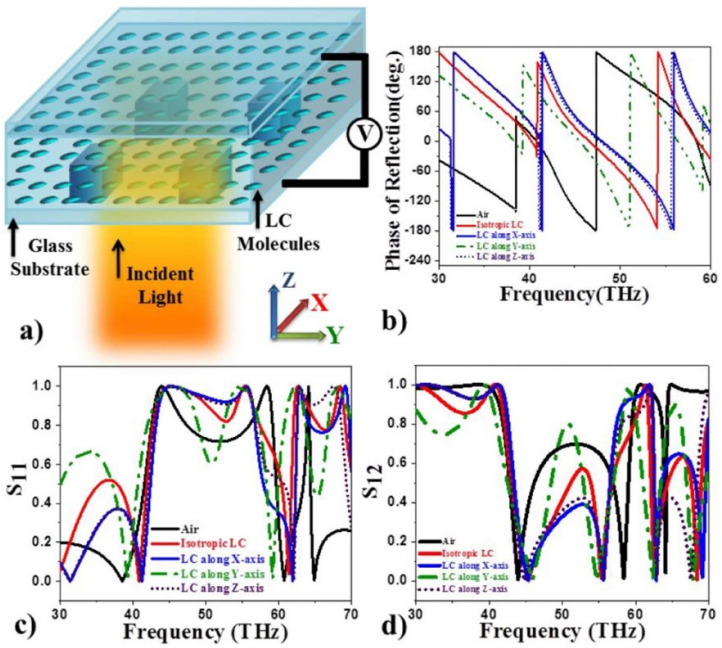



**Figure 13.** Electromagnetic response of a Te metasurface embedded in a liquid crystal (LC) environment. (a) Schematic illustration of the unit cell, featuring cubic Te structures (1 $\mu$m × 1 $\mu$m × 1 $\mu$m) with a 2 $\mu$m lattice constant inside a nematic LC medium. (b) Phase of the reflected light as a function of incident frequency. (c) and (d) Simulated scattering parameters ($S_{11}$ and $S_{12}$) across the 30–70 THz range, respectively. The plots clearly demonstrate the stark contrast in resonance behaviour between the simplified isotropic LC assumption (red curves) and the more rigorous anisotropic models where the LC director is aligned along the *X*, *Y*, and *Z* axes (blue, green, and purple curves). Reproduced from [159]. CC BY 4.0.

interactions and polarization-dependent responses within subwavelength structures, leading to non-physical results such as incorrect resonance shifts. As illustrated in figure 13, assuming an isotropic LC medium (red curves) yields significantly different reflection phases and scattering parameters ($S_{11}$, $S_{12}$) in the 30–70 THz range, specifically failing to capture the ∼4 THz bandwidth shifts and the precise depth of the reflection nulls compared to rigorous anisotropic models where the LC is aligned along specific axes. These discrepancies arise because the scattered electromagnetic fields within MMs are highly non-uniform and not aligned with the incident field polarization, making scalar representations insufficient.

To address these limitations, modern simulation frameworks adopt a rigorous anisotropic formulation, where the LC is described by a spatially varying permittivity tensor. This tensorial representation is directly linked to the LC director orientation and evolves under external stimuli such as electric or magnetic fields. Accurate determination of this director field requires solving energy minimization problems based on continuum theories, most commonly the Frank–Oseen elastic model or the more comprehensive LdG formalism [160]. These approaches account for elastic deformations (splay, twist, bend), surface anchoring conditions, and electrostatic coupling, enabling realistic modelling of LC behaviour within complex MM geometries.

The simulation workflow therefore typically begins with the calculation of the equilibrium (or transient) LC director distribution. This step is often performed using finite element-based multiphysics solvers such as COMSOL Multiphysics, where electrostatic and elastic equations are solved simultaneously. The resulting spatial director profile is then translated into a full anisotropic permittivity tensor field, which serves as the input for electromagnetic simulations. Importantly, the accuracy of this step is critical, as even small deviations in director orientation can significantly impact resonance behaviour and tunability.

Once the local dielectric environment is mapped out, full-wave techniques such as the finite-difference time-domain (FDTD) and the finite element method (FEM) are brought in to analyse the actual electromagnetic wave interactions. FDTD and its integral-based counterpart, the finite integration technique (FIT), are highly versatile for discretizing Maxwell's equations in both space and time, making them highly effective for observing the temporal evolution of fields and extracting wideband

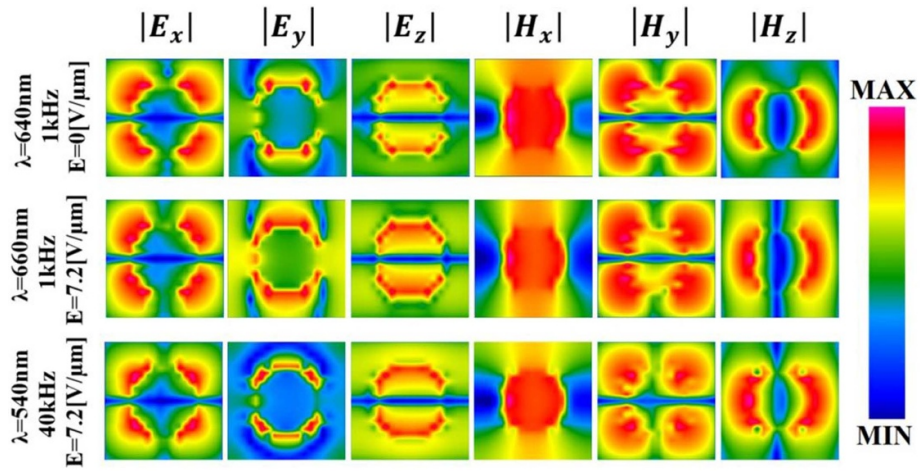



**Figure 14.** Spatial distribution of electric (E) and magnetic (H) fields within an active metadevice at different resonant frequencies (640 nm, 660 nm, and 540 nm). These simulated cross-sectional profiles demonstrate how dual-frequency liquid crystal reorientation governs the localized plasmonic modes. Reproduced from [74]. CC BY 4.0.

spectral responses. A classic example is the work by Kowerdziej *et al* [161], who utilized FDTD simulations in QuickWave to analyse a left-handed MM in the 10–14 GHz range. Their findings clearly demonstrated that the device's tunability is directly tied to the LC's dielectric anisotropy, confirming that precise molecular control translates to a predictable resonance shift. Beyond simply predicting frequency shifts, modern simulations delve into the underlying physical mechanisms by mapping electric and magnetic field distributions (figure 14). Wang *et al* [162], for example, provided a thorough analysis of a terahertz modulator by monitoring electric field distributions at resonance. As illustrated in their studies, it is the transition between localized dipole modes and non-local surface-Bloch modes—driven entirely by LC reorientation—that enables a modulation depth exceeding 90% and an insertion loss below 0.5 dB.

Beyond predicting frequency shifts, full-wave simulations such as CST Microwave Studio are vital for visualizing near-field interactions. For instance, simulations of a graphene-assisted asymmetric cross-shaped absorber revealed that the reorientation of the LC director under a 10 V bias does not merely shift the resonance frequency, but radically redistributes the near-field hot spots. The intense THz electric field enhancement physically migrates from one arm of the cross-resonator to the other as the LC transitions from a horizontal to a vertical alignment [65]. Such predictive near-field mapping is crucial for designing advanced sensors and nonlinear metadevices.

Vasić *et al* [163] leveraged FEM in COMSOL Multiphysics to simulate a unit cell of an LC-based MM under periodic boundary conditions. FEM-based platforms like Ansys HFSS and CST Studio Suite are often the standard for frequency-domain analysis, especially for complex volumetric geometries. Guirado *et al* [157] introduced an insightful dynamic modelling approach for multiresonant planar cells. They used FEM to solve the LC director equation in the longitudinal direction and integrated this physics directly into CST Studio Suite. Their hybrid strategy showed that using a reduced number of stratified layers can accurately model material inhomogeneity without sacrificing computational efficiency. At terahertz (THz) and optical frequencies, simulations have focused on optimizing absorber performance and dynamic control. For example, Ansys HFSS simulations demonstrated that leveraging the temperature-sensitive refractive index of nematic LCs can achieve tunability in the range of 30 nm [80]. More recently, Wang *et al* [83] utilized Ansys HFSS to investigate the impact of LC molecular reorientation, demonstrating a tunability of 10.7% at 30.4 GHz.

In periodic optical and photonic structures, Rigorous Coupled-Wave Analysis (RCWA) provides an efficient alternative, especially for grating-like geometries [164]. This method leverages Fourier expansions and Floquet theory to solve Maxwell's equations exactly for periodic media. For large-scale planar systems, more efficient methods such as the Spectral Domain Method of Moments (SD-MoM) are preferred, as they significantly reduce computational complexity by solving integral equations only on conductive surfaces rather than across the entire volume [165]. Additionally, analytical approaches such as the Tight-Binding Method (TBM) have been introduced to estimate inter-cell coupling effects without requiring full-wave simulations of large arrays.

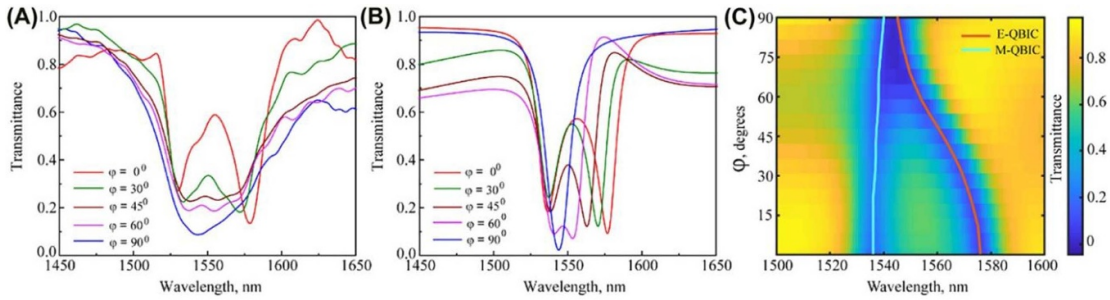



**Figure 15.** Continuous spectral tuning of the metasurface via magnetic field reorientation. (A) Measured and (B) numerically calculated transmittance spectra for the sample with a periodicity of $P_{y1} = 730$ nm, illustrating the effect of varying the in-plane magnetic field angle ($\varphi = 0°$, 30°, 45°, 60°, and 90°). (C) A simulated colourmap of the transmittance as a continuous function of the magnetic field orientation $\varphi$. The superimposed cyan and orange lines track the gradual spectral shifts of the M-QBIC and E-QBIC resonance modes, respectively, highlighting the excellent agreement between the predicted continuous tunability and the discrete experimental measurements. Reproduced from [167]. CC BY 4.0.

A critical aspect of LC MM simulation is the integration of different computational tools. Since electromagnetic solvers typically do not natively include LC physics, hybrid workflows are commonly employed. In such approaches, LC orientation data are first computed using dedicated LC simulation software and then exported (e.g. as CSV datasets) to electromagnetic solvers. This data must be carefully interpolated onto the electromagnetic mesh to ensure consistency between mechanical and electromagnetic domains. Improper mapping can lead to significant errors in predicted optical or microwave responses [166].

Beyond steady-state analysis, recent studies have increasingly focused on transient and dynamic simulations to capture switching behaviour and response times. Furthermore, these numerical models are highly effective at capturing continuous dynamic responses rather than just discrete states. These models incorporate hydrodynamic effects, rotational viscosity, and time-dependent field interactions, enabling the prediction of millisecond-scale LC dynamics. Furthermore, these advanced numerical frameworks are highly effective at capturing continuous parametric variations. As illustrated in figure 15, systematically varying the external magnetic field orientation ($\varphi$) allows for the continuous tuning of specific resonance modes, yielding a precisely tracked wavelength shift of approximately 40 nm. The excellent agreement between the measured intermediate states (figure 15(A)) and the calculated continuous spectral mapping (figure 15(C)) confirms that the complex reorientation dynamics of the LC director field can be reliably predicted. More recently, data-driven approaches have begun to complement traditional numerical methods. Machine learning (ML)-based surrogate models can approximate electromagnetic responses with significantly reduced computational cost, and physics-informed neural networks (PINNs) have been introduced to embed Maxwell's equations directly into the learning process, ensuring physically consistent predictions while accelerating inverse design tasks.

Ultimately, the true test of these predictive models lies in their experimental validation [168]. As demonstrated in figure 16, the simulated transmittance spectra and local field profiles (Panels (C), (D)) align remarkably well with the experimental measurements (Panels (A), (B)) under varying magnetic field orientations.

Kowerdziej *et al* [74] demonstrated this beautifully with dual-frequency liquid crystal (DFLC) hybrids. Their simulated transmission spectra ($T_s$) aligned remarkably well with the experimental measurements ($T_M$) as depicted in figure 17. This agreement not only validated the bidirectional spectral tuning—showing a redshift at 1 kHz and a blueshift at 40 kHz—but also confirmed that these computational models can be trusted to design devices that bypass the slow relaxation times typical of single-frequency LC systems. While strong agreement is often achieved, discrepancies can occasionally arise due to fabrication imperfections, finite-size effects, and deviations from ideal boundary conditions. These challenges highlight the ongoing need for improved multiscale modelling strategies that bridge molecular-level LC behaviour with macroscopic electromagnetic responses.

Collectively, these diverse simulation methodologies have significantly advanced our understanding of LC-MM interactions. The performance metrics of various LC-based MMs discussed in these simulation studies are summarized in table 11.

### 3.7. Wide-ranging applications of LC-based MMs

The integration of LCs with MM and metasurface architectures has enabled a paradigm shift from static electromagnetic components to dynamically reconfigurable and programmable photonic systems. Unlike

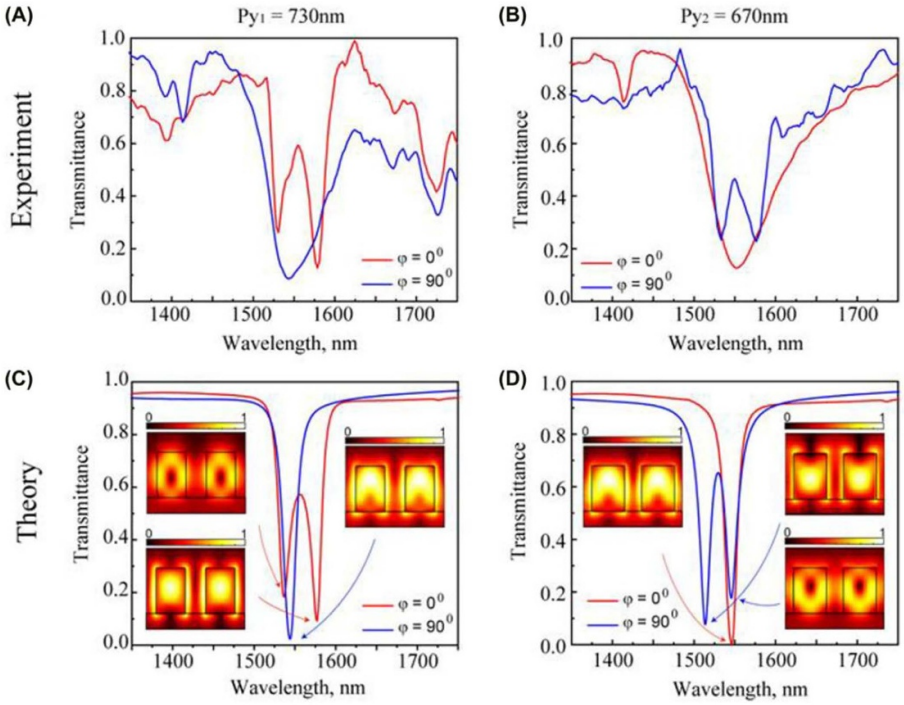



**Figure 16.** Measured (A), (B) and numerically calculated (C), (D) normalized transmittance spectra for two metasurface samples with periodicities $Py_1 = 730$ nm (A), (C) and $Py_2 = 670$ nm (B), (D) after nematic liquid crystal (NLC) infiltration. The red curves illustrate the resonance positions when the applied magnetic field, B, is aligned along the $x$-axis ($\varphi = 0°$), whereas the blue curves correspond to alignment along the $y$-axis ($\varphi = 90°$). The insets in panels (C) and (D) depict the simulated electric field amplitude profiles of the QBIC resonances, highlighting the capability of these numerical models to map local field distributions accurately. Reproduced from [167]. CC BY 4.0.

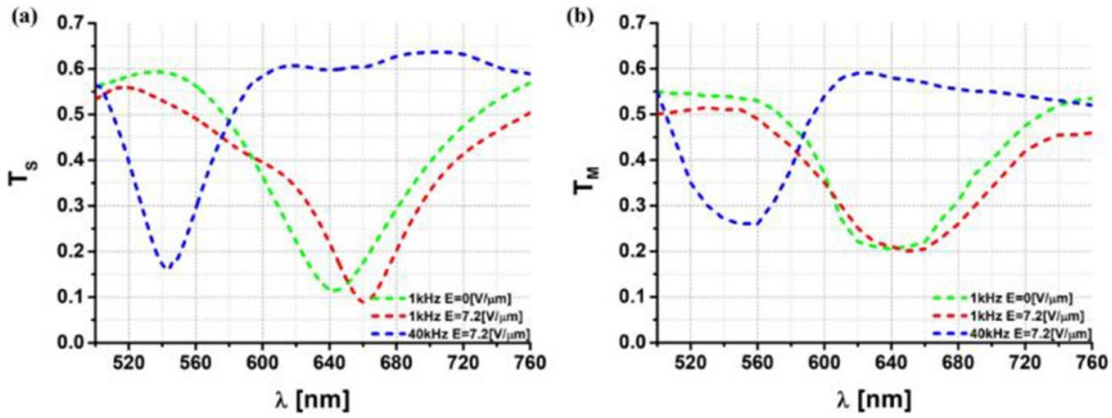



**Figure 17.** Transmission spectra demonstrating bidirectional spectral tuning in a dual-frequency liquid crystal (DFLC)-integrated plasmonic metamaterial. (a) Simulated transmission spectra ($T_s$) showing a redshift at a low driving frequency (1 kHz) and a blueshift at a high driving frequency (40 kHz). (b) Experimental measurements ($T_M$) confirming the frequency-dependent spectral shifts. This bidirectional tunability leverages the DFLC's frequency-dependent dielectric anisotropy, enabling active optical switching and eliminating the slow relaxation times associated with conventional single-frequency LC devices. Reproduced from [74]. CC BY 4.0.

conventional MMs, whose functionality is fixed after fabrication, LC-based MMs leverage the electrically controllable birefringence of LCs to achieve continuous and low-power tunability across a wide spectral range. This capability has led to a broad spectrum of applications, which can be systematically categorized into three major domains: SLM, optical and spectral filtering, and display/colour technologies.

One of the most transformative application areas is SLM and active polarization control. Traditional LCoS systems are widely used for beam shaping, holography, and adaptive optics; however, they suffer from intrinsic limitations such as large LC layer thickness and pixel crosstalk due to fringing fields. LC-integrated metasurfaces overcome these constraints by decoupling phase modulation from physical

**Table 11.** Comparative summary of material properties, frequency tunability, simulation methods, and performance metrics of liquid crystal-based electromagnetic structures.

| References | Software | Structure/materials[a] | LC properties[a] | Frequency range & tuning | Performance metrics |
|---|---|---|---|---|---|
| Kowerdziej *et al* [161] | QuickWave | Teflon fibreglass, metals, LC | LC orientation: 0° to 90° loss tangents: $\tan\delta_o = 0.025$ $\tan\delta_e = 0.001$ | 10–14 GHz, Resonance shift 11.35 GHz | Resonance frequency tuning via LC reorientation |
| Wang *et al* [162] | COMSOL Multiphysics | Poly(3,4-ethylenedioxythiophene), polyimide, LCMS-107 | $n_o = 1.55 + i0.03$, $n_e = 1.83 + i0.001$ quality factor = 68 at 1.75 THz | 60 GHz tuning for Incident angle: 0°–15°, 140 GHz for Incident angle: 5°–25° | Modulation depth >90%, insertion loss < 0.5 dB |
| Shih *et al* [120] | FDTD Simulation Software | SRR, PET Substrate, Dye Layer (SD1) | Nematic LC, change in refractive index based on LC alignment | 0.551 THz to 0.566 THz, tunable by LC director alignment. | Losses above 0.6 THz, Experimental peak at 0.688 THz aligns. |
| Guirado *et al* [157] | COMSOL Multiphysics and CST Studio | Quartz, GT3-23001 LC (LC between two electrodes) | Height of LC:0.075 mm | Frequency tuning range: 100 GHz, Losses: 6 dB | 360° phase control, low-loss operation |
| Mirbagheri and Crouse [80] | Ansys HFSS | Silicon wafer, $SiO_2$, Silicon Nanodisk, 5CB LC, glass wafer | $n_e = 1.69$, $n_o = 1.53$ at 24 °C, $n = 1.58$ at 39 °C | Wavelength Tuning range: 30 nm | Temperature-driven refractive index tuning |
| Wang *et al* [83] | Ansys HFSS | Metallic electrodes, fused silica, NLC | $\varepsilon r_{\parallel} = 3.16$, $\varepsilon r_{\perp} = 2.47$, $\tan\delta_{\parallel} = 0.0033$, $\tan\delta_{\perp} = 0.0151$ for 30 GHz | Resonance Shift: 30.4 GHz→27.3 GHz (10.7% tunability) | Phase change 60°, power contrast: 10 dB, $S_{21} = -2.5$ dB |
| Mamonova *et al* [169] | COMSOL Multiphysics | ITO, polyimide, LC (E7), chromium stearyl surfactant | Director distribution, response to electric fields, reorientation dynamics | Visible light spectrum (450 nm–700 nm), tunable by electric fields, fast switching times (ms range) | Diffraction efficiency transmittance, optical switching speed, alignment quality |
| Han *et al* [170] | CST Microwave Studio | Metal-LC-Metal | Electrically tunable permittivity, Low dielectric loss, Anisotropic | X-band (9.5–10.5 GHz), Tuning achieved by applied electric field, Reflection angle tuning: 20° and 30° | Achieves dynamic phase shift up to $2\pi$ |

[a] $SiO_2$: Silicon Dioxide, $n_o$: LC's ordinary refractive index, $n_e$: LC's extraordinary refractive index, $\varepsilon r_{\parallel}$: Relative dielectric constant when the electric field is parallel to the liquid crystal and $\varepsilon r_{\perp}$: Relative dielectric constant when the electric field is perpendicular to the liquid crystal.

propagation distance. By electrically controlling the molecular orientation of LCs, researchers have developed highly efficient reconfigurable antennas [83], and polarization converters [73, 163]. These functionalities are particularly valuable in high-frequency applications, such as THz spatial light modulators [75, 171], where active control over wave interactions enhances optical performance. As a representative architecture, figure 18 details the design and working principle of a dual-colour THz SLM, illustrating how LC-permittivity tuning enables precise reflectance control. The dynamic modulation of polarization

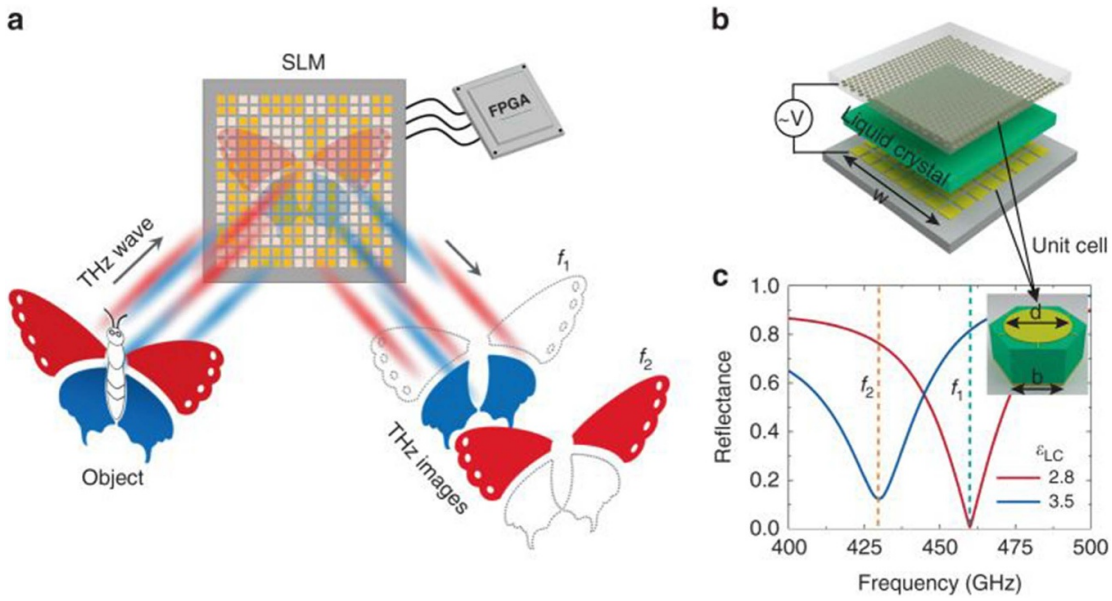



**Figure 18.** (a) Schematic diagram of the dual-colour THz SLM. (b) Exploded view of the THz SLM; the resonant structures are on the back of the top quartz substrate (300 $\mu$m), and the pixelated gold patches are on the front of the bottom quartz substrate (500 $\mu$m). The LC layer thickness is 10 $\mu$m, and the side length ($w$) is 19.7 mm. (c) Simulated reflectance spectra of the SLM for different permittivities of LC ($\varepsilon_{LC}$). The inset displays the unit cell of the MMA with $d = 240$ $\mu$m and b = 173 $\mu$m. Reproduced from [172]. CC BY 4.0.

states—ranging from linear to circular polarization—demonstrates the versatility of LC-based MMs in controlling electromagnetic behaviour with minimal energy input, critical for emerging technologies such as LiDAR, free-space optical communication, and programmable optical computing.

Another major application domain lies in optical and spectral filtering, where LC-based MMs function as tunable FSS, perfect absorbers [59, 173], and compact spectroscopic elements. In microwave and terahertz regimes, LC infiltration into periodic metallic structures allows dynamic tuning of resonance frequencies through voltage-controlled permittivity changes. The introduction of compact, polarization-insensitive bandpass filters showcases the potential for high-performance signal processing. For instance, Lv *et al* [82] proposed a polarization-insensitive LC-based MM filter featuring a flat-top passband and sharp roll-off, demonstrating a 7.9% continuous tuning capability within the 10.88 GHz to 11.78 GHz range. Moreover, LC-integrated MM absorbers can dynamically switch between high-absorption and reflective states, making them highly suitable for applications such as thermal camouflage and hyperspectral sensing. In the visible and near-infrared ranges, architectures like dichroic metagrating cavities have demonstrated wide tuning ranges, paving the way for on-chip spectrometers.

In the visible and near-infrared ranges, more advanced architectures—such as dichroic metagrating Fabry–Perot cavities—have demonstrated wide tuning ranges (hundreds of nanometres) with relatively high transmission efficiencies. These systems utilize LC layers as electrically controlled polarization modulators, enabling 'mode switching' between distinct spectral resonances. Such capabilities pave the way for compact, high-resolution, and energy-efficient hyperspectral imaging systems and on-chip spectrometers.

A rapidly advancing and highly impactful application field is displayed technologies and ultrafast photonics. Conventional display systems rely on bulky optical components and polarization filtering, which limit efficiency. LC-based metasurfaces address these challenges through structural colouration, where colour generation is achieved via nanoscale optical resonances. Another groundbreaking application involves the development of voltage-controlled metasurfaces capable of displaying vivid red, green, and blue pixels. These systems utilize LCs to achieve dynamic subwavelength pixel control, enabling ultrahigh-resolution colour printing, multicoloured cryptography, and full-colour reflective displays [174]. Furthermore, by reducing LC layer thickness and optimizing the resonant near-field, researchers have significantly improved response times, achieving modulation speeds up to 50 times faster than conventional LCD designs [175]. Additionally, the ability to fine-tune light transmission enhances the functionality of smart windows, offering energy-efficient solutions for next-generation architectural and automotive applications.

Additionally, voltage-controlled LC metasurfaces enable dynamic colour tuning and pixel-level modulation, supporting applications such as high-resolution reflective displays, optical encryption, and adaptive camouflage. The ability to generate vivid and tunable RGB responses at subwavelength scales highlights the strong potential of LC-based MMs in next-generation AR, VR, and holographic display systems.

Beyond these primary domains, LC-based MMs are increasingly explored in sensing technologies, where their birefringence properties enable highly sensitive detection mechanisms. By embedding LCs within nanoporous structures or integrating them with resonant metasurfaces, researchers have engineered bio-photonic sensors and thermal detectors capable of real-time monitoring. For instance, Rahimi and Motahari [176] developed a novel sensor utilizing E7 Nematic LC, achieving a remarkable refractive index tolerance of 500 nm $RIU^{-1}$ and a thermal sensitivity of 11 nm $K^{-1}$. Additionally, the combination of zero electrical permeability MMs with high-birefringence LC films has enabled tunable photonic devices with enhanced detection sensitivity [177]. These robust systems leverage the environment-dependent refractive index of LCs, making them highly promising candidates for label-free biomedical diagnostics, environmental sensing, and integrated photonic circuits.

In summary, LC-based MMs provide a versatile and scalable platform for dynamic electromagnetic wave manipulation. Their ability to combine subwavelength optical control with continuous, low-power tunability has unlocked applications ranging from beam steering and adaptive filtering to structural colour displays and intelligent sensing systems. As fabrication techniques and material engineering continue to advance, these hybrid systems are expected to play a central role in the development of next-generation, compact, and multifunctional photonic technologies.

### 3.8. Opportunities and challenges

LC materials provide a unique opportunity for the development of tunable metasurfaces, enabling dynamic control of electromagnetic properties in real-time. Their ability to manipulate light with high precision opens new avenues for adaptive optical devices [35]. They can adjust key electromagnetic properties such as refractive index, resonance frequency, and polarization in real time. This adjustment is achieved by applying external stimuli including electric fields, magnetic fields, temperature variations, or light. As a result, these materials operate without the need for any mechanical reconfiguration. They cover a wide frequency range, from microwaves and terahertz to visible and infrared wavelengths. This versatility makes them suitable for various applications in communication, sensing, and imaging.

LC-enhanced MMs also have fast response times, particularly in the terahertz and optical ranges. Thin LC layers allow for rapid reconfiguration, with response times measured in milliseconds (as demonstrated in figure 19), which is essential for adaptive optics and high-speed communication systems. Furthermore, these systems consume low power because they operate using low-voltage inputs. Their compatibility with plasmonic materials, metasurfaces, and nanophotonic circuits supports the development of compact and multifunctional devices that can be produced using standard fabrication techniques.

Despite these advantages, LC-enhanced MMs face several challenges. The degradation mechanisms underlying long-term stability concerns, including ion contamination, alignment layer aging, temperature sensitivity, cyclic fatigue, and environmental exposure, are analysed in detail in section 3.4.9, along with targeted mitigation strategies for each. Additional challenges include the following:

Fabrication complexity is a significant concern. Integrating LCs with nanostructured MMs requires precise alignment and encapsulation, increasing both production cost and complexity. Achieving uniform LC alignment over large areas remains a difficult technical problem. Although these systems use low power during tuning, continuous operation in devices like displays or sensors may lead to concerns about cumulative energy consumption.

In summary, LC-enhanced MMs offer promising dynamic control for next-generation electromagnetic devices. They have strong potential for applications in communication, sensing, and imaging. However, challenges related to lower-frequency response speed, environmental sensitivity, fabrication complexity, material limitations, and long-term stability need to be addressed. Future research into improved LC materials, advanced fabrication techniques, and innovative hybrid integration methods is essential to overcome these obstacles and fully exploit the potential of LC-enhanced MMs.

The key advantages, challenges, research directions, future prospects, and potential applications of LC-enhanced MMs are summarized in table 12.

### 3.9. Looking to the future: the potential of LC-enhanced MMs

The integration of LCs with MMs has opened a new frontier in dynamic and adaptive electromagnetic devices. As research advances, the potential applications of LC-enhanced MMs are expanding into areas

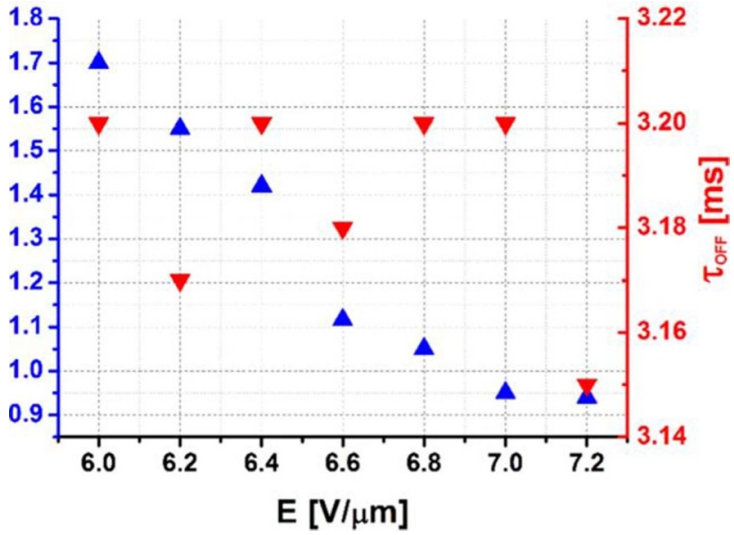



**Figure 19.** Experimental response times of a metadevice using a dual-frequency switching mechanism. By utilizing frequency-dependent dielectric anisotropy, both switch-on and switch-off times can be driven actively, achieving millisecond response times and overcoming the natural relaxation delay of conventional nematic liquid crystals. Reproduced from [74]. CC BY 4.0.

previously considered technologically infeasible. These materials combine the dynamic properties of LCs with the extraordinary electromagnetic capabilities of MMs, enabling real-time control over light and other electromagnetic waves. Below, we explore the transformative potential of LC-enhanced MMs across various domains, highlighting their future impact.

Building on the advances documented throughout this review, five scientific bottlenecks have been identified as the highest-priority targets for future research, ranked by their impact on the field's transition from laboratory demonstration to practical deployment.

(1) Nanoscale LC alignment—Priority: High.
Current photoalignment methods reliably achieve molecular ordering down to approximately 100 nm feature sizes; below this threshold, surface energy gradients from adjacent metallic structures dominate over the alignment layer's anchoring torque, producing unpredictable polydomain textures that elevate scattering losses and reduce device Q-factor. This barrier directly limits the operating frequency ceiling of LC-MM devices. Promising research directions include bio-inspired anchoring layers that mimic the hierarchical surface chemistry of biological alignment surfaces, and topology-optimized resonator geometries engineered to produce self-aligning LC configurations through deliberate surface energy patterning, eliminating the need for a separate alignment layer entirely.

(2) Low-voltage operation—Priority: High.
Current LC-MM drive voltages of 5–15 $V_{\mathrm{rms}}$ are incompatible with standard CMOS logic supply levels of 1.8–3.3 V, necessitating dedicated high-voltage driver circuitry that increases system complexity, power consumption, and cost. Closing this gap is a prerequisite for monolithic integration with CMOS readout and control electronics. Key research directions include ferroelectric LC phases, where spontaneous polarization enables sub-1 V switching through field-induced polarization reversal rather than director rotation, and DFLC mixtures, where reconfiguration is achieved by shifting drive frequency rather than increasing voltage amplitude.

(3) Ultrafast switching—Priority: Medium-High.
Millisecond-scale LC response times are sufficient for beam-steering and adaptive filtering applications, but are four to six orders of magnitude too slow for optical-packet-switching and ultrafast photonic routing, where nanosecond to picosecond reconfiguration is required. Blue phase LCs, which exhibit intrinsic sub-millisecond electro-optic response owing to their cubic lattice structure and absence of a slow elastic relaxation mode, represent the most mature near-term pathway. Polymer-stabilized nematic networks and plasmonic-enhanced all-optical switching via LC photoisomerization offer complementary routes to sub-microsecond operation.

**Table 12.** Key advantages, challenges, research directions, future directions, and potential applications of LC-enhanced metamaterials.

| Advantages | Challenges | Research directions | Future directions | Potential applications |
|---|---|---|---|---|
| Dynamic tunability with external stimuli [33, 178] | Fabrication complexity [179–181] | Develop nano-patterning and laser-assisted alignment | Multifunctional Devices | Imaging & Sensing [182] |
| Broad frequency range [35] | Temperature sensitivity | Combine LCs with low-loss materials like graphene [65] | Reconfigurable Devices | Telecommunications [183, 184] |
| Fast response times (optical/THz) | Cost and scalability challenges | Use high-birefringence materials for optical use [36] | Hybrid Metamaterials | Terahertz Devices [185–187] |
| Integration with existing technologies | Limited response speed in lower frequencies [188] | AI-Driven Design: Utilize machine learning for geometry optimization [189] | Cognitive Environments: Real-time adaptive EM spaces | Neuromorphic Computing [190] |
| Energy-efficient operation [103] | High sensitivity to alignment defects [36] | 3D Nanoprinting: Advanced manufacturing (e.g. TPP) | Wearable Photonics: Flexible and stretchable systems | Smart Windows |
| High sensitivity for sensing | Durability and aging issues | | Space Exploration: Telescopes and satellite comms | Adaptive Camouflage [103, 191] |
| Reconfigurable optical properties [192] | Limited tunability in some configurations | | | Quantum Sensors [193, 194] |
| Nonlinear optical capabilities [195] | Power consumption in continuous operation | | | Holographic Displays [196] |
| In-memory computing and fuzzy logic hardware based on LC hysteresis | | | | |

(4) CMOS integration—Priority: Medium.
The realization of large-scale programmable LC-MM platforms for 5 G/6 G RIS requires monolithic integration of LC cells with CMOS backplane electronics, analogous to the LCoS architecture established in display technology but adapted for millimetre-wave and THz operation. Key enabling research includes via-hole electrode array designs compatible with standard foundry design rules, and thin-film LC deposition processes compatible with back-end-of-line (BEOL) thermal budgets below 400 °C.

(5) Standardized characterization—Priority: Medium.
The absence of community-agreed reporting standards for LC-MM devices makes cross-laboratory comparison unreliable and impedes cumulative progress. At minimum, publications should report: centre frequency and tuning range under specified bias conditions; insertion loss at peak tuning; response time (both rise and fall); operating voltage; LC cell gap and mixture identity; alignment method; and number of characterized polarization states. Adoption of the FoMs proposed in section 3.5.2 of this review as community reporting standards would substantially improve reproducibility and accelerate the field's development.

LC-enhanced MMs are poised to revolutionize telecommunications by enabling the development of reconfigurable antennas, filters, and adaptive waveguides [197]. These devices can dynamically adjust their operating frequencies and radiation patterns, promoting more efficient exploitation of the electromagnetic bandwidth. For example, reconfigurable antennas could seamlessly switch between different communication standards, such as 5 G and 6 G, without the need for multiple hardware components. Additionally, LC-enhanced MMs could be used in beam-steering systems for satellite communications, improving signal strength and reducing interference. This adaptability makes them ideal for next-generation wireless networks, where flexibility and efficiency are critical.

Furthermore, the convergence of AI and ML with LC-enhanced MMs represents a transformative frontier in both device design and real-time operation. Traditional design workflows rely on iterative full-wave simulations (FDTD, FEM) requiring hours to days per design cycle, fundamentally limiting exploration of the vast LC-MM parameter space. AI-driven approaches disrupt this bottleneck across three distinct paradigms. First, forward neural network models, deep neural networks (DNNs) trained on simulation datasets, predict the electromagnetic response of an LC-MM unit cell given geometric parameters and LC director configuration as inputs, reducing inference time from hours to milliseconds and enabling rapid screening of thousands of candidate designs. Second, inverse design via tandem neural networks, variational autoencoders (VAEs), and generative adversarial networks (GANs) enables the reverse mapping: specifying a target electromagnetic response and automatically retrieving the corresponding device geometry and LC operating conditions. Applied to LC metasurface beam-steering, this approach has achieved 80% beam-switching efficiency and 144° steering angles—substantially exceeding the <30% efficiency typical of manually designed devices [198]. Third, reinforcement learning (RL) and topology optimization methods iteratively refine resonator geometries under fabrication-aware constraints, producing non-intuitive designs that simultaneously minimize insertion loss and maximize tuning range; Zhan *et al* recently demonstrated this for bidirectional MM absorbers, achieving performance metrics superior to all manually designed counterparts [189].

Beyond algorithmic design, AI plays a central operational role in programmable LC-MM platforms [199]. Deep learning models integrated into the control loops of RISs for 6 G networks can predict the electro-optical response of the LC layer in real time, adapting instantaneously to changing channel conditions without the computational latency of conventional Maxwell solvers [183]. This closed-loop AI-LC-RIS architecture—receiving real-time channel state information from the base station and reconfiguring the LC director field within the device response time (1.89–150 ms), has been identified as a key enabling technology for achieving the >120° beam coverage and >22.5% aperture efficiency targets of next-generation 6 G reflect array systems.

Beyond algorithmic and operational AI, the physical properties of LCs offer intrinsic hardware capabilities for neuromorphic computing. Certain LC phases—ferroelectric smectics and nanoparticle-doped nematics—exhibit significant hysteresis and memory effects, enabling retention of optical states without continuous power consumption [70]. This optical memory transforms metasurfaces from passive tunable devices into non-volatile storage elements. Furthermore, the continuous molecular reorientation of LCs allows for distinct analogue states aligned with fuzzy logic principles, suggesting that LC-enhanced MMs could serve as physical layers for neuromorphic computing, processing information directly through material response [200].

In the field of medical imaging, LC-enhanced MMs hold the potential to create superlenses that overcome the diffraction limit, enabling higher-resolution imaging than traditional lenses [201]. These

lenses could be used in advanced imaging systems, like optical coherence tomography (OCT) and magnetic resonance imaging (MRI), to provide clearer and more detailed images of biological tissues. Beyond imaging, LC-enhanced MMs could power biosensors capable of detecting minute changes in temperature or chemical composition with high sensitivity and specificity. Such sensors could revolutionize diagnostics, enabling early detection of diseases and real-time monitoring of environmental conditions.

The display industry is another area where LC-enhanced MMs are making significant strides. These materials are already being used in pixels, adaptive lenses, and holographic displays. Future advancements could lead to ultra-high-resolution displays with dynamic colour tuning and wide viewing angles, offering a more immersive visual experience. Moreover, LC-enhanced MMs could enhance AR and VR devices, creating more realistic and interactive environments. By enabling precise control over light, these materials could pave the way for next-generation optical devices that blur the line between the digital and physical worlds.

To solve the world's energy problems and advance renewable energy technology, these applications may be extremely important. Energy harvesting and storage systems could also benefit from LC-enhanced MMs; for example, tunable MMs could optimize light absorption in solar cells, increasing energy conversion efficiency across a wide range of wavelengths. Similarly, they could improve the efficiency of wireless power transfer systems, enabling more effective energy transmission over long distances.

Quantum photonics represents a prospective, rather than experimentally established, application domain for LC-integrated metasurfaces, and the distinction deserves emphasis. What has been demonstrated to date concerns static, all-dielectric metasurfaces operating in the quantum regime. Such platforms have performed multiphoton interference and full reconstruction of multiphoton polarization states [202], and have generated entanglement between the spin and orbital angular momentum of single photons [203]. When structured as metalens arrays, they have also served as high-dimensional, multi-path sources of entangled photon pairs [204] and produced complex multi-frequency quantum states through resonantly enhanced spontaneous parametric down-conversion [205]. Metasurface interferometry has further been proposed as a compact route toward quantum sensing [206], and the field has been consolidated in recent perspective articles [207]. In all of these demonstrations, however, the quantum-optical transformation implemented by the metasurface is fixed at the moment of fabrication. Physically, a dielectric metasurface acts on the photonic degrees of freedom by imposing a spatially varying Jones matrix: geometric (Pancharatnam–Berry) phase couples circular polarization to orbital angular momentum, while nanoresonator arrays define the multiport interference geometry that determines the output quantum state. Because LC reorientation modifies precisely this local Jones matrix through the effective index seen by each resonator, the same tuning mechanism described in section 2.2 would, in principle, render the quantum-optical transformation itself programmable.

The role envisaged for LCs is to make such transformations electrically reconfigurable, turning a fixed quantum-state preparation or tomography element into a programmable one, in the spirit of recently proposed space-time-modulated quantum metasurfaces [208]. Several caveats temper this prospect. First, no LC-tunable metasurface has yet been operated with non-classical light; the concept remains theoretical. Second, quantum logic imposes far stricter requirements than classical wavefront shaping: linear-optical two-photon gates are intrinsically probabilistic [209, 210], and any scattering or absorption introduced by the LC layer translates directly into photon loss and hence reduced gate fidelity, which disfavours lossy plasmonic implementations. The realistic near-term opportunities therefore lie not in high-fidelity quantum gates, but in reconfigurable quantum-state preparation, adaptive quantum tomography, and tunable front-end optics for quantum sensors. High-fidelity gate operation should instead be regarded as a long-term research direction, contingent on low-loss dielectric platforms and on experimental validation of LC-metasurface operation at the single-photon level.

LC-enhanced MMs could also play a key role in developing smart and adaptive environments. For example, they could be used in smart windows that dynamically adjust their transparency to control light and heat transmission, improving energy efficiency in buildings. Similarly, they could enable adaptive camouflage systems that change their appearance to blend in with the surroundings, with applications in defence and security. These materials could also enhance intelligent transportation systems, where adjustable properties could improve the efficiency and safety of autonomous vehicles.

LC-enhanced MMs represent promising candidates for space-based applications as another application area due to their special characteristics. They could be used in space-based telescopes to improve image quality and resolution, enabling more detailed observations of distant celestial objects. Additionally, they could enhance satellite communication systems increasing signal strength and reducing interference. These applications could significantly advance our capabilities in space exploration and communication.

At this point, the future of LC-enhanced MMs is exceptionally promising, with the capacity to transform a broad spectrum of industries and technologies. From revolutionizing telecommunications and advancing medical imaging to enabling next-generation displays and pioneering quantum technologies, the scope of possible applications is broad. As research continues to advance, the improvement of new LC materials, advanced fabrication techniques, and hybrid approaches will further enhance the functionality and performance of LC-enhanced MMs. By addressing challenges such as precise LC orientation, minimizing absorption losses, and scaling to optical frequencies, researchers can unlock the full potential of these materials, paving the way for a new era of innovation and discovery.

## 4. Conclusion

The integration of LCs with MMs has established a transformative framework for adaptive electromagnetic systems, merging the tunable properties of LCs with engineered subwavelength structures. By leveraging external stimuli such as electric fields and temperature, this synergy enables dynamic control over resonance frequencies, polarization states, and phase responses across microwave, terahertz, and optical regimes. Recent advancements include terahertz MMs achieving over 10% frequency tunability with millisecond-scale response times and optical metasurfaces demonstrating modulation depths of 18.3 dB. These innovations address the static limitations of conventional MMs, enabling reconfigurable filters, absorbers, and polarization converters critical for modern technologies.

Challenges such as optical losses in metallic nanostructures, precise LC alignment at subwavelength scales, and scalable fabrication remain barriers to practical implementation. Emerging strategies involve high-birefringence LCs, hybrid systems incorporating graphene or vanadium dioxide, and advanced manufacturing techniques like 3D nanoprinting. Computational tools, including FDTD simulations, have accelerated design optimization by modelling complex LC-MM interactions and predicting device performance.

Despite the breadth of device demonstrations reviewed here, it is important to acknowledge that only a handful of LC-MM concepts have progressed beyond laboratory proof-of-concept toward practical deployment. The primary barriers are not electromagnetic in nature, the tuning ranges and modulation depths reported across platforms are largely sufficient for target applications, but rather stem from the alignment, stability, and fabrication challenges detailed in sections 3.4.8 and 3.5. Specifically, the absence of scalable alignment solutions for sub-micron LC infiltration, the lack of long-term reliability data under realistic operating conditions, and the 10–100× cost premium relative to conventional LCD manufacturing collectively prevent industrialization. Addressing these barriers requires the field to shift emphasis from demonstrating new device geometries toward systematic characterization of device lifetime, yield, and environmental robustness—metrics that are conspicuously absent from the current literature.

The applications of LC-enhanced MMs span diverse domains. In telecommunications, reconfigurable antennas and beam-steering metasurfaces enhance 6 G network efficiency, exemplified by systems achieving 120° beam steering [84] with minimal power consumption. Medical imaging benefits from LC-tuned superlenses capable of sub-diffraction-limit resolution, while energy harvesting systems use tunable MMs to optimize solar cell efficiency under varying environmental conditions. Quantum photonics remains a prospective direction, in which LC-integrated metasurfaces could provide reconfigurable polarization control of entangled photons for secure communication and ultra-sensitive sensing.

Future progress hinges on interdisciplinary efforts to address thermal stability, fabrication scalability, and high-frequency losses. Innovations such as ML-driven design and quantum-material integration could unlock ultrafast, low-power devices. By bridging these gaps, LC-enhanced MMs will transition from laboratory prototypes to industrial applications, reshaping fields like AR, space exploration, and smart infrastructure.

To facilitate future cross-platform comparison, this review proposes standardized FoM adapted to each frequency regime: $\mathrm{FoM_{MW}}$ for microwave and mmWave systems, $\mathrm{FoM_{THz}}$ for THz devices, $\mathrm{FoM_{Opt}}$ for optical platforms, and $\mathrm{FoM_{speed}}$ for switching-speed-critical applications. Adoption of these metrics as community reporting standards would substantially improve the reproducibility and comparability of LC-MM research.

In summary, the fusion of LCs with MMs represents a paradigm shift in photonics, offering unprecedented adaptability across the electromagnetic spectrum. Continued advancements in materials, fabrication, and computational modelling will drive their real-world impact, transforming both cutting-edge

technologies and everyday applications. Addressing existing challenges through collaborative research will unlock the full potential of these dynamic systems, paving the way for multifunctional devices that revolutionize technology and improve daily life.

## Acknowledgment

This work was supported by the research project of Kocaeli University with Grant Number FKA-2024-3938.

## Data availability statement

No new data were generated or analysed in support of this review.

## Conflict of interest

The authors declare that they have no known competing financial interests or personal relationships that could have appeared to influence the work reported in this paper.

## Author contributions

Gülcan Aydın 0000-0003-4627-961X
Conceptualization (equal), Investigation (equal), Methodology (equal), Validation (equal), Visualization (equal), Writing – original draft (equal), Writing – review & editing (equal)

İdris Candan 0000-0002-9950-713X
Investigation (equal), Methodology (equal), Writing – review & editing (equal)

Mahpeyker Kocakoç Toprakoğlu 0000-0001-7966-1482
Investigation (equal)

Sait Eren San 0000-0001-5042-4555
Methodology (equal), Supervision (equal)

## References

[1] Lee Y 2025 Metamaterials and their devices *Crystals* **15** 119
[2] Shelby R A, Smith D R and Schultz S 2001 Experimental verification of a negative index of refraction *Science* **292** 77–79
[3] Valentine J, Li J, Zentgraf T, Bartal G and Zhang X 2009 An optical cloak made of dielectrics *Nat. Mater.* **8** 568–71
[4] Schurig D, Mock J J, Justice B J, Cummer S A, Pendry J B, Starr A F and Smith D R 2006 Metamaterial electromagnetic cloak at microwave frequencies *Science* **314** 977–80
[5] Zhang X and Liu Z 2008 Superlenses to overcome the diffraction limit *Nat. Mater.* **7** 435–41
[6] Haxha S, AbdelMalek F, Ouerghi F, Charlton M D B, Aggoun A and Fang X 2018 Metamaterial superlenses operating at visible wavelength for imaging applications *Sci. Rep.* **8** 16119
[7] Fang N, Lee H, Sun C and Zhang X 2005 Sub-diffraction-limited optical imaging with a silver superlens *Science* **308** 534–7
[8] Veselago V G 1968 The electrodynamics of substances with simultaneously negative values of $\varepsilon$ and $\mu$ *Sov. Phys. Usp.* **10** 509
[9] Pendry J B, Holden A J, Robbins D J and Stewart W J 1999 Magnetism from conductors and enhanced nonlinear phenomena *IEEE Trans. Microw. Theory Tech.* **47** 2075–84
[10] Pendry J B 2000 Negative refraction makes a perfect lens *Phys. Rev. Lett.* **85** 3966
[11] Smith D R, Padilla W J, Vier D C, Nemat-nasser S C and Schultz S 2000 Composite medium with simultaneously negative permeability and permittivity *Phys. Rev. Lett.* **84** 4184–7
[12] Liu Z, Zhang X, Mao Y, Zhu Y Y, Yang Z, Chan C T and Sheng P 2000 Locally resonant sonic materials *Science* **289** 1734–6
[13] Tao H, Landy N I, Bingham C M, Zhang X, Averitt R D and Padilla W J 2008 A metamaterial absorber for the terahertz regime: design, fabrication and characterization *Opt. Express* **16** 7181–8
[14] Lagerwall J P F and Scalia G 2012 A new era for liquid crystal research: applications of liquid crystals in soft matter nano-, bio- and microtechnology *Curr. Appl. Phys.* **12** 1387–412
[15] Zhou S, Sokolov A, Lavrentovich O D and Aranson I S 2014 Living liquid crystals *Proc. Natl Acad. Sci. USA* **111** 1265–70
[16] Khoo I C 2014 Nonlinear optics, active plasmonics and metamaterials with liquid crystals *Prog. Quantum Electron.* **38** 77–117
[17] Karyappa R *et al* 2025 Unlocking the potential of liquid crystals as phase change materials for thermal energy storage *Energy Mater.* **5** 500037
[18] Singh S 2024 Advanced applications of liquid crystals *Handbook of Liquid Crystals* vol II (Wiley) pp 601–65
[19] Zhang Z, Yang X, Zhao Y, Ye F and Shang L 2023 Liquid crystal materials for biomedical applications *Adv. Mater.* **35** 2300220

[20] Yin K, Hsiang E-L, Zou J, Li Y, Yang Z, Yang Q, Lai P-C, Lin C-L and Wu S-T 2022 Advanced liquid crystal devices for augmented reality and virtual reality displays: principles and applications *Light Sci Appl.* **11** 1–22
[21] Bisoyi H K and Li Q 2022 Liquid crystals: versatile self-organized smart soft materials *Chem. Rev.* **122** 4887–926
[22] Ma L-L, Li C Y, Pan J-T, Ji Y-E, Jiang C, Zheng R, Wang Z-Y, Wang Y, Li B-X and Lu Y-Q 2022 Self-assembled liquid crystal architectures for soft matter photonics *Light Sci Appl.* **11** 270
[23] Xiong J and Wu S-T 2021 Planar liquid crystal polarization optics for augmented reality and virtual reality: from fundamentals to applications *eLight* **1** 3
[24] Shrekenhamer D, Chen W-C and Padilla W J 2013 Liquid crystal tunable metamaterial absorber *Phys. Rev. Lett.* **110** 177403
[25] Yang L, Fan F, Chen M, Zhang X and Chang S-J 2017 Active terahertz metamaterials based on liquid-crystal induced transparency and absorption *Opt. Commun.* **382** 42–48
[26] Kim H, Oh S, Bang S, Yang H, Kim B and Oh J 2023 Independently polarization manipulable liquid-crystal-based reflective metasurface for 5G reflectarray and reconfigurable intelligent surface *IEEE Trans. Antennas Propag.* **71** 6606–16
[27] Yang J, Zheng G, Zha X, Xi H, Yin Z, Zhu J and Deng G 2024 Coded digital inspired tunable metamaterial absorber based on liquid crystals *Opt. Commun.* **565** 130653
[28] Li S-Q, Xu X, Veetil R M, Valuckas V, Paniagua-Domínguez R and Kuznetsov A I 2019 Phase-only transmissive spatial light modulator based on tunable dielectric metasurface *Science* **364** 1087–90
[29] Wu J *et al* 2020 Liquid crystal programmable metasurface for terahertz beam steering *Appl. Phys. Lett.* **116** 131104
[30] Gorkunov M V, Kasyanova I V, Artemov V V, Barnik M, Geivandov A and Palto S 2017 Fast surface-plasmon-mediated electro-optics of a liquid crystal on a metal grating *Phys. Rev. Appl.* **8** 054051
[31] Buchnev O, Podoliak N and Fedotov V A 2018 Liquid crystal-filled meta-pixel with switchable asymmetric reflectance and transmittance *J. Mol. Liq.* **267** 411–4
[32] Buchnev O, Podoliak N, Kaltenecker K, Walther M and Fedotov V A 2020 Metasurface-based optical liquid crystal cell as an ultrathin spatial phase modulator for THz applications *ACS Photon.* **7** 3199–206
[33] Li J, Chen J, Yan D, Fan F, Chen K, Zhong K, Wang Y, Tian Z and Xu D 2024 A review: active tunable terahertz metamaterials *Adv. Photonics Res.* **5** 2300351
[34] Kang D, Heo H, Yang Y, Seong J, Kim H, Kim J and Rho J 2024 Liquid crystal-integrated metasurfaces for an active photonic platform *Opto-Electron. Adv.* **7** 230216
[35] Gorkunov M V, Miroshnichenko A E and Kivshar Y S 2015 Metamaterials tunable with liquid crystals *Springer Series in Materials Science* (Springer) pp 237–53
[36] Wang L, Wang Y, Zong G, Hu W and Lu Y 2025 Liquid crystal based tunable terahertz metadevices *J. Materiomics* **11** 100888
[37] Maier W and Saupe A 1958 Eine einfache molekulare Theorie des nematischen kristallinflüssigen Zustandes *Z. Naturforsch. A* **13** 564–6
[38] de Gennes P-G and Prost J 1995 *The Physics of Liquid Crystals* 2nd edn (Clarendon)
[39] Oseen C W 1933 The theory of liquid crystals *Trans. Faraday Soc.* **29** 883–99
[40] Frank F C 1958 I. Liquid crystals: on the theory of liquid crystals *Discuss. Faraday Soc.* **25** 19–28
[41] Fréedericksz V and Zolina V 1933 Forces causing the orientation of an anisotropic liquid *Trans. Faraday Soc.* **29** 919–30
[42] Leslie F M 1968 Some constitutive equations for liquid crystals *Arch. Ration. Mech. Anal.* **28** 265–83
[43] Rapini A and Papoular M 1969 Distorsion d'une lamelle nématique sous champ magnétique conditions d'ancrage aux parois *J. Phys. Colloq.* **30** C4–54–C4–56
[44] Khoo I-C 2007 Liquid Crystals *Wiley Series in Pure and Applied Optics* 2nd edn (Wiley)
[45] Green M and Madden S J 1989 Low loss nematic liquid crystal cored fiber waveguides *Appl. Opt.* **28** 5202–3
[46] Tanggaard Larsen T, Bjarklev A, Sparre Hermann D and Broeng J 2003 Optical devices based on liquid crystal photonic bandgap fibres *Opt. Express* **11** 2589–96
[47] Du F, Lu Y-Q and Wu S-T 2004 Electrically tunable liquid-crystal photonic crystal fiber *Appl. Phys. Lett.* **85** 2181–3
[48] Alkeskjold T T, Lægsgaard J, Bjarklev A, Hermann D S, Anawati A, Broeng J, Li J and Wu S-T 2004 All-optical modulation in dye-doped nematic liquid crystal photonic bandgap fibers *Opt. Express* **12** 5857–71
[49] Woliński T R, Ertman S, Lesiak P, Domański A, Czapla A, Dąbrowski R, Nowinowski-Kruszelnicki E and Wójcik J 2006 Photonic liquid crystal fibers—a new challenge for fiber optics and liquid crystals photonics *Opto-Electron. Rev.* **14** 329–34
[50] Suzuki M, Ohara S, Sakamoto M, Noda K, Sasaki T, Kawatsuki N and Ono H 2024 Temperature dependence of the diffraction efficiency of circular polarization gratings made by liquid crystal molecules with anisotropic absorption *Opt. Mater. Express* **14** 1857
[51] Skutnik R A, Eichler J C, Mazza M G and Schoen M 2021 The temperature dependence of the helical pitch in a cholesteric liquid crystal *Mol. Phys.* **119** 15–16
[52] Okutan M, Yakuphanoglu F, San S E and Koysal O 2005 Impedance spectroscopy and dielectric anisotropy-type analysis in dye-doped nematic liquid crystals having different preliminary orientations *Physica B* **368** 308–17
[53] Tsai T-R, Chen C-Y, Pan C-L, Pan R-P and Zhang X-C 2003 Terahertz time-domain spectroscopy studies of the optical constants of the nematic liquid crystal 5CB *Appl. Opt.* **42** 2372
[54] Yang C-S, Lin C-J, Pan R-P, Que C T, Yamamoto K, Tani M and Pan C-L 2010 The complex refractive indices of the liquid crystal mixture E7 in the terahertz frequency range *J. Opt. Soc. Am. B* **27** 1866–73
[55] Vieweg N, Shakfa M K and Koch M 2011 BL037: a nematic mixture with high terahertz birefringence *Opt. Commun.* **284** 1887–9
[56] Wang L, Lin X, Liang X, Wu J, Hu W, Zheng Z-G, Jin B-B, Qin Y-Q and Lu Y-Q 2012 Large birefringence liquid crystal material in terahertz range *Opt. Mater. Express* **2** 1314–9
[57] Chodorow U, Mavrona E, Palka N, Strzezysz O, Garbat K, Saitzek S, Blach J F, Apostolopoulos V, Kaczmarek M and Parka J 2017 Terahertz properties of liquid crystals doped with ferroelectric $BaTiO_3$ nanoparticles *Liq. Cryst.* **44** 1207–15
[58] Reuter M, Vieweg N, Fischer B M, Mikulicz M, Koch M, Garbat K and Dąbrowski R 2013 Highly birefringent, low-loss liquid crystals for terahertz applications *APL Mater.* **1** 012107
[59] Yin S, Xiao D, Liu J, Li K, He H, Jiang S, Luo D, Sun X W, Ji W and Liu Y J 2018 Reconfigurable chiral metasurface absorbers based on liquid crystals *IEEE Photonics J.* **10** 2878775
[60] Muravsky A and Murauski A 2024 Q&A of liquid crystal alignment: theory and practice *Front. Soft Matter* **4** 1382925
[61] Yin K, Xiong J, He Z and Wu S-T 2020 Patterning liquid-crystal alignment for ultrathin flat optics *ACS Omega* **5** 31485–9
[62] Yaroshchuk O and Reznikov Y 2011 Photoalignment of liquid crystals: basics and current trends *J. Mater. Chem.* **22** 286–300
[63] Chigrinov V, Sun J and Wang X 2020 Photoaligning and photopatterning: new LC technology *Crystals* **10** 323

[64] Babakhanova G and Lavrentovich O D 2019 The techniques of surface alignment of liquid crystals *Springer Proc. Phys.* **223** 165–97
[65] Wang L, Ge S, Hu W, Nakajima M and Lu Y 2017 Graphene-assisted high-efficiency liquid crystal tunable terahertz metamaterial absorber *Opt. Express* **25** 23873–9
[66] Chiang W-F, Lin S-X, Lee Y-X, Shih Y-H, Liu J-H, Silalahi H-M, Lee C-R and Huang C-Y 2021 Effect of thicknesses of liquid crystal layers on shift of resonance frequencies of metamaterials *Coatings* **11** 578
[67] Wang P Y, Rennings A and Erni D 2023 A tunable metamaterial element based on liquid crystals for holographic beam-steering antennas *2023 IEEE MTT-S Int. Wireless Symp. (IWS)* (IEEE) pp 1–3
[68] Zhang F, Zhang W, Zhao Q, Sun J, Qiu K, Zhou J and Lippens D 2011 Electrically controllable fishnet metamaterial based on nematic liquid crystal *Opt. Express* **19** 1563–8
[69] Qiu K, Jia N, Liu Z, Wu C, Fan Y, Fu Q, Zhang F and Zhang W 2016 Electrically reconfigurable split ring resonator covered by nematic liquid crystal droplet *Opt. Express* **24** 27096–103
[70] Gdovinová V, Tomašovičová N, Jeng S-C, Zakutanská K, Kula P and Kopčanský P 2019 Memory effect in nematic phase of liquid crystal doped with magnetic and non-magnetic nanoparticles *J. Mol. Liq.* **282** 286–91
[71] Zhao Q, Kang L, Du B, Li B, Zhou J, Tang H, Liang X and Zhang B 2007 Electrically tunable negative permeability metamaterials based on nematic liquid crystals *Appl. Phys. Lett.* **90** 011112
[72] Decker M, Kremers C, Minovich A, Staude I, Miroshnichenko A E, Chigrin D, Neshev D N, Jagadish C and Kivshar Y S 2013 Electro-optical switching by liquid-crystal controlled metasurfaces *Opt. Express* **21** 8879–85
[73] Sasaki T, Nishie Y, Kambayashi M, Sakamoto M, Noda K, Okamoto H, Kawatsuki N and Ono H 2019 Active terahertz polarization converter using a liquid crystal-embedded metal mesh *IEEE Photonics J.* **11** 1–7
[74] Kowerdziej R, Wróbel J and Kula P 2019 Ultrafast electrical switching of nanostructured metadevice with dual-frequency liquid crystal *Sci. Rep.* **9** 1–8
[75] Sharma M, Hendler N and Ellenbogen T 2020 Electrically switchable color tags based on active liquid-crystal plasmonic metasurface platform *Adv. Opt. Mater.* **8** 1901182
[76] Wu J, Yao S, Zhang H, Man W, Bai Z, Zhang F, Wang X, Fang D and Zhang Y 2021 Liquid crystal elastomer metamaterials with giant biaxial thermal shrinkage for enhancing skin regeneration *Adv. Mater.* **33** 2106175
[77] Buchnev O *et al* 2013 Electrically controlled liquid crystal plasmonic metamaterials *2013 Conf. on Lasers and Electro-Optics—International Quantum Electronics Conf.* (Optica Publishing Group)
[78] Buchnev O, Podoliak N, Kaczmarek M, Zheludev N I and Fedotov V A 2015 Electrically controlled nanostructured metasurface loaded with liquid crystal: toward multifunctional photonic switch *Adv. Opt. Mater.* **3** 674–9
[79] Lee Y U, Kim J and Wu J W 2015 Electro-optic switching in metamaterial by liquid crystal *Nano Converg.* **2** 23
[80] Mirbagheri G and Crouse D 2022 Design, fabrication, and spectral characterization of temperature-dependent liquid crystal-based metamaterial to tune dielectric metasurface resonances *Proc. SPIE* **12000** 50
[81] Song X, Zhang W, Liu H, Zhao L, Chen Q and Tian H 2022 3D printing of liquid crystal elastomers-based actuator for an inchworm-inspired crawling soft robot *Front Robot AI* **9** 889848
[82] Lv J-F, Meng F-Y, Zhang K, Han J-Q, Liu Y-H, Ding C and Wu Q 2022 Tunable liquid crystal metamaterial filter with polarization-insensitive characteristic *Liq. Cryst.* **49** 1338–46
[83] Wang P-Y, Sievert B, Svejda J T, Benson N, Meng F-Y, Rennings A and Erni D 2023 A liquid crystal tunable metamaterial unit cell for dynamic metasurface antennas *IEEE Trans. Antennas Propag.* **71** 1135–40
[84] Park J, Yoo Y, Lee C, Yoon D K and Park S-O 2024 Liquid-crystal-based beam steering guided-wave metasurface antenna at millimeter-wave band *IEEE Antennas Wirel. Propag. Lett.* **23** 4208–12
[85] Lin C C, Lin G S, Ke G J and Chou H H 2021 Tunable frequency selective surface (FSS) based on LC material for mmWave communications *2021 Int. Symp. on Antennas and Propagation* (ISAP) (https://doi.org/10.23919/ISAP47258.2021.9614366)
[86] Paik S *et al* 2020 Near-field sub-diffraction photolithography with an elastomeric photomask *Nat. Commun.* **11** 805
[87] Al-amri M, Liao Z and Zubairy M S 2012 Beyond the rayleigh limit in optical lithography *Adv. At. Mol. Opt. Phys.* **61** 409–66
[88] Gan Z, Cao Y, Evans R A and Gu M 2013 Three-dimensional deep sub-diffraction optical beam lithography with 9 nm feature size *Nat. Commun.* **4** 2061
[89] Tan Y S, Wang H, Wang H, Pan C and Yang J K W 2023 High-throughput fabrication of large-scale metasurfaces using electron-beam lithography with SU-8 gratings for multilevel security printing *Photonics Res.* **11** B103–B10
[90] Wei K *et al* 2025 Novel focused ion beam techniques for enhanced sample preparation for *in situ* transmission electron microscopy heating and irradiation experiments *Microsc. Microanal.* **31** 29
[91] Lan Y W, Chang W H, Chang Y C, Chang C-S and Chen C-D 2015 Effect of focused ion beam deposition induced contamination on the transport properties of nano devices *Nanotechnology* **26** 055705
[92] Agarwal R, Barretta R and Schift H 2025 Nanoimprint—Mo(o)re than lithography *Encyclopedia* **5** 197
[93] Zhang W *et al* 2018 Metafluidic metamaterial: a review *Adv. Phys. X* **3** 165–84
[94] Gorkunov M V and Osipov M A 2008 Tunability of wire-grid metamaterial immersed into nematic liquid crystal *J. Appl. Phys.* **103** 036101
[95] Liu L, Shadrivov I V, Powell D A, Raihan R, Hattori H T, Decker M, Mironov E and Neshev D N 2013 Temperature control of terahertz metamaterials with liquid crystals *IEEE Trans. Terahertz Sci. Technol.* **3** 827–31
[96] Kowerdziej R, Olifierczuk M, Parka J and Wróbel J 2014 Terahertz characterization of tunable metamaterial based on electrically controlled nematic liquid crystal *Appl. Phys. Lett.* **105** 022908
[97] Maasch M, Roig M, Damm C and Jakoby R 2014 Voltage-tunable artificial gradient-index lens based on a liquid crystal loaded fishnet metamaterial *IEEE Antennas Wirel. Propag. Lett.* **13** 1581–4
[98] Jiang S-A, Chen C-C, Wang S-H, Jiang S-A, Chang T-H, Wang S-H and Huang C-Y 2015 Continuously tunable and fast-response terahertz metamaterials using in-plane-switching dual-frequency liquid crystal cells *Opt. Lett.* **40** 2021–4
[99] Zografopoulos D C and Beccherelli R 2015 Tunable terahertz fishnet metamaterials based on thin nematic liquid crystal layers for fast switching *Sci. Rep.* **5** 1–11
[100] Komar A *et al* 2017 Electrically tunable all-dielectric optical metasurfaces based on liquid crystals *Appl. Phys. Lett.* **110** 071109
[101] Yang J, Wang P, Shi T, Gao S, Lu H, Yin Z, Lai W and Deng G 2019 Electrically tunable liquid crystal terahertz device based on double-layer plasmonic metamaterial *Opt. Express* **27** 27039–45
[102] Bhardwaj A, Sridurai V, Puthoor N M, Nair A B, Ahuja T and Nair G G 2020 Evidence of tunable Fano resonance in a liquid crystal-based colloidal metamaterial *Adv. Opt. Mater.* **8** 1901842

[103] Liu Y, Song J, Zhao W, Ren X, Cheng Q, Luo X, Fang N X and Hu R 2020 Dynamic thermal camouflage via a liquid-crystal-based radiative metasurface *Nanophotonics* **9** 855–63
[104] Sandford O'Neill J J, Salter P S, Booth M J, Elston S J and Morris S M 2020 Electrically-tunable positioning of topological defects in liquid crystals *Nat. Commun.* **11** 1–8
[105] Muller J *et al* 2003 Electrically controlled light scattering with metal nanoparticles *Conf. on Lasers and Electro-Optics Europe—Technical Digest* vol 524
[106] Draper M, Saez I M, Cowling S J, Gai P, Heinrich B, Donnio B, Guillon D and Goodby J W 2011 Self-assembly and shape morphology of liquid crystalline gold metamaterials *Adv. Funct. Mater.* **21** 1260–78
[107] Chu K C, Chao C Y, Chen Y F, Wu Y C and Chen C C 2006 Electrically controlled surface plasmon resonance frequency of gold nanorods *Appl. Phys. Lett.* **89** 103107
[108] Franklin D, Frank R, Wu S T and Chanda D 2017 Actively addressed single pixel full-colour plasmonic display *Nat. Commun.* **8** 1–10
[109] Sharma M, Michaeli L, Haim Ben D and Ellenbogen T 2022 Liquid crystal switchable surface lattice resonances in plasmonic metasurfaces *ACS Photonics* **9** 2702–12
[110] Abdulhalim I 2012 Liquid crystal active nanophotonics and plasmonics: from science to devices *J. Nanophotonics* **6** 061001
[111] Vahedi A and Kouhi M 2020 Liquid crystal-based surface plasmon resonance biosensor *Plasmonics* **15** 61–71
[112] Khorasaninejad M, Chen W T, Devlin R C, Oh J, Zhu A Y and Capasso F 2016 Metalenses at visible wavelengths: diffraction-limited focusing and subwavelength resolution imaging *Science* **352** 1190–4
[113] Aieta F, Genevet P, Khorasaninejad M, Khorasaninejad M and Devlin R 2017 Recent advances in planar optics: from plasmonic to dielectric metasurfaces *Optica* **4** 139–52
[114] Kasyanova I V, Gorkunov M V and Palto S P 2022 Liquid-crystal metasurfaces: self-assembly for versatile optical functionality *Europhys. Lett.* **136** 24001
[115] Zhu Z *et al* 2023 Metasurface-enabled polarization-independent LCoS spatial light modulator for 4K resolution and beyond *Light Sci Appl.* **12** 1–10
[116] Wang S *et al* 2024 Electrically active terahertz liquid-crystal metasurface for polarization vortex beam switching *Laser Photon. Rev.* **18** 2301301
[117] Habibpourmoghadam A, Evlyukhin A and Lesina A C 2024 Reconfigurable collective resonances induced by liquid crystals in dielectric metasurfaces (arXiv:2404.17788)
[118] Chen K-P, Ye S-C, Yang C-Y, Yang Z-H, Lee W and Sun M-G 2016 Electrically tunable transmission of gold binary-grating metasurfaces integrated with liquid crystals *Opt. Express* **24** 16815
[119] Izdebskaya Y V, Yang Z, Shvedov V G, Neshev D N and Shadrivov I V 2023 Multifunctional metasurface tuning by liquid crystals in three dimensions *Nano Lett.* **23** 9825–31
[120] Shih Y-H, Lin X-Y, Silalahi H M, Lee C-R and Huang C-Y 2021 Optically tunable terahertz metasurfaces using liquid crystal cells coated with photoalignment layers *Crystals* **11** 1100
[121] Ji Y-Y, Fan F, Chen M, Yang L and Chang S-J 2017 Terahertz artificial birefringence and tunable phase shifter based on dielectric metasurface with compound lattice *Opt. Express* **25** 11405
[122] Fan F, Zhao H-J, Ji Y-Y, Jiang S-L, Tan Z-Y, Cheng J-R and Chang S-J 2023 Spin-decoupled beam steering with active optical chirality based on terahertz liquid crystal chiral metadevice *Adv. Mater. Interfaces* **10** 2202103
[123] Zhao H, Liu J, Jiang S, Jiang X, Cheng J, Ji Y, Chang S and Fan F 2023 Broadband large-angle beam scanning with dynamic spin energy distribution based on liquid crystal cascaded bilayer metasurface *Nanophotonics* **12** 3945
[124] Shen Z, Zhou S, Li X, Ge S, Chen P, Hu W and Lu Y 2020 Liquid crystal integrated metalens with tunable chromatic aberration *Adv. Photon.* **2** 036002
[125] Gao S, Xu J, Cao J, Yao H, Ali S E, Abo-dief H M, Alanazi A K, Lan C, Algadi H and Zhai X 2023 Highly efficient tunable terahertz all-dielectric metasurface absorber based on high mode *Adv. Compos. Hybrid Mater.* **6** 116
[126] Zhao H-J, Fan F, Zhang T-R, Ji Y-Y and Chang S-J 2022 Dynamic terahertz anisotropy and chirality enhancement in liquid-crystal anisotropic dielectric metasurfaces *Photonics Res.* **10** 1097–106
[127] Gay-balmaz P and Martin O J F 2002 Electromagnetic resonances in individual and coupled split-ring resonators *J. Appl. Phys.* **92** 2929–36
[128] Baena J D 3 2005 Equivalent-circuit models for split-ring resonators and complementary split-ring resonators coupled to planar transmission lines *IEEE Trans. Microw. Theory Tech.* **53** 1451–60
[129] Marqués R, Martel J, Mesa F and Medina F 2002 Left-handed-media simulation and transmission of EM waves in subwavelength split-ring-resonator-loaded metallic waveguides *Phys. Rev. Lett.* **89** 183901
[130] Salim A and Lim S 2018 Review of recent metamaterial microfluidic sensors *Sensors* **18** 232
[131] Zhang F *et al* 2008 Magnetic control of negative permeability metamaterials based on liquid crystals *Proceedings 38th European Microwave Conf.* (EuMC 2008) pp 801–4
[132] Kowerdziej R, Parka J and Krupka J 2011 Experimental study of thermally controlled metamaterial containing a liquid crystal layer at microwave frequencies *Liq. Cryst.* **38** 743–7
[133] Atorf B, Mühlenbernd H, Zentgraf T and Kitzerow H-S 2020 All-optical switching of a dye-doped liquid crystal plasmonic metasurface *Opt. Express* **28** 8898–908
[134] Pusovnik A, Aplinc J and Ravnik M 2019 Optical properties of metamaterial split ring nematic colloids *Sci. Rep.* **9** 1–10
[135] Ding C, Meng F Y, Mu H L, Han J-Q, Zhao C-H, Fang Q-Y and Wu Q 2019 Design of filtering tunable liquid crystal phase shifter based on coplanar waveguide and split-ring resonators *Liq. Cryst.* **46** 2127–33
[136] Liu Y *et al* 2019 Frequency reconfigurable SRR filter based on nematic liquid crystal for microwave applications *30th Irish Signals and Systems Conf.* (ISSC 2019) (https://doi.org/10.1109/ISSC.2019.8904958)
[137] Martinic M, Markovic T, Baric A and Nauwelaers B 2021 A 4 × 4 array of complementary split-ring resonators for label-free dielectric spectroscopy *Chemosensors* **9** 348
[138] Minovich A *et al* 2010 Infrared metamaterials tuned by liquid crystals *Conf. Optoelectronic and Microelectronic Materials and Devices* (Proceedings, COMMAD) pp 27–28
[139] Kruk S *et al* 2012 Tunable and nonlinear fishnet metamaterials based on liquid crystal infiltration *Proc. SPIE* **8455** 84552O (https://doi.org/10.1117/12.931309)
[140] Diepolder A, Schmidt L, Brandl S, Hinz P, Waldschmidt C and Damm C 2025 Hybrid fishnet metamaterial based on liquid crystal and p-i-n diodes for reconfigurable transmitarrays at 10 GHz *IEEE J. Microw.* **5** 96–107
[141] Wang D S, Qu S-W and Chan C H 2016 Frequency Selective Surfaces *Handbook of Antenna Technologies* (Springer) pp 471–525

[142] Munk B A 2000 *Frequency Selective Surfaces* (Wiley)
[143] Shavit R 2018 Frequency selective surfaces (FSS) radomes *Radome Electromagnetic Theory and Design* (Wiley) pp 39–88
[144] Kapoor A, Mishra R and Kumar P 2022 Frequency selective surfaces as spatial filters: fundamentals, analysis and applications *Alexandria Eng. J.* **61** 4263–93
[145] Mondal K 2019 Bandwidth and gain enhancement of microstrip antenna by frequency selective surface for WLAN, WiMAX applications *Sādhanā* **44** 233
[146] Güneş F, Sharipov Z, Belen M A and Mahouti P 2017 GSM filtering of horn antennas using modified double square frequency selective surface *Int. J. RF Microw. Comput. Aided Eng.* **27** e21136
[147] Anwar R S, Mao L and Ning H 2018 Frequency selective surfaces: a review *Appl. Sci.* **8** 1689
[148] Hu W, Dickie R, Cahill R, Gamble H, Ismail Y, Fusco V, Linton D, Grant N and Rea S 2007 Liquid crystal tunable mm wave frequency selective surface *IEEE Microw. Wirel. Compon. Lett.* **17** 667–9
[149] Wang R and Cai L 2020 Liquid crystal based reconfigurable frequency selective surface for ISM applications *2020 IEEE Asia-Pacific Conf. Antennas and Propagation* (APCAP 2020—Proceedings)
[150] Li R *et al* 2021 Reconfigurable frequency selective surface based on liquid crystal *2021 Int. Conf. Microwave and Millimeter Wave Technology* (ICMMT 2021—Proceedings)
[151] Lv J F, Ding C, Zhu Z, Li X, Meng F-Y, Han J-Q, Jin T and Wu Q 2021 Tunable liquid crystal frequency selective surface with the compact unit cell, large tuning range, and the passband of flat-top and sharp roll-off *J. Phys. D: Appl. Phys.* **54** 315001
[152] Yang F, Liu H, Wang T, Zhang Y, Wei J, Feng Z and Wang Z 2024 Tunable liquid crystal double-layer frequency selective surface with wide transmission band and small insertion loss *Liq. Cryst.* **51** 2011–23
[153] Dierking I 2014 Chiral liquid crystals: structures, phases, effects *Symmetry* **6** 444–72
[154] Ji W, Yin S, Sun X W, Liu J, Ji W, Wang B, Luo D, Li G and Sun X W 2018 Liquid-crystal-loaded chiral metasurfaces for reconfigurable multiband spin-selective light absorption *Opt. Express* **26** 25305–14
[155] Wang L, Urbas A M and Li Q 2020 Nature-inspired emerging chiral liquid crystal nanostructures: from molecular self-assembly to DNA mesophase and nanocolloids *Adv. Mater.* **32** 1801335
[156] Zhang X, Xu Y, Valenzuela C, Gong W, Zhang Y, Han S and Situ G 2022 Liquid crystal-templated chiral nanomaterials: from chiral plasmonics to circularly polarized luminescence *Light Sci Appl.* **11** 1–29
[157] Guirado R, Perez-Palomino G, Ferreras M, Carrasco E and Cano-garcia M 2022 Dynamic modelling of liquid crystal-based metasurfaces and its application to reducing reconfigurability times *IEEE Trans. Antennas Propag.* **70** 11847–57
[158] Zhang F, Zhao Q, Gaillot D P, Zhao X and Lippens D 2008 Numerical investigation of metamaterials infiltrated by liquid crystal *J. Opt. Soc. Am. B* **25** 1920–5
[159] Sakhare P A, Atmakuri M and Dontabhaktuni J 2023 Tailoring the resonant modes in liquid crystal based all-dielectric metasurfaces *Sci. Rep.* **13** 6780
[160] Yang X, Gregory Forest M, Li H, Liu C, Shen J, Wang Q and Chen F 2013 Modeling and simulations of drop pinch-off from liquid crystal filaments and the leaky liquid crystal faucet immersed in viscous fluids *J. Comput. Phys.* **236** 1–14
[161] Kowerdziej R, Parka J, Nyga P and Salski B 2011 Simulation of a tunable metamaterial with nematic liquid crystal layers *Liq. Cryst.* **38** 377–9
[162] Wang J, Tian H, Wang Y, Li X, Cao Y, Li L, Liu J and Zhou Z 2018 Liquid crystal terahertz modulator with plasmon-induced transparency metamaterial *Opt. Express* **26** 5769–76
[163] Vasić B, Zografopoulos D C, Isić G, Beccherelli R and Gajić R 2017 Electrically tunable terahertz polarization converter based on overcoupled metal-isolator-metal metamaterials infiltrated with liquid crystals *Nanotechnology* **28** 124002
[164] Song K, Wang J and Wang G 2025 Rigorous coupled-wave analysis algorithm for stratified two-dimensional gratings with unconditionally stable H-matrix methods *Photonics* **12** 943
[165] Perez-Palomino G, Florencio R, Encinar J A, Barba M, Dickie R, Cahill R, Baine P, Bain M and Boix R R 2014 Accurate and efficient modeling to calculate the voltage dependence of liquid crystal-based reflectarray cells *IEEE Trans. Antennas Propag.* **62** 2659–68
[166] Gallego Rico S and Zitzenbacher G 2025 Modeling approach to calculate the orientation of liquid crystal polymers in a flow channel under varying boundary conditions *Polymers* **17** 2209
[167] Izdebskaya Y V, Yang Z, Liu M, Choi D-Y, Komar A, Neshev D N and Shadrivov I V 2022 Magnetic tuning of liquid crystal dielectric metasurfaces *Nanophotonics* **11** 3895–900
[168] Helaly D M M, Hameed M F O, Areed N F F, Obayya S S A and Saadeldin A S 2026 Design, fabrication and characterization of metamaterial absorber for sensing applications *Sci. Rep.* **16** 8268
[169] Mamonova A V, Simdyankin I V, Kasyanova I V, Artemov V V, Geivandov A R, Palto S P, Ezhov A A and Gorkunov M V 2023 Liquid crystal metasurfaces for versatile electrically tunable diffraction *Liq. Cryst.* **50** 1555–62
[170] Han S Y, Arya A K and Kim S 2022 Liquid crystal based high-efficiency reconfigurable metasurface *2022 International Symposium on Antennas and Propagation* (ISAP 2022) pp 135–6
[171] Ting T-L 2019 Technology of liquid crystal based antenna *Opt. Express* **27** 17138–53
[172] Li W *et al* 2022 Dual-color terahertz spatial light modulator for single-pixel imaging *Light Sci Appl.* **11** 191
[173] Hokmabadi M P, Tareki A, Rivera E, Kung P, Lindquist R G and Kim S M 2017 Investigation of tunable terahertz metamaterial perfect absorber with anisotropic dielectric liquid crystal *AIP Adv.* **7** 015102
[174] Badloe T, Kim J, Kim I, Kim W-S, Kim W S, Kim Y-K and Rho J 2022 Liquid crystal-powered Mie resonators for electrically tunable photorealistic color gradients and dark blacks *Light Sci Appl.* **11** 1–11
[175] Abu Aisheh M, Abutoama M, Abuleil M J and Abdulhalim I 2023 Fast tunable metamaterial liquid crystal achromatic waveplate *Nanophotonics* **12** 1115–27
[176] Rahimi H and Motahari H 2025 High sensitivity metamaterial thin film: bio and thermal sensors based on Fano resonances and nematic liquid crystals *Liq. Cryst.* **52** 59–73
[177] Lio G E, Ferraro A, Zappone B, Parka J, Schab-balcerzak E, Umeton C P, Riboli F, Kowerdziej R and Caputo R 2024 Unlocking optical coupling tunability in epsilon-near-zero metamaterials through liquid crystal nanocavities *Adv. Opt. Mater.* **12** 2302483
[178] Ma Z, Meng X, Liu X, Si G and Liu Y J 2018 Liquid crystal enabled dynamic nanodevices *Nanomaterials* **8** 871
[179] Yoon G, Kim I and Rho J 2016 Challenges in fabrication towards realization of practical metamaterials *Microelectron. Eng.* **163** 7–20
[180] Matei A T, Vişan A I and Popescu-pelin G F 2025 Design and processing of metamaterials *Crystals* **15** 374
[181] Chen Y, Ai B and Wong Z J 2020 Soft optical metamaterials *Nano Converg.* **7** 18

[182] Liao S, Chen Q, Ma H, Huang J, Sui J and Zhang H 2023 A liquid crystal-modulated metastructure sensor for biosensing *Sensors* **23** 7122
[183] Li L, Zhao H, Liu C, Li L and Cui T J 2022 Intelligent metasurfaces: control, communication and computing *eLight* **2** 7
[184] Dong X Y, Su W Q, Ruan Y, Cui H Y and Chen L 2025 Ultra-wideband metasurface absorber based on ITO material *J. Appl. Phys.* **138** 143101
[185] Beddoes B, Klokkou N, Kaczmarek M, Fedotov V A and Apostolopoulos V 2025 Making liquid crystals twitch under metamaterial-enhanced terahertz illumination: toward strong optical nonlinearity *Opt. Express* **33** 1008–19
[186] Chiang W F, Lu Y Y, Chen Y P, Lin X-Y, Lim T-S, Liu J-H, Lee C-R and Huang C-Y 2021 Passively tunable terahertz filters using liquid crystal cells coated with metamaterials *Coatings* **11** 381
[187] Zhou S, Shen Z, Kang R, Ge S and Hu W 2018 Liquid crystal tunable dielectric metamaterial absorber in the terahertz range *Appl. Sci.* **8** 2211
[188] Chikhi N, Lisitskiy M, Papari G, Tkachenko V and Andreone A 2016 A hybrid tunable THz metadevice using a high birefringence liquid crystal *Sci. Rep.* **6** 34536
[189] Zhan H, Guo J, Zhou W, Wang B, Tan H and Ma Q 2025 Multi-objective optimization design of bidirectional metamaterial absorber based on hybrid semi-supervised learning and reinforcement learning *Opt. Mater. Express* **15** 2324–36
[190] Joshi S, Srivastava S, Sharma S, Saxena S, Agarwal S, Tripathi S, Pandey K K and Manohar R 2025 Tunable SWCNT-doped nematic liquid crystals for high-efficiency photonic devices toward quantum and neuromorphic technologies *J. Mol. Liq.* **438** 128695
[191] Zhu R, Wang J, Sui S, Han Y, Chu Z, Jia Y, Li Y, Qiu T, Wang J and Qu S 2023 Chameleon-like intelligent camouflage metasurface *Mater. Des.* **235** 112422
[192] Lin Y-S and Xu Z 2020 Reconfigurable metamaterials for optoelectronic applications *Int. J. Optomechatronics* **14** 78–93
[193] Nandi R, Saeed M U and Chen C-H 2026 Advances in liquid crystal-based sensors driven by nanotechnology: mechanisms, materials, and emerging trends *Sens. Actuators B* **446** 138684
[194] Kanyang R, Fang C, Yang Q, Shao Y, Han G, Liu Y and Hao Y 2022 Electro-optical modulation in high Q metasurface enhanced with liquid crystal integration *Nanomaterials* **12** 3179
[195] Shadrivov I V, Lapine M and Kivshar Y S 2015 *Nonlinear, Tunable and Active Metamaterials* (Springer International Publishing)
[196] Zhu S, Xu Z, Zhang H, Yang K, Wang N, Liu H, Wang Y, Xia J and Huang L 2021 Liquid crystal integrated metadevice for reconfigurable hologram displays and optical encryption *Opt. Express* **29** 9553–64
[197] Kulkarni S and Mishra A 2022 Metamaterials: advancement and futuristic design approach *Wirel. Pers. Commun.* **124** 2075–95
[198] Chung H and Miller O D 2020 Tunable metasurface inverse design for 80% switching efficiencies and 144° angular deflection *ACS Photonics* **7** 2236–43
[199] Lio G E and Ferraro A 2021 LIDAR and beam steering tailored by neuromorphic metasurfaces dipped in a tunable surrounding medium *Photonics* **8** 65
[200] Zhou H, Zhao C, He C, Huang L, Man T and Wan Y 2024 Optical computing metasurfaces: applications and advances *Nanophotonics* **13** 419–41
[201] Guo Z, Xu Y, Hu S, Wang Y, Sun Y and Chen H 2024 Metamaterial-enhanced magnetic resonance imaging: a review *Adv. Photonics Nexus* **3** 054001
[202] Wang K *et al* 2018 Quantum metasurface for multiphoton interference and state reconstruction *Science* **361** 1104–8
[203] Stav T, Faerman A, Maguid E, Oren D, Kleiner V, Hasman E and Segev M 2018 Quantum entanglement of the spin and orbital angular momentum of photons using metamaterials *Science* **361** 1101–4
[204] Li L *et al* 2020 Metalens-array–based high-dimensional and multiphoton quantum source *Science* **368** 1487–90
[205] Santiago-cruz T, Gennaro S D, Mitrofanov O, Addamane S, Reno J, Brener I and Chekhova M V 2022 Resonant metasurfaces for generating complex quantum states *Science* **377** 991–5
[206] Georgi P, Massaro M, Luo K-H, Sain B, Montaut N, Herrmann H, Weiss T, Li G, Silberhorn C and Zentgraf T 2019 Metasurface interferometry toward quantum sensors *Light Sci Appl.* **8** 70
[207] Solntsev A S, Agarwal G S and Kivshar Y S 2021 Metasurfaces for quantum photonics *Nat. Photon.* **15** 327–36
[208] Kort-kamp W J, Azad A K and Dalvit D A 2021 Space-time quantum metasurfaces *Phys. Rev. Lett.* **127** 043603
[209] Kok P, Munro W J, Nemoto K, Ralph T C, Dowling J P and Milburn G J 2007 Linear optical quantum computing with photonic qubits *Rev. Mod. Phys.* **79** 135
[210] Knill E, Laflamme R and Milburn G J 2001 A scheme for efficient quantum computation with linear optics *Nature* **409** 46–52